DEFENCE S&T TECHNICAL BULLETIN

VOL. 15 NUM. 1 YEAR 2022 ISSN 1985-6571

CONTENTS

Ministry of Defence Malaysia

SCIENCE & TECHNOLOGY RESEARCH INSTITUTE FOR DEFENCE (STRIDE)

AIMS AND SCOPE

The Defence S&T Technical Bulletin is the official journal of the Science & Technology Research Institute for Defence (STRIDE). The journal, which is indexed in, among others, Scopus, Index Corpenicus, ProQuest and EBSCO, contains manuscripts on research findings in various fields of defence science & technology. The primary purpose of this journal is to act as a channel for the publication of defence-based research work undertaken by researchers both within and outside the country.

WRITING FOR THE DEFENCE S&T TECHNICAL BULLETIN

Contributions to the journal should be based on original research in areas related to defence science & technology. All contributions should be in English.

PUBLICATION

The editors' decision with regard to publication of any item is final. A manuscript is accepted on the understanding that it is an original piece of work that has not been accepted for publication elsewhere.

PRESENTATION OF MANUSCRIPTS

The format of the manuscript is as follows:

a) Page size A4
b) MS Word format
c) Single space
d) Justified
e) In Times New Roman, 11-point font
f) Should not exceed 20 pages, including references
g) Texts in charts and tables should be in 10-point font.

Please e-mail the manuscript to:

1) Gs. Dr. Dinesh Sathyamoorthy (dinesh.sathyamoorthy@stride.gov.my)
2) Dr. Mahdi bin Che Isa (mahdi.cheisa@stride.gov.my)

The next edition of the journal (Vol. 15, Num. 2) is expected to be published in November 2022. The due date for submissions is 3 August 2022. **It is strongly iterated that authors are solely responsible for taking the necessary steps to ensure that the submitted manuscripts do not contain confidential or sensitive material.**

The template of the manuscript is as follows:

TITLE OF MANUSCRIPT

Name(s) of author(s)

Affiliation(s)

Email:

ABSTRACT

Contents of abstract.

Keywords: *Keyword 1; keyword 2; keyword 3; keyword 4; keyword 5.*

1. TOPIC 1

Paragraph 1.

Paragraph 2.

1.1 Sub Topic 1

Paragraph 1.

Paragraph 2.

2. TOPIC 2

Paragraph 1.

Paragraph 2.

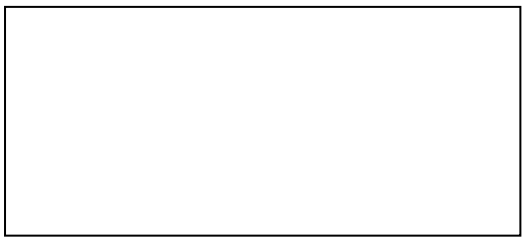

Figure 1: Title of figure.

Table 1: Title of table.

Content	Content	Content
Content	Content	Content
Content	Content	Content
Content	Content	Content

Equation 1 (1)
Equation 2 (2)

REFERENCES

Long lists of notes of bibliographical references are generally not required. The method of citing references in the text is 'name date' style, e.g. 'Hanis (1993) claimed that...', or '…including the lack of interoperability (Bohara *et al.*, 2003)'. End references should be in alphabetical order. The following reference style is to be adhered to:

Books

Serra, J. (1982). *Image Analysis and Mathematical Morphology*. Academic Press, London.

Book Chapters

Goodchild, M.F. & Quattrochi, D.A. (1997). Scale, multiscaling, remote sensing and GIS. *In* Quattrochi, D.A. & Goodchild, M.F. (Eds.), *Scale in Remote Sensing and GIS*. Lewis Publishers, Boca Raton, Florida, pp. 1-11.

Journals / Serials

Jang, B.K. & Chin, R.T. (1990). Analysis of thinning algorithms using mathematical morphology. *IEEE T. Pattern Anal.*, **12**: 541-550.

Online Sources

GTOPO30 (1996). *GTOPO30: Global 30 Arc Second Elevation Data Set*. Available online at: http://edcwww.cr.usgs.gov/landdaac/gtopo30/gtopo30.html (Last access date: 1 June 2009).

Unpublished Materials (e.g. theses, reports and documents)

Wood, J. (1996). *The Geomorphological Characterization of Digital Elevation Models*. PhD Thesis, Department of Geography, University of Leicester, Leicester.

RELATIONSHIP BETWEEN ANGLE OF DEPARTURE AND HEIGHT OF HIT AT STATIC TARGET FOR SMALL ARM WEAPONS

Kamsani Kamal[1*], Razali Abidin[2], Mohamad Asmidzam Ahamat[3], Fakroul Ridzuan Hashim[4] & Muhammad Syafiq Mohd Zamshari[1]

[1]Weapons Technology Division, Science & Technology Research Institute for Defence (STRIDE), Ministry of Defence, Malaysia
[2]Centre for Defence Research and Technology (CODRAT), National Defence University of Malaysia (UPNM), Malaysia
[3]Research & Innovation Section, Universiti Kuala Lumpur Malaysia France Institute (UniKL MFI), Malaysia
[4]Department of Electrical & Electronics Engineering, National Defence University of Malaysia (UPNM), Malaysia

[*]Corresponding author: kamsani.kamal@stride.gov.my

ABSTRACT

Firers normally try to maintain the point of aim on the target when shooting as well as the maximum shifting allowable to ensure that their projectiles are still able to hit target. The shifting of hit position in the vertical direction has relationship with the angle of departure (AoD). The effect of changes to AoD above the limit could cause the target to be missed. Maintaining AoD during firing is difficult especially for small arm weapons. In this study, the prediction of projectile trajectory using six degrees of freedom (6-DOF) is conducted using the PRODAS modelling program to study the allowable limit of change of AoD in the vertical direction during firing that causes change to the height of hit on the target according to specified distance. The static target in the modelling program is assumed as a personnel. The small arm weapon calibres selected based on the target suitability are 5.56, 7.62 and 9 mm. The results obtained show that changing AoD would change the trajectory of the projectile and the position of hit on the target. It would miss the target at the range intended to hit if change of AoD is more than is allowed. Therefore, the firer needs to maintain the AoD when pulling the trigger of the gun in order to hit the target.

Keywords: *Angle of departure (AoD); calibre; trajectory; projectile; aiming.*

1. INTRODUCTION

Maintaining the aiming direction of a weapon is important to ensure that the projectile has consistent hit probability to the target. However, it has a tolerance of allowable angle shift when the projectile leaves the weapon, whereby it is still able to hit the target at distance. The trajectory of the projectile can change due to gun motion (Henelsmith, 2016), which has relationship with the final angle position of the barrel before the projectile exits. Therefore, angle of departure (AoD) has relationship with the trajectory of the projectile to the intended target. This case is more important when firing with small arm weapons that are normally held by hand. Mason (2014) and Taraszewski & Ewertowski (2017) found that that the movement of weapon happens especially at the last phase during pulling the trigger. Maintaining AoD in order to have the same point of hit on the same target is important, especially when firing in fast action. This is usually easier to be done by experienced firers as compared to new firers.

For trajectory, the relationship between muzzle velocity and AoD can give the distance needed for projectile fall. Changing AoD while maintaining muzzle velocity can change the distance of projectile fall. It is also will change the height of projectile trajectory starting from muzzle of the barrel to the

target. Increasing AoD will also increase the height trajectory of the projectile until its maximum angle, which is normally 45°. The trajectory of a projectile is typically considered a straight line for a relatively short distance of up to 30 m for common handguns and rifles (Mattijssen & Kerkhoff, 2016).

Prediction of projectile trajectory using modelling programs is known to be accurate and reliable, and thus is widely used (Courtney & Courtney, 2014). One of the well-known modelling programs is PRODAS, which was used by Litz (2006) in determining the maximum effective range of small arm weapons. In addition, Mukhedkar & Naik (2013) and Rabbath & Corriveau (2019) used this program to predict the maximum height trajectory and direction of drift of projectile according to the AoD entered.

In this study, the prediction of projectile trajectory using six degrees of freedom (6-DOF) is conducted. According to Gkritzapis *et al*. (2007) and Yeh (2020), 6-DOF simulation of flight dynamic model is considered as an accurate prediction of the trajectory of spin stabilised projectiles. Therefore, the trajectory produced shows the allowable limit of change of AoD in the vertical direction during firing that causes change to the height of hit on the target according to specified distance. The effect of barrel movement in the vertical direction over the limit of AoD will cause the target to be missed.

2. METHODOLOGY

2.1 Fundamentals of Forces Acting on the Projectile

Trajectory prediction in this study is conducted using the 6-DOF equation of motion model. It is more accurate in predicting the trajectory of projectiles because it takes into consideration the influence variation of forces, moment, wind, Magnus effects, gravity forces, rotation of earth, spin of projectile, and density of environment (Gkritzapis & Kaimakamis, 2008). It is also sensitive to launch data and shows the information about the stability of projectile during flight (Mukhedkar & Naik, 2013).

The equation of motion starts with Newton's Second Law to estimate the trajectory (Carlucci & Jacobson, 2008; Mukhedkar & Naik, 2013).

$$\mathbf{F} = m\mathbf{a} \tag{1}$$

$$m\frac{d\mathbf{V}}{dt} = \sum \mathbf{F} + m\mathbf{g} + m\boldsymbol{\Lambda} \tag{2}$$

$$\frac{d\mathbf{H}}{dt} = \sum \mathbf{M} \tag{3}$$

where $\frac{d\mathbf{V}}{dt}$ is vector acceleration; $\mathbf{V}$ is vector projectile velocity; $\mathbf{F}$ is vector aerodynamic force consisting of drag force, lift force, Magnus force and pitch damping force; $\mathbf{g}$ is vector acceleration gravity; $\boldsymbol{\Lambda}$ is vector Coriolis acceleration due to earth rotation; $\frac{d\mathbf{H}}{dt}$ is the vector angular momentum of the projectile; $\mathbf{M}$ is vector aerodynamic moments; and m is projectile mass.

6-DOF considers the three rotational components and three translation components on the projectile, as shown in Figures 1 and 2. The translation components describe the coordinate of the centre point of mass of the projectile, while the rotational components describe the orientation of the projectile with respect to translation from the body frame (no-roll frame) to the fixed plane (inertia frame) *X*, *Y*, *Z* (Gkritzapis *et al*., 2007).

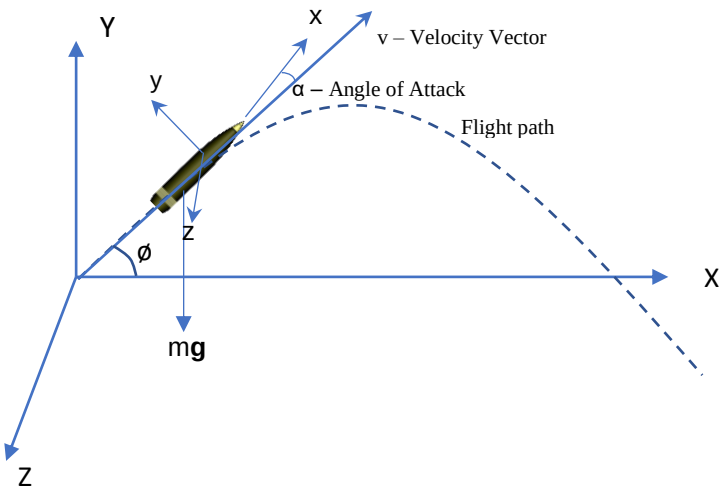

Figure 1: Coordinate system of the projectile trajectory.

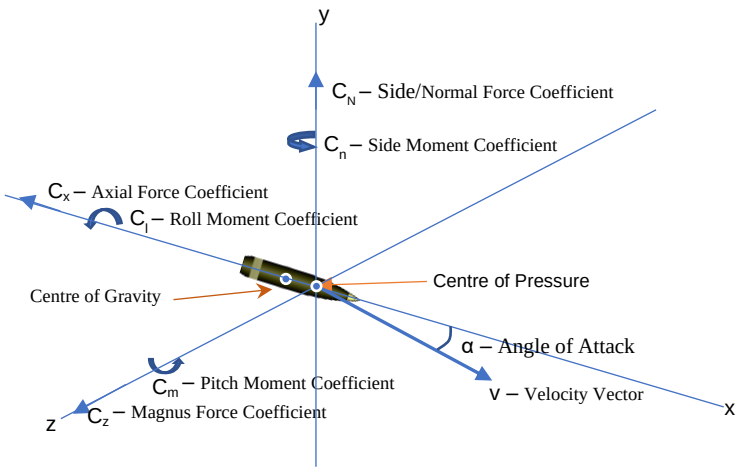

Figure 2: Aerodynamic forces and moments.

2.2 Simulation Procedure of Projectile Trajectory in PRODAS

Small arm weapons with calibres of 5.56, 7.62 and 9 mm were selected in the PRODAS library. The weight, axial and transverse inertias as well as centre of gravity and reference diameter of the projectile models were generated in the mass properties function. The aerodynamic coefficient, gyroscopic and dynamic stability were generated using the aero function. Then, the rotating band diameter, muzzle velocity, twist and gun barrel bore were set to the calibre diameter. The atmosphere code was specified to standard (std) based on the International Civil Aviation Organization (ICAO), with the sea level temperature set at 15 °C, pressure at 1013.25 mbar and density at 1.225 kg/m^3 (PRODAS, 2005). After that, the verified the gyroscopic stability factor in the aero-stability function was more than 1.1.

Lastly, trajectory analysis was run using fixed plane 6-DOF to produce the trajectory prediction with specified AoD. Before that, time of flight and expected distance of projectile were specified. The data generated was then transferred to MS Excel to plot the graphs.

The data produced according to the calibre of projectile is shown in Table 1. AoD with increment of 0.05° is specified accordingly as shown in the table in order to predict the trajectory. The trajectory of projectile is plotted according to distance (range) of the static target in the horizontal direction against the height of hit on the target in the vertical direction. In this study, the 9 mm projectile is plotted for up to 50 m, while the 5.56 and 7.62 mm projectiles are plotted for up to 100 m.

Table 1: Data setup in the analysis.

Projectile	9 mm FMJ 115 gr	5.56 mm M193 Ball FMJ	7.62 mm M80 Ball FMJ
Weight Projectile	7.43 g	3.64 g	9.49 g
Muzzle Velocity	335.0 m/s	990.6 m/s	838.0 m/s
Twist	27.77 cal/rev or 1 turn in 243.9 mm (9.6")	54.82 cal/rev or 1 turn in 304.8 mm (12")	40.01 cal/rev or 1 turn in 304.8 mm (12")
AoD (increment : 0.05°)	0.05 to 2.00°	0.05 to 1.00^0	0.05 to 1.00^0
Exit spin ratio	1		
Trajectory	Fixed Plane 6-DOF		
Met Table Source	std		

2.3 Determination of How the Projectile Hits the Target

In this study, the weapon was positioned horizontally and directed at the static target at the specified distance. The weapon was aimed at the middle of the target, in this case a man standing, as shown in Figure 3. AoD was measured from the horizontal line or 0° angle of the barrel bore line to the target. For the first AoD (Ø1), the projectile was able to hit the target, which was considered as the reference point. Then, AoD was the increased incrementally in the vertical direction until the projectile missed the target. Then, the AoD value and height of hit from the reference point of projectile were recorded. This is aimed at determining the effect of changing AoD vertically when pulling the trigger to the projectile position on the target.

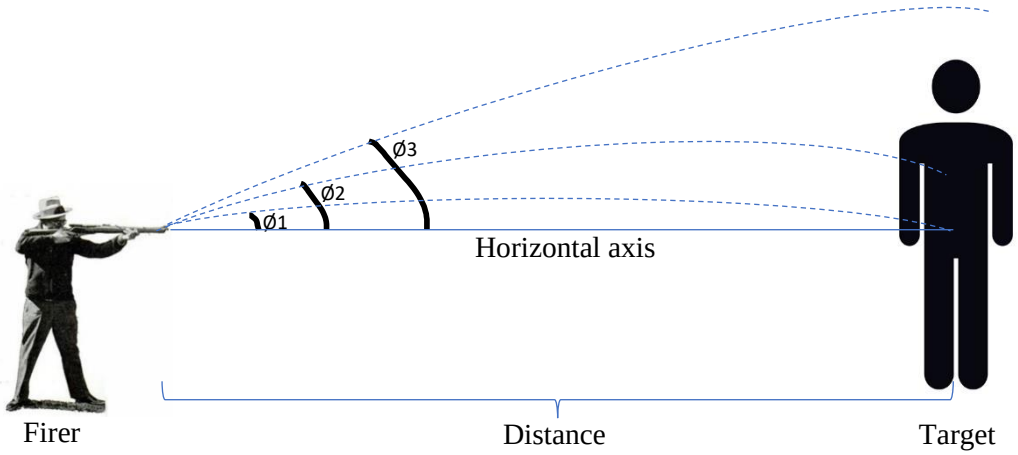

Figure 3: Firing plan.

3. RESULTS

The predicted ranges according to the minimum and maximum AoD considered in this paper are shown in Table 2. It is found that for AoD of 0.05°, small arm weapons with calibres of 5.56, 7.62 and 9 mm had maximum distance of 151.65, 116.42 and 19.62 m respectively. All the calibres had no effect of drift with this AoD along the way to its final distance. The apex height in the trajectory for the 9 mm calibre was 0.00 m; the 5.56 mm calibre had maximum height of 0.04 m at distance 70 m from the muzzle of the gun; and for the 7.62 mm calibre, it was 0.03 m at distance of 50 m.

The 9 mm calibre with AoD of 2.00° had maximum distance of 457.87 m and apex height in the trajectory of 4.97 m at distance of 250 m from the muzzle of the gun. It also had drift effect at this range of about 0.72 m to the right. AoD of 1.00° for the 5.56 mm calibre had maximum distance of 947.09 m, with apex height of 6.75 m at distance of 580 m from the muzzle of the gun and drift to the right with value 0.49 m. For the 7.62 mm calibre, for AoD of 1.00°, it had maximum distance of 1,027.77 m and apex height of 6.56 m at distance of 600 m from the muzzle of the gun with drift to the right of 0.48 m.

The location of these apexes is more than half of the maximum distance produced by every calibre. There was also the effect of drift to the right at maximum distance. All this data indicates that the predicted values had different results because there are differences in projectile weight, muzzle velocity, groove rotation used and environment selected in the program.

Table 2: Summary data collected from simulation.

Calibre Projectile (mm)	AoD (°)	Apex Height from Horizontal Axis (m)	Distance of Apex from Muzzle of Gun (m)	Maximum Drift (m)	Maximum Distance (m)
9	0.05	0.00	-	0	19.62
	2.00	4.97	250	-0.72	457.87
5.56	0.05	0.04	70	0	151.65
	1.00	6.75	580	-0.49	947.09
7.62	0.05	0.03	50	0	116.42
	1.00	6.56	600	-0.48	1027.77

Table 3 shows the predicted change in height of hit in the vertical direction when AoD changed in relation with the specified range distance. When AoD increased, the height of hit `on the target also increased in the vertical direction accordingly. The limit of selected range distance was only for the purpose of this study.

Table 3: The predicted change of high hit on target.

Calibre Projectile (mm)	AoD (°)	Height of Hit on Target from Horizontal Axis (m)	Drift (m)	Range Distance (m)
9	0.15	0.01	-0.01	50
	2.00	1.63	-0.01	50
5.56	0.05	0.03	0	100
	1.00	1.69	0	100
7.62	0.05	0.01	0	100
	1.00	1.67	0	100

The simulation results show that for the predicted trajectory, the 9 mm calibre required AoD of 0.15° in order to be able to hit the target at distance of 50 m, with the height of hit with this angle considered as the reference. When AoD increased by 1.85° from 0.15 to 2.00°, as shown in Figure 4, the predicted height of hit became 1.62 m. The average increasing rate of height of hit is about 0.044 m for every 0.05° increase of AoD.

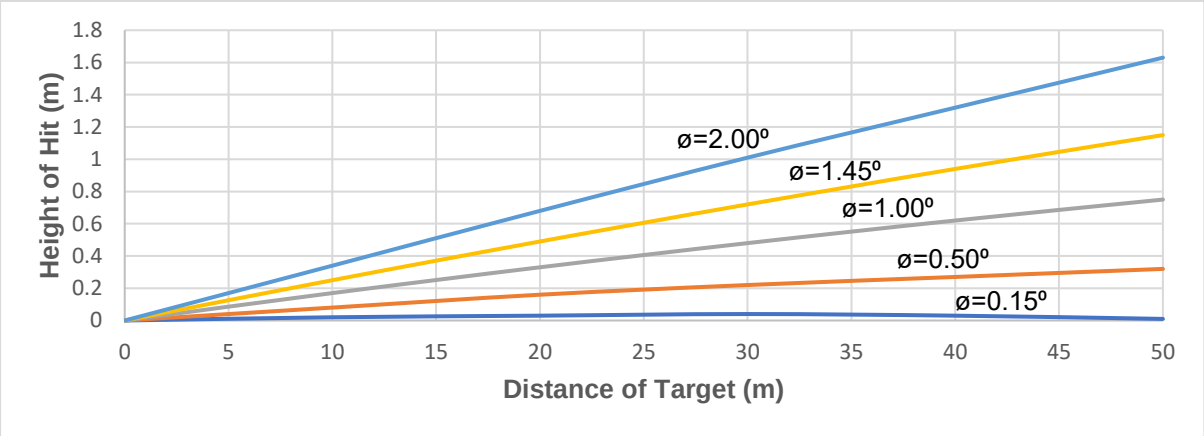

Figure 4: Sample of trajectory change with increasing AoD for the 9 mm calibre with target distance of 50 m.

The 5.56 mm calibre with AoD of 0.05° was able to hit the target at distance of 100 m, which was considered as the starting point of height of hit on the target. The predicted height of hit became 1.66 m from starting point hit when AoD increased by 0.95° from 0.05 to 1.00°, as shown in Figure 5. The average increase of rate of height of hit was about 0.088 m for every 0.05° increase of AoD. This result is almost the same for the 7.62 mm calibre in order to be able to hit the target at distance of 100 m. The reference AoD started at 0.05° and the hit position with this angle was considered as the reference. The predicted height of hit became 1.66 m when the AoD increased by 0.95° from 0.05 to 1.00°, as shown in Figure 6, with the average rate of height increase being 0.087 m for every 0.05° in increase of AoD.

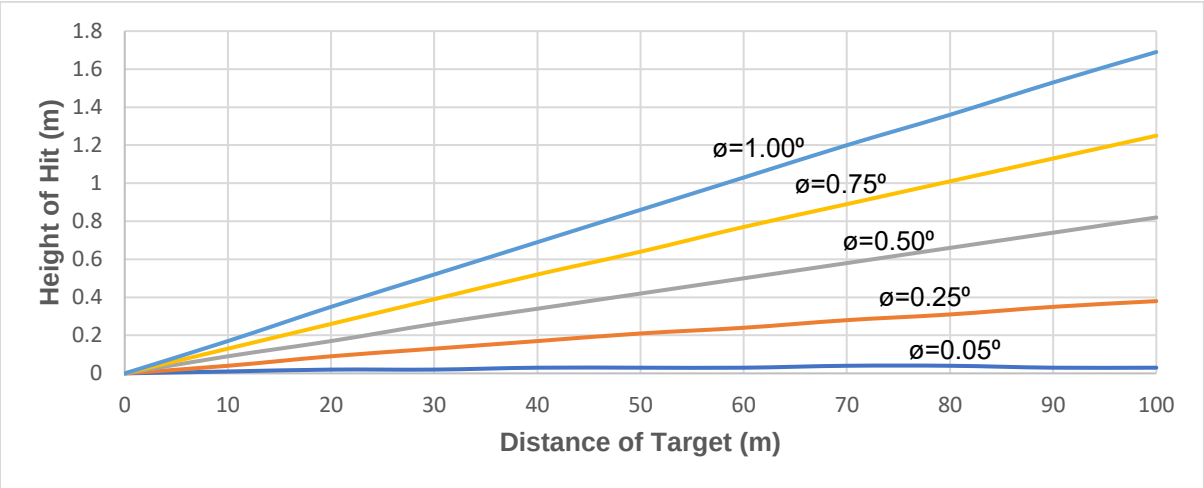

Figure 5: Sample of trajectory change with increasing AoD for the 5.56 mm calibre with target distance of 100 m.

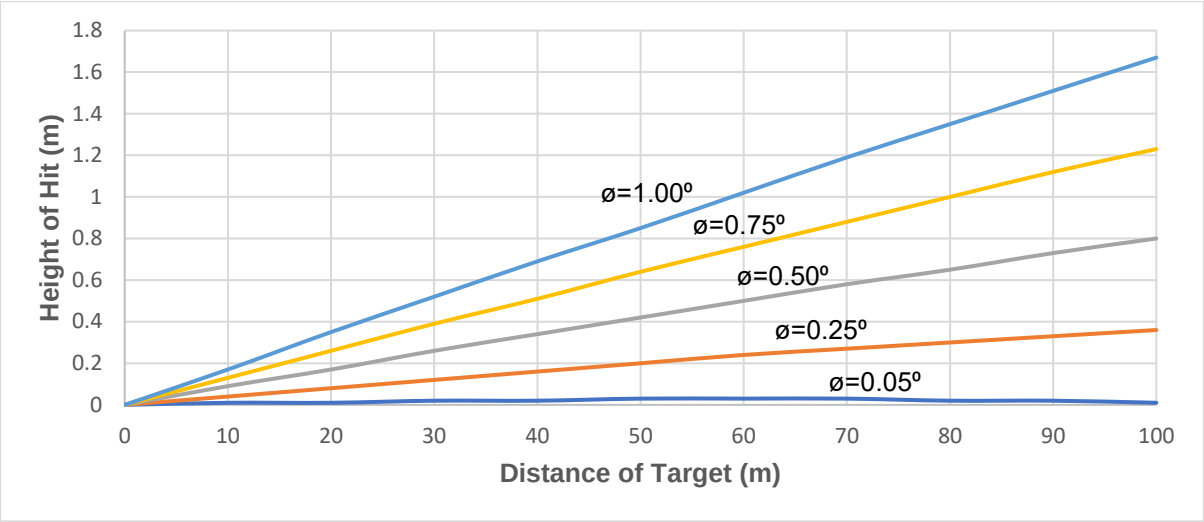

Figure 6: Sample of trajectory change with increasing AoD for the 7.62 mm calibre with target distance of 100 m.

Referring to the graphs for every calibre, the predicted projectile trajectory path is almost in a straight line up to the specified distance of the target. Therefore, the changes of height of hit on target are directly proportional with the change of AoD.

4. DISCUSSION

The results obtained in this study demonstrated that change of AoD of the gun in firing upwards will change the flight trajectory and distance of fall of the projectile. The graphs of trajectory change also showed that the height of projectile trajectory for every AoD changed accordingly. Due to this, it has relationship with the hit position on the target at the specified distance. A small change of AoD in the vertical direction of firing will give an impact on the position of hit on the target. Therefore, in firing, the allowed change of AoD is small, especially when the distance from the gun to the target is large. This is true for every calibre studied. The projectiles also had drift effect to the right. However, this drift was considered small and did not count in this study. The results of hit position on the target in terms of external ballistics also depend on the projectile calibre, muzzle velocity, length of barrel, twist, flight stability, projectile weight, firer stability, AoD and environment (Carlucci & Jacobson, 2013). From experience, normally the firer aims his or her gun from the belly or abdomen to the head of the soldier.

The target of small arm guns used by militaries for 5.56, 7.62 and 9 mm calibres is typically humans. Previous studies showed that the average height of humans in the Asia-Pacific region for men is 1.69 m and 1.57 m for women (Lee *et al*., 2009). For the American continent, the mean height is 1.76 m (Fessler *et al*., 2012), and 1.84 m for Europe (Grasgruber *et al*., 2016). Therefore, changes of height are only allowable for these heights.

For example, if a firer aimed the gun at the middle of an average Europe man of his height. The firer has available height of only 0.92 m. As shown in Table 4, for a 9 mm projectile with weight of 7.43 g and muzzle velocity of 335 m/s with target position at 50 m, the allowed AoD to move in the vertical direction is not more than 1.05°. It will miss that target if AoD is more than this angle. For a 5.56 mm

projectile with weight of 3.64 g and muzzle velocity of 990.6 m/s, the allowed AoD during firing is not more than 0.50°. This will produce height of hit of 0.91 m when the target is at distance of 100 m. For a 7.62 mm projectile with weight of 9.49 g and muzzle velocity of 838.0 m/s, the allowed AoD is up to 0.45° when the target is at distance of 100 m, which will produce height of hit of 0.79 m. These AoD values are for half man height from the belly or abdomen of soldier to the head. The AoD values would be smaller for human targets from the Asia-Pacific region and American continent.

This study shows that the allowable AoD increase for the 9 mm calibre is 1.05°, 0.50° for 5.56 mm and 0.45° for 7.62 mm. The firer will miss the target if his or her gun changes its AoD during the proses of pulling the trigger. If the target moves nearer to the gun, the firer has higher probability to hit the target, but if the target moves further away, it will miss the target. The 5.56 and 7.62 mm calibres have almost the same predicted trajectories even though they have different weights. This is because they have the same profile of projectile shape and drag effect. Therefore, they have almost the same characteristics. However, the 9 mm calibre has different predicted trajectory due to the obvious difference in weight of projectile and less muzzle velocity. For all the three calibres studied, it is found that that the projectile will hit the target if the firer is able to maintain its AoD within the range as shown in Table 4.

Table 4: Allowable angle of departure for the projectile able to hit the human target.

Projectile (mm)	Total Allowable Angle Increased (°)	Estimated Height of Hit Produced (m)	Target Distance (m)
9	1.05	0.92	50
5.56	0.50	0.91	100
7.62	0.45	0.79	100

5. CONCLUSION

The study shows that changing AoD would change the trajectory of the projectile and the position of hit on the target. It would miss the target at the range intended to hit if change of AoD is more than is allowed. Therefore, the firer needs to maintain the AoD when pulling the trigger of the gun in order to hit the target. The capability of projectile in hitting the target will be more difficult when it is moving further away from the gun position, and it will be easier when the target is moving closer. The factors that affect the capability to hit the target include the stability of holding the gun during the action of pulling the trigger, the quality of gun produced, weight of projectile, muzzle velocity, stability of flight projectile and environment. Further studies are needed to understand the limit of change of AoD on every small arm gun and projectile in order to help the firer to be able to hit its target.

ACKNOWLEDGEMENT

The authors are grateful to the Science & Technology Research Institute for Defence (STRIDE), National Defence University of Malaysia (UPNM) and Universiti Kuala Lumpur Malaysia France Institute (UniKL MFI) for allowing the use their facilities, as well as support and assistance in preparing this paper.

REFERENCES

Carlucci, D. E. & Jacobson, S. S. (2013). *Ballistics: Theory and Design of Guns and Ammunition*. CRC Press, Florida, US.

Courtney, E.R. & Courtney, M.W. (2014.). *Aerodynamic Drag and Gyroscopic Stability*. Cornell University Library, Ithaca, New York, US.

Fessler, D.M.T., Holbrook, C. & Snyder, J.K. (2012). Weapons make the man (larger): Formidability is represented as size and strength in humans. *PLoS ONE*, **7**:e32751

Gkritzapis, D.N. & Kaimakamis, G. (2008). A review of flight dynamic simulation model of missiles. *2nd Eur. Comput. Conf. (ECC '08)*, 11-13 September 2008, Malta, pp. 257-261.

Gkritzapis, D.N., Panagiotopoulos, E.E., Margaris, D.P. & Papanikas, D.G. (2007). A six degree of freedom trajectory analysis of spin-stabilized projectiles. *AIP Conf. Proc.*, **963**: 1187–1194.

Grasgruber, P., Sebera, M., Hrazdíra, E., Cacek, J. & Kalina, T. (2016). Major correlates of male height: A study of 105 countries. *Econ. Human Biol.*, **21**: 172–195.

Henelsmith, N. (2016). *Projectile Motion: Finding the Optimal Launch Angle*. Whitman College, Walla Walla, Washington, US.

Lee, C. M.Y., Barzi, F., Woodward, M., Batty, G.D., Giles, G.G., Wong, J.W. & Yao, S.X. (2009). Adult height and the risks of cardiovascular disease and major causes of death in the Asia-Pacific region: 21 000 deaths in 510 000 men and women. *Int. J. Epidemiol.*, **38**: 1060–1071.

Litz, B.B. (2006). *Maximum Effective Range of Small Arms*. Applied Ballistics, Howard City, Michigan, US.

Mason, B.R. (2014). Factors affecting accuracy in pistol shooting. *Excel*, **6**: 2-6.

Mattijssen, E.J. & Kerkhoff, W. (2016). Projectile trajectory reconstruction - Methods, accuracy and precision. *Forensic Sci. Int.*, **262**: 204–211.

Miller, M.W.O. (2018). *Armoured Military Vehicles Catalogue*. SAE Technical Papers, Warrendale, Pennsylvania, US

Mukhedkar, R.J. & Naik, S.D. (2013). Effects of different meteorological standards on projectile path. *Defence Sci. J.*, **63**: 101–107.

Rabbath, C.A. & Corriveau, D. (2019). A comparison of piecewise cubic Hermite interpolating polynomials, cubic splines and piecewise linear functions for the approximation of projectile aerodynamics. *Defence Tech.*, **15**: 741-757.

PRODAS (2005). *PRODAS V3 Technical Manual*. Arrow Tech, South Burlington, Vermont, US

Taraszewski, M. & Ewertowski, J. (2017). Complex experimental analysis of rifle-shooter interaction. *Defence Tech.*, **13**: 346–352.

Yeh, D.P. (2020). *Six Degrees of Freedom (6DOF) Simulations of Supersonic Fragment Trajectories*. Sandia Laboratories, Deparment of Energy, Washington, DC, US.

INDUSTRIAL SPECT SIMULATION FOR IMAGING RADIOTRACER DISTRIBUTION IN A PIPELINE USING MCNPX CODE

Hanafi Ithnin[1,2,*], Elmy Johanna Mohamad[1], Norliana Mohd Lip[3], Ismail Mustapha[2] & Nazrul Hizam Yusoff[2]

[1]Faculty of Electrical Engineering, Universiti Tun Hussein Onn, Malaysia
[2]Industrial Technology Division, Malaysian Nuclear Agency, Malaysia
[3]Faculty of Computer and Mathematical Science, Universiti Teknologi MARA, Malaysia

[*]Email:hanafi_i@nm.gov.my

ABSTRACT

The development of a single photon emission computed tomography (SPECT) system for industrial applications has become increasingly desirable, as it enables the industry to image and monitor flow processes in a closed conduit system non-invasively. Different industrial SPECT (iSPECT) system configurations were modelled in this study using a maximum of 36 sodium iodide (NaI) scintillation detectors. These configurations were then used to simulate the iSPECT imaging process in a 20 cm diameter pipeline for cross-sections with varying laminar flow levels. The flow rate was varied from 20 to 80% of the pipeline volume per diameter along with the configurations of the detectors. The results demonstrated that using the modelled iSPECT system, different laminar flow levels can be imaged correctly. The nonagonal iSPECT configuration provided the most accurate image of the flow level of up to 60% of the pipeline volume per diameter.

Keywords: *Emission tomography; industrial SPECT (iSPECT); distribution-source imaging; Monte Carlo N-Particle eXtended (MCNPX) simulation; Gamma-ray tomography*.

1. INTRODUCTION

Transmission computed tomography, also known as structural imaging, has been widely used in medical and industrial applications to visualise an object's internal structure. On the other hand, emission tomography, particularly the single photon emission tomography (SPECT) system, has been extensively used in medical applications as a diagnostic tool (Van den Wyngaert *et al.*, 2020; Auer *et al.*, 2021). The SPECT system has been used in industries on a limited basis due to the system's need to be optimised for each industrial problem. Medical SPECT imaging is limited to diagnosing specific human organs that have been performed repeatedly thus, medical SPECT systems are optimised for human imaging (Israel *et al.*, 2019). In contrast, in an industrial setting, various objects of interest must be scanned, necessitating the system to complement the industrial problem's nature. The primary distinction between medical and industrial SPECT systems is the requirement of the radiotracers type, spatial image resolution and temporal resolution. Nevertheless, the fundamental principle in radiation measurement and image reconstruction procedure remains the same for both systems (Kim, 2014).

Several works have been conducted for applying industrial SPECT (iSPECT) for different industrial problems. Legoupil *et al.* (1997) developed an experimental SPECT system for dynamic fluid flow analysis. They used 36 NaI detectors arranged in a hexagonal structure. The results were promising, whereby two-dimensional images of the radiotracer distribution were successfully constructed. An advanced work was done by Park *et al.* (2014a), where they conducted a performance evaluation of an industrial SPECT system with a 12-gonal diverging collimator for flow visualisation in industrial reactors. The resultant image of the radiotracer distribution showed that the system could differentiate varying sources in static and dynamic conditions of the reactor. In a more recent work, Mesquita. (2020) developed a hybrid industrial tomographic system by simultaneously combining the emission tomography system with a transmission system using five gamma-ray sources. The resultant images showed the possibility of the two systems being used simultaneously for industrial applications as they are currently being used in the medical system. There are

also other works, including experimental and simulation works in developing SPECT systems for different industrial applications (Park *et al.*, 2013, 2014b; Ithnin *et al.*, 2020). All of these previous works mainly focused on either the distribution of the radiotracer or the position of the radiation source.

The purpose of this study is to simulate the ability of three distinct iSPECT configurations to image laminar flow level in a horizontal pipe. Hexagonal, octagonal and nonagonal structures are used for the iSPECT system. For these three configurations, the simulated iSPECT system will employ a maximum of 36 sodium iodide (NaI) scintillation detectors. Monte Carlo N-Particle eXtended (MCNPX) is used to model and simulate radiation detection for the iSPECT system. The MCNPX code is a general-purpose Monte Carlo radiation transport code designed to track many particle types over broad ranges of energies (Pelowitz, 2008). The volume source is created to represent the various levels of a distributed source within the horizontal pipeline. Finally, the maximum likelihood expectation maximisation (ML-EM) algorithm is used to reconstruct the cross-section image of the distribution source (Bruyant, 2002; Wernick & Aarsvold, 2004).

2. METHODOLOGY

2.1 iSPECT system

The iSPECT system was modelled in this study in order to develop a system that can be applied in industrial environments under two constraints; the number of measurement tools available and the size of the imaging region of interest (ROI). The maximum number of detectors used in this study was 36 NaI scintillation detectors. The detectors were collimated using lead (Pb) with hole width of 0.5 cm and depth of 3.5 cm, as illustrated in Figure 1.

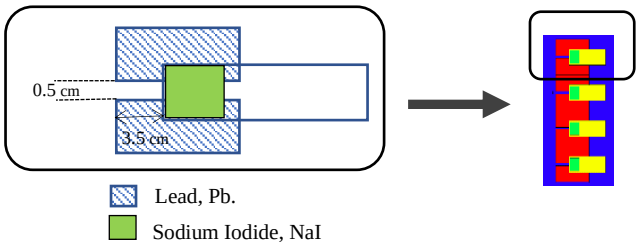

Figure 1: Single NaI scintillation model and four detectors arranged in an array for iSPECT simulation.

The scanning area or ROI in this study was a circular pipeline with diameter of 20 cm that was centrally located within the iSPECT system. As suggested in IAEA-TECDOC 1589, the ROI was chosen based on the acceptable condition calculated using Equation 1 (IAEA, 2008). The diameter ranges for the scanning region in relation to the collimator geometry and number of detectors used in the simulation of the iSPECT system are listed in Table 1.

$$1 \leq \frac{FWHM \; x \; No \; of \; detectors}{Diameter \; ROI} \leq 2 \tag{1}$$

where:

$$FWHM = \frac{Collimator \; hole \; width \; x \; Distance \; detector \; to \; column \; centre}{Collimator \; hole \; depth} \tag{2}$$

Table 1: Conditions for acceptable ROI ranges.

iSPECT Configuration	ROI range (cm)
Hexagonal	20 - 41
Octagonal	11 - 23
Nonagonal	12 - 25

In accordance with the study's limitation condition, three iSPECT system configurations were chosen for the current study. As illustrated in Figure 2, the hexagonal arrangement consists of six arrays of six detectors (6x6); the octagonal arrangement consists of eight arrays of four detectors (8x4); and the nonagonal arrangement consists of nine arrays of four detectors (9x4). The sketch diagram in Figure 3 illustrates the iSPECT system mounted around a pipeline for imaging the flow level inside the pipeline.

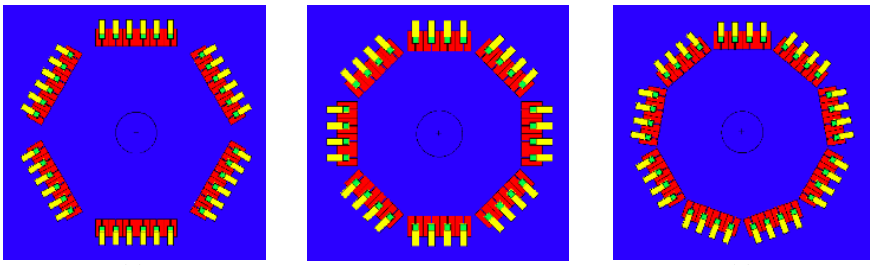

Figure 2: The three different iSPECT system configurations used in this study; (a) Hexagonal (6x6). (b) Octagonal (8x4). (c) Nonagonal (9x4).

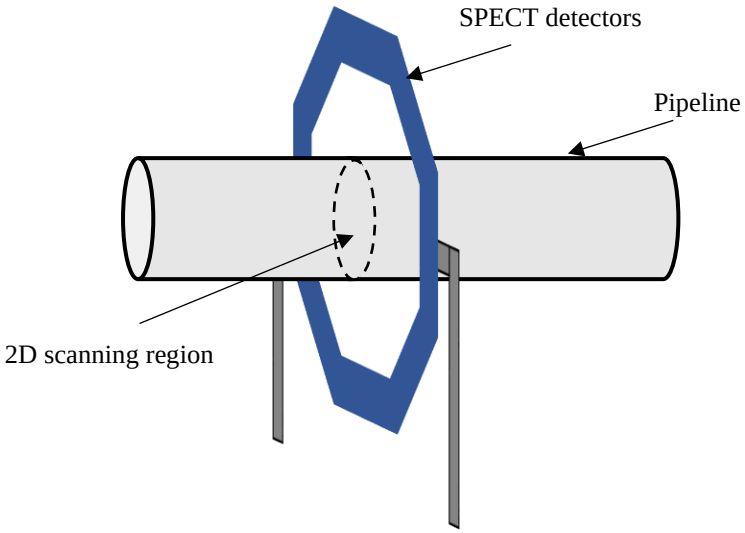

Figure 3: Illustration of the iSPECT system for pipeline imaging.

2.2 Imaging Distribution Source

All image reconstruction processes were carried out using LabVIEW's ML-EM function. The ML-EM algorithm and its variations have been among the leading image reconstruction algorithms utilised for emission computed tomography (CT) systems. For the emission tomography reconstruction problem, the ML-EM framework yields the following equation:

.

$$\hat{f}_j^{(n+1)} = \frac{\hat{f}_j^{(n)}}{\sum_{i'} h_{i'j}} \sum_i h_{ij} \frac{g_i}{\sum_k h_{ik} \hat{f}_k^{(n)}} \tag{3}$$

where g_i is detector count, $f^{(n)}$ is estimated image value, and h_{ij} is system matrix or probability of detecting photon on the i detector from the emission of tracer at position j. The system matrix h_{ij} is calculated using a 41 x 41-pixel grid. Thus for 20 cm ROI, the number of point sources calculated is 1,245 points for the three iSPECT configurations as illustrated is Figure 4.

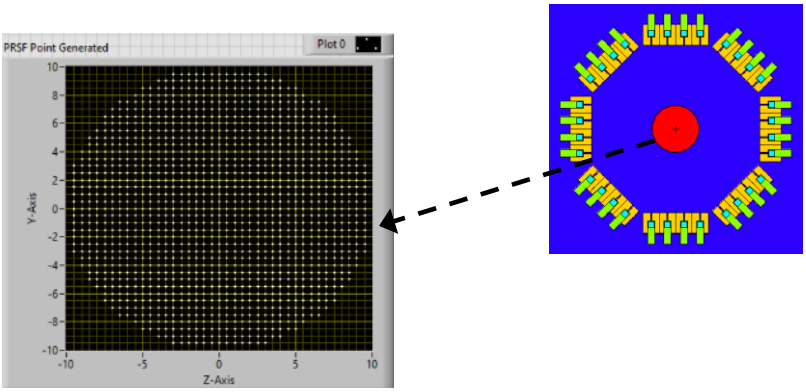

Figure 4: 1,245 points in the system matrix for 20 cm ROI.

Laminar flow level imaging was conducted by simulating the distribution source inside the ROI. Four different distribution sources were simulated in this study, simulating the various levels of laminar flow inside a horizontal pipeline. In this study, caesium (Cs-137) was used as a gamma-ray source with energy of 622 keV that is distributed evenly throughout the pipeline. Figure 5 illustrates the four different distribution source levels at 20, 40, 60 and 80% of the diameter of the ROI.

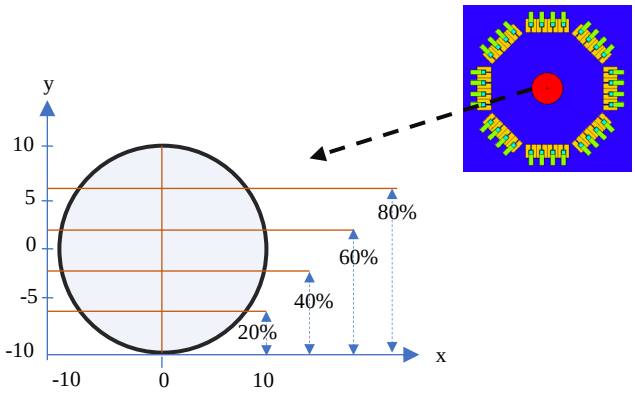

Figure 5: Different levels of distribution source simulating the iSPECT imaging of different water levels in a pipeline.

3. RESULT AND DISCUSSION

Figure 6 shows the reconstructed images from the three iSPECT systems simulated using different distribution sources. The first row represents the reconstructed images from the hexagonal configuration, the second row is from the octagonal configuration, and the last row is from the nonagonal configuration. In the figure, the first column is the reconstructed images for source distribution at 20% of ROI diameter, the second column is 40%, the third column is 60%, and the last column is 80%. The green circle is the reference for ROI circumference, which has a diameter of 20 cm, and the dashed red line is the reference line where the actual level of distribution source is expected in the image. In emission tomography, the reconstructed image is actually the mapping of the gamma-ray source intensity distribution. Thus, the bright blue pixels in the reconstructed images represent a higher probability of the iSPECT system to detect the gamma-ray source, while the darker pixels inside the ROI represents the lack of gamma-ray source detected.

The reconstructed images in Figure 6 show that all three configurations were able to image the distribution source up to 60% of the ROI diameter. However, for all three configurations, for distribution source at 80% of the ROI diameter, Figure 6 (iv) shows that the image reconstructed cannot accurately estimate the distribution source level. On the other hand, at a lower distribution source percentages of the ROI diameter, the images were estimated accurately. The overestimation is due to the fact that the same amount of source activity is diluted when the volume fraction is higher and more concentrated in a lower volume percentage.

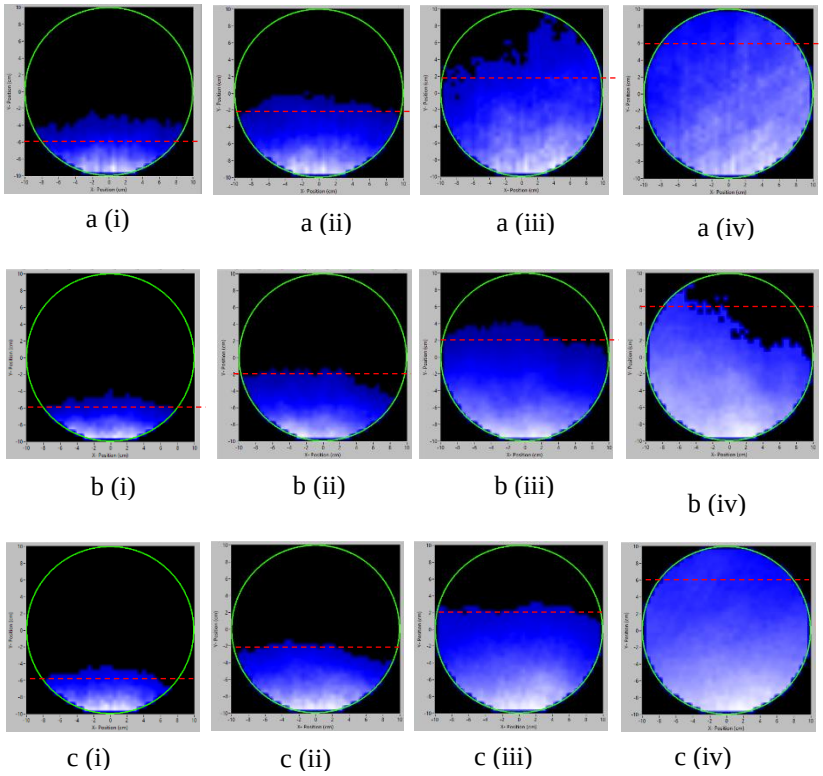

Figure 6: Reconstructed images of the distribution source for the (a) hexagonal, (b) octagonal and (c) nonagonal iSPECT configurations at (i) 20%, (ii) 40%, (iii) 60% and (iv) 80% of ROI diameter.

The intensity profile plot in Figure 7 is obtained from the *y*-axis view of the reconstructed images in Figure 6. Figure 7(i) is the profile plot for 20%, 7(ii) is the profile plot for 40%, and 7(iii) is the profile plot for 60%. The red dashed line represents the actual level of the source distribution per diameter, and on the intensity axis, 1 is the brightest pixel colour and 0 represents the dark / black pixel colour. From the graphs presented in Figure 7, the hexagonal configuration overestimated the level of distribution source as compared to the octagonal and nonagonal configurations, whereby the resulting reconstructed images showed nearly similar results. The difference is that the octagonal system had slightly overestimated the level of distribution source as compared to the nonagonal system. From the simulation results, the nonagonal configuration of the iSPECT system is the best structure for imaging the different levels of distribution source inside a horizontal pipeline. The plotted lines intersect with the actual distribution source levels at pixel intensities of 0.75, 0.33, and 0.50 for percentages of ROI diameter of 20, 40 and 60% respectively, resulting in an average of 0.53. Additionally, the graphs also show that the best position to estimate the level of the reconstructed image for source distribution for up to 60% of the ROI diameter is at half of the intensity.

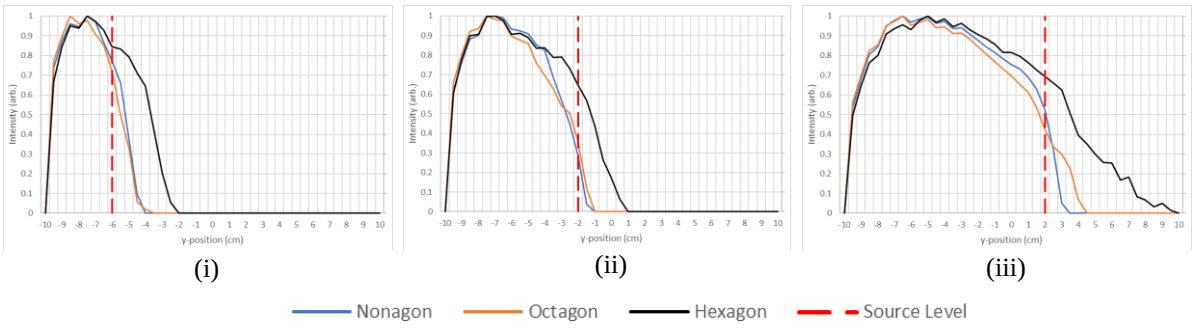

Figure 7: Intensity profile plots of the reconstructed images for (a) 20%, (b) 40% and (c) 60% of distribution source level for the three iSPECT configurations.

4. CONCLUSION

The hexagonal, octagonal, and nonagonal iSPECT system configurations were simulated in this study to image the different percentage levels of the distribution source inside a horizontal pipeline. The iSPECT system was simulated using a maximum of 36 NaI detectors, and the system was applied for imaging of a 20 cm scanning ROI inside a pipeline. The reconstructed images showed that all three configurations can estimate the different source distribution levels for up to 60% of ROI diameter. From the results obtained, it was determined that half of the intensity value is the best position to estimate the level of the reconstructed images for source distribution. Of the three configurations of the iSPECT system, the nonagonal configuration was found to be the best structure for imaging the different levels of distribution source inside a horizontal pipeline.

REFERENCES

Auer, B., Zeraatkar, N., Goding, J.C., Könik, A., Fromme, T.J., Kalluri, K.S. & King, M.A. (2021). Inclusion of quasi-vertex views in a brain-dedicated multi-pinhole SPECT system for improved imaging performance. *Phys. Med. Biol.*, **66**: 035007.

Bruyant, P.P. (2002). Analytic and iterative reconstruction algorithms in SPECT. *J. Nucl. Med.,* **43**: 1343-1358.

IAEA (2008). *TECDOC 1589, Industrial Process Gamma Tomography*. International Atomic Energy Agency, Austria.

Ithnin, H., Mohamad, E.J., Yusoff, N.H., Hassan, H. & Lip, N. M. (2020, April). Development of industrial single photon emission computed tomography (ISPECT). *IOP Conf. Ser-Mat. Sci.,* Vol. **785**: p. 012024).

Israel, O., Pellet, O., Biassoni, L., De Palma, D., Estrada-Lobato, E., Gnanasegaran, G. & Giammarile, F. (2019). Two decades of SPECT/CT–the coming of age of a technology: an updated review of literature evidence. *Eur. J. Nucl. Med. Mol. I.*, **46**: 1990-2012.

Kim, J.B., 2014. Principle and Application of SPECT. *IAEA/RCA Regional Training Course on Industrial Radioactive Particle Tracking and SPECT for Multi-Phase Process Investigation*, 14-18 April 2014 Kajang, Malaysia.

Legoupil, S., Pascal, G., Chambellan, D. & Bloyet, D. (1997). An experimental single photon emission computed tomograph method for dynamic 2D fluid flow analysis. *Appl. Radiat. Isot.*, **48**: 1507-1514.

Mesquita, C.H., Velo, A.F., Calvo, W.P., Carvalho, D.V. & Hamada, M.M. (2020). Emission and transmission tomography system applied to analyse industrial process inside chemical reactors. *Nucl. Instrum. Methods A*, **954**: 161847.

Park, J.G., Kim, C.H., Han, M.C., Jung, S.H., Kim, J.B. & Moon, J. (2013). Optimisation of detection geometry for industrial SPECT by Monte Carlo simulations. *J. Instrum.*, **8**: C04006.

Park, J.G., Jung, S.H., Kim, J.B., Moon, J., Yeom, Y.S. & Kim, C.H. (2014a). Performance evaluation of advanced industrial SPECT system with diverging collimator. *Appl. Radiat. Isot.*, **94:** 125-130.

Park, J.G., Jung, S.H., Kim, J.B., Moon, J., Han, M.C. & Kim, C. H. (2014b). Development of advanced industrial SPECT system with 12-gonal diverging-collimator. *Appl. Radiat. Isotopes*, **89**, 159-166.

Pelowitz, D. B. (2008). *MCNPX User Manual Version 2.6*. Los Alamos National Lab. (LANL), Los Alamos, New Mexico, United States.

Van den Wyngaert, T., Elvas, F., De Schepper, S., Kennedy, J.A. & Israel, O. (2020). SPECT/CT: Standing on the shoulders of giants, it is time to reach for the sky. *J. Nucl. Med.*, **61**: 1284-1291.

Wernick, M.N. & Aarsvold, J.N. (2004). *Emission Tomography: The Fundamentals of PET and SPECT*. Amsterdam, Netherlands.

FINITE ELEMENT ANALYSIS FOR TRANSIENT THERMAL CHARACTERISTICS OF DIE-ATTACH ADHESIVE GRAPHENE CONDUCTIVE PASTE

Ameeruz Kamal Ab Wahid[1,2], Mohd Azli Salim[2,3,4*], Nor Azmmi Masripan[2,3,4] & Adzni Md. Saad[3,4]

[1]Jabatan Kejuruteraan Mekanikal, Politeknik Sultan Azlan Shah (PSAS), Malaysia
[2]Advanced Manufacturing Centre, Universiti Teknikal Malaysia Melaka (UTeM), Malaysia
[3]Fakulti Kejuruteraan Mekanikal, Universiti Teknikal Malaysia Melaka (UTeM), Malaysia
[4]Intelligent Engineering Technology Services Sdn. Bhd., Malaysia

[*]Email: azli@utem.edu.my

ABSTRACT

With the increase of operating temperature of high-temperature power electronics applications, a new requirement has emerged, which requires appropriate materials that meet the new specifications. In this context, the die-attach layer (attached substance between the semiconductor device and substrate) is one of the most significant components of power electronics modules, and choosing the right die-attach material is one of the most difficult challenges. Using transient thermal analysis, this study determines the best die-attach materials for conductive ink performance in thermal conductivity. It was carried out with the use of finite element analysis (FEA) modelling approaches. For FEA analysis, four different die-attach materials of conductive ink straight line patterns were developed: Au/Sn (80/20) braze, nanoscale silver, SAC alloy solder paste, and Epo-Tek P1011 epoxy. By evaluating the maximum temperature and total heat flux, FEA modelling can be utilised to identify which die-attach materials have more effect on thermal conductivity to the graphene conductive ink circuits on copper substrate. For the varying die-attach materials' effect of thermal conductivity, a modelling approach of conductive ink patterns with silicon carbide (SiC) diodes attached to the directly bonded graphene with die-attach materials was proposed to be used. The temperature and total heat flux time-dependent during heating within 1.5 s was optimised by using temperature load of 90.3 °C on the dies (diode) in the circuit. The epoxy achieved the best results in terms of the least maximum temperature and total heat flux with the values of 90.3 °C and 0.8073 x 10^7 W/m^2 respectively. As a result, epoxy types of die-attach materials have the best potential to be effective heat conductors. This is due to the results that epoxy die-attach materials have the highest thermal resistance and lowest thermal conductivity.

Keywords: *Die-attach materials; graphene conductive inks; finite element analysis (FEA); transient thermal; thermal conductivity.*

1. INTRODUCTION

The integrated circuit, which is an assembly of millions of interconnected components such as resistors and transistors built on a tiny silicon chip, is the foundation of modern electronics. These circuits rely on insulating materials to maintain their reliability, which can serve as substrates for microscopic electronic components, and their connections are built and packaged within the structure itself, sealed in a circuitry away from the environment, resulting in a single, compact unit (Wahid *et al.*, 2021). With many different sorts of circuit sizes, conductive ink circuit reliability is becoming a growing challenge. With decreasing interconnect size and rising number of interconnect layers, the impact of interconnect failure materials on conductive filler failure rate increases significantly. The influence of boundary scattering on cross-plane thermal conductivity decreases as the layer number increases (Wei *et al.*, 2011).

The application of die-attach layers is one of the most important aspects of the manufacturing process in the design of power electronics packaging technologies. This connection must meet certain requirements to ensure proper operation and wear resistance, such as sufficient adhesion between die and substrate, which ensures that the die is firmly attached to the substrate, high electrical and thermal conductivities, suitable mechanical properties to avoid and support thermo-mechanical stresses, and a high melting point to ensure reliability (Melchor, 2015). Epoxy and eutectic solder compounds are commonly used as die-attach materials (Chidambaram *et al.*, 2017). Navarro *et al.* (2019) used SiC dies and silver (Ag) sintered die-attach layer produced in two different ways onto copper (Cu) substrates to investigate the deterioration of the die-shear force during thermal cycling, as well as the impact of thermal cycling on the electrical behaviour of the die-attach layer. The researcher's observation results found that the maximum cycling temperature rose to 275 °C within 20 min and close to the sintering temperature of 285 °C. The maximum cycling temperature value was selected according to the homologous temperature (the margin between the operating temperature and melting point) of the die-attach materials used in their work.

New die-attach materials with higher melting points and good thermo-mechanical characteristics are required by new application areas requiring higher operating device temperatures in power systems. Specific die-attach materials are thus a genuine issue to meet the criteria of high-temperature power electronics applications (Navarro *et al.*, 2019). As a result, several studies have been conducted to determine the best materials and processes for producing high-temperature die-attach. These high-temperature application die-attach materials have severe requirements and tests. Gold-tin (Au-Sn), gold-germanium (Au-Ge), gold-silicon (Au-Si), silver glass, silver-indium (AgIn), high lead (Pb) solutions, and nanoscale silver are only a few of the high-temperature application die-attach materials that have been investigated so far. Due to technological advancements, these high-temperature die-attach materials have been used in a variety of industries (Tan *et al.*, 2017). The thickness of the die-attach layer has little effect on the thermal conductivity of die-attach materials. The die-attach materials layer thickness (a few micrometres) has little effect on the model heat flux conduction, allowing heat to flow more easily (He *et al*., 2017; Jiang *et al.*, 2018)

Die-attach is a material that is used to connect the conductive inks to the circuit's components. To make the circuit system efficient and can satisfy other requirements, it must include materials with good mechanical, electrical, and thermal properties. Among the conditions that must be satisfied are the adhesion of the circuit whereby the connection will not result in components and circuits being isolated, capable of functioning at high temperatures and having a low resistivity value for current flow between circuits and components. Ovrebo (2008) tested the thermal performance of four different die-attach materials used in high-power circuit boards under applied load of 90.3 °C on the SiC dies with epoxy die-attach materials. Three of the four die-attach materials studied were metallic and had excellent thermal conductivity. These materials were an Au/Sn braze, in an 80%/20% mixture; a CPES nanoscale silver powder; and Kester R520A solder paste, an alloy which is 96.5% Sn, 3.0% Ag, and 0.5% Cu, commonly called SAC. The fourth die-attach material was Epo-Tek P-1011 single-element polyimide epoxy. The physical properties of the die-attach materials required in the transient thermal transfer calculation are listed in Table 1.

Table 1: Physical properties of die-attach materials in transient thermal transfer simulation (Ovrebo, 2008).

Die-attach Material	Density (kg/m^3)	Specific Heat (J/kg.K)	Thermal Conductivity (W/m.K)
Au/Sn (80/20) braze	14510	150	57
Nanoscale silver	8580	233	200
SAC alloy solder paste	7400	220	57.26
Epo-Tek P1011 epoxy	3190	628	1.29

According to (He *et al.*, 2017), the thickness of the die-attach layer affects the thermal conductivity of the die-attach. As the thickness of the die-attach material decreases, the thermal resistance of the material decreases, and the thermal resistance of the die-attach materials caused by void fraction or number of bubbles discharged from the die-attach layer decreases. As shown in Equation 1, the thermal resistance of a material is proportional to its thermal conductivity coefficient, heat transfer area, and thickness.

$$R_{Th} = \frac{L}{kA} \tag{1}$$

where R_{Th} is thermal resistance, k and A is thermal conductivity coefficient and heat transfer area, respectively and L is the thickness of the die-attach material. According to the findings of the researcher (He *et al.*, 2017), the thermal conductivity of the die-attach layer is as high as 67W/m.K, with k being the main influencing factor. Because the void fraction is just about 7%, heat dissipation is effective, and the die-attach layer's thermal resistance is not affected by its thickness of around 2 μm.

Various conductive fillers used in the printed electronics industry, such as gold, titanium, carbon nanotubes, silver nanoparticles, organic conductive polymers, and graphene, can be used to replace printed circuit board (PCB) technology, thus lowering production costs. Due to its exceptional electrical, mechanical, and thermal properties, graphene as a filler has the potential to increase the efficiency, reliability and durability of numerous applications for the future generation of electronic devices, composite materials and energy storage devices (Olabi *et al.*, 2021). These incredibly fascinating properties along with high thermal conductivity suggest that graphene is an excellent candidate for applications in circuits beyond conventional complementary metal-oxide-semiconductor technologies and many other potential applications (Gong, 2011). Due to its exceptional electrical (Pokharel *et al.*, 2014), thermal (Tian *et al.*, 2014), and mechanical properties (Xu *et al.*, 2014), graphene has recently become a viable option for experimentation. Electronics (Bkakri *et al.*, 2014), bio-electric sensors (Lian *et al.*, 2014), energy technology (Abidin *et al.*, 2013), lithium batteries (Sun *et al.*, 2014), bio-engineering (Azeez *et al.*, 2013), aerospace (Aziz *et al.*, 2015), and a variety of other nanotechnology sectors (Agnihotri *et al.*, 2015) have all used graphene.

In this work, the use of graphene as the filler and copper as the substrate for reliability in conductive ink circuit is studied using a complete simulation circuit model. The simulation circuit models are ideal for conducting studies related to current circuit connectivity. Maximum temperature and maximum total heat flux are important for the reliability of a circuit. The study conducted on conductive ink is to determine the reliability of the circuit for different type of die-attach materials on the circuit lines and the state of the circuit at the thermal weak spots of each circuit line and die-attach connection. It is important to understand the properties of conductive ink. Different die-attach materials will have substantial thermal effect on the results. The influence of the conductive ink materials on the temperature and total heat flux in a circuit is investigated in an experimental investigation.

However, there is a lack of data on the thermal-induced by attachments, as well as the effect of different conductive ink materials and robustness on thermal dissipation. Experimental results can be used as an input parameter for material properties in FEA modelling to determine the maximum temperature and maximum total heat flux. This study aimed to demonstrate how different types of die-attach on a screen-printed straight-line design with conductive inks cause significant heat flow variance. It can be estimated using the maximum temperature and total heat flux generated by FEA modelling. The transient of maximum temperature and maximum total heat flux during heating might be optimised by using the transient thermal analysis in the circuit line. Following the completion of the above objective, an attempt was made to determine the best die-attach materials with the lowest temperature and total heat flux obtained from FEA modelling.

2. METHODOLOGY

This study aimed to determine which conductive inks with different die-attach materials would have the least amount of temperature and total heat flux. The lowest numerical results were then selected to analyse the time-dependent of the circuit. The FEA of the circuit was performed using numerical workbench tools.

2.1 Model Configuration

Data from previous studies and FEA models (Wahid *et al.*, 2021) were used in the research. Previous graphene material properties research was used, as well as simulated temperature and total heat flux values. The model was prepared with CATIA V5R21 and then the file was saved in IGES format and imported into the workbench software as shown in Figure 1. In this work, a transient thermal analysis was carried out to investigate the temperature and total heat flux variation across the graphene conductive inks circuit by applying temperature load value on the dies using ANSYS R16.0. Conductive inks patterns with a thickness of 0.1 mm were used to generate the FEA model. The circuit board substrate material of copper and silicon carbide (SiC) diodes were attached to the directly bonded graphene with die-attach materials. Conductive inks were the circuits that connect all of the diodes (die) directly. Die-attach was a type of adhesive or connector that connects the diode (die) to the conductive inks circuit.

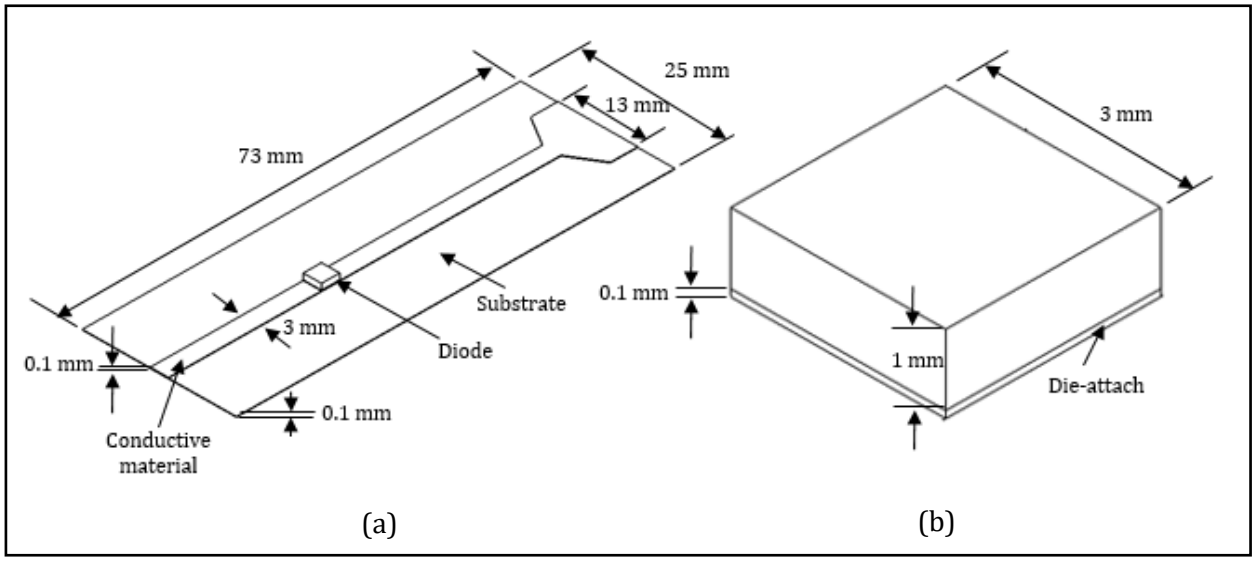

Figure 1: Model of the conductive inks circuit board. (a) Experiment setup. (b) Dimension of the die-attach material and die.

2.2 FEA

The results were determined by numerically solving the governing equations at each node using a mesh-generated finite element approach. As shown in Figure 2, the fine mesh option with tetrahedrons patch confirming (TPC) method was used with the straight-line model preference, and the computation process took some time. The finite element resulted in 31,094 nodes and 14,493 elements.

FEA of conductive inks thermal analysis on a screen-printed circuit using ANSYS software was used to simulate the circuit's thermal behaviour under heating load. The ink was approximated as a layered structure to imitate the screen-printing method. The study's purpose was to see how different die-attach materials affected the conductive inks resulting in heat flow. On the same substrate, the patterns were printed using the same printing and curing procedures. The focus of this research was to find out which die-attach materials are suitable for the conductive inks based on the least amount of temperature and total heat flux maximum values.

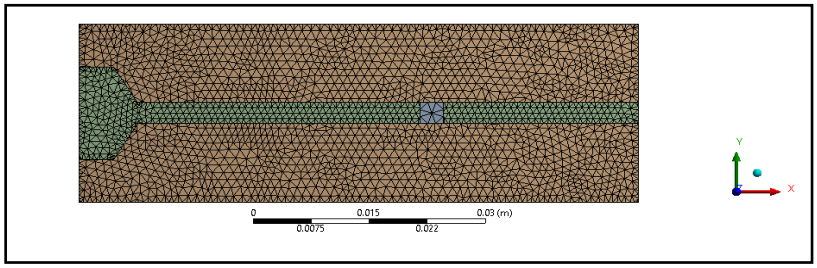

Figure 2: Mesh model of circuit board sample.

2.3 Boundary Conditions

The simulation began by defining the materials composing the circuit boards, along with their pertinent physical properties like thermal conductivity, specific heat, and density. The circuit substrate was copper, the lands on the circuit were graphene and the devices were silicon. For die-attach materials' physical properties and maximum temperature performed on semiconductor devices, this study used diodes as a reference (Ovrebo, 2008). Temperature and other thermal parameters varied over time in a transient thermal analysis, which was used to evaluate structural analysis in steady-state thermal research. In transient analysis, the induced loads are time functions that can be used to divide the load versus time curve into load steps (Ravikumar *et al.*, 2017). The SiC dies were designated as a volume heat source. The maximum temperature of 90.3 °C was applied to the SiC dies with metallic and epoxy die-attach materials within 0.5 second intervals; t = 0.5 s, t = 1.0 s, and t = 1.5 s, to compare thermal conductivity between all types of die-attach materials.

Heat flux is the rate of thermal energy flow per unit surface area of the heat transfer surface. In this study, the heat flux was applied to the SiC dies surface with metallic and epoxy die-attach materials within 1.5 seconds to compare thermal conductivity between all types of die-attach materials. From Equation (2), the total heat flux can be calculated on different die-attach materials circuits. The heat flux can be obtained by following Fourier's law of heat conduction:

$$q" = k\,(dT/dx) \tag{2}$$

where *q"* is heat flux (W/m^2), *k* and *dT* is thermal conductivity coefficient (measured in W/m K) and temperature of heat present on the top surface of the diode (measured in Kelvin), respectively and *dx* is the thickness of the materials (from the top surface of the diode to the bottom surface of the substrate). Figure 3(a) illustrates a schematic diagram of heat flows in the circuit. Figure 3(b) shows R_1, R_2, and R_3 representing die-attach material, graphene conductive ink, and copper substrate, respectively. These three materials were the resistances that the load applied to the diode. To acquire the total heat flux values of the circuit, the heat was transferred from the diode through the die-attach material, graphene conductive ink, copper substrate, and finally to the surrounding temperature of 17 °C. The simulated total heat flux value from ANSYS was compared with the calculated total heat flux value.

As illustrated in Figure 3(b), material resistance, R is given by the following;

$$R = \frac{dx}{k} \tag{3}$$

Where *dx* is the thickness of the materials and k is material thermal conductivity. By using the series method, the heat flux, *q"* can be obtained by following;

$$q" = \frac{\Delta T}{R_1+R_2+R_3} \tag{4}$$

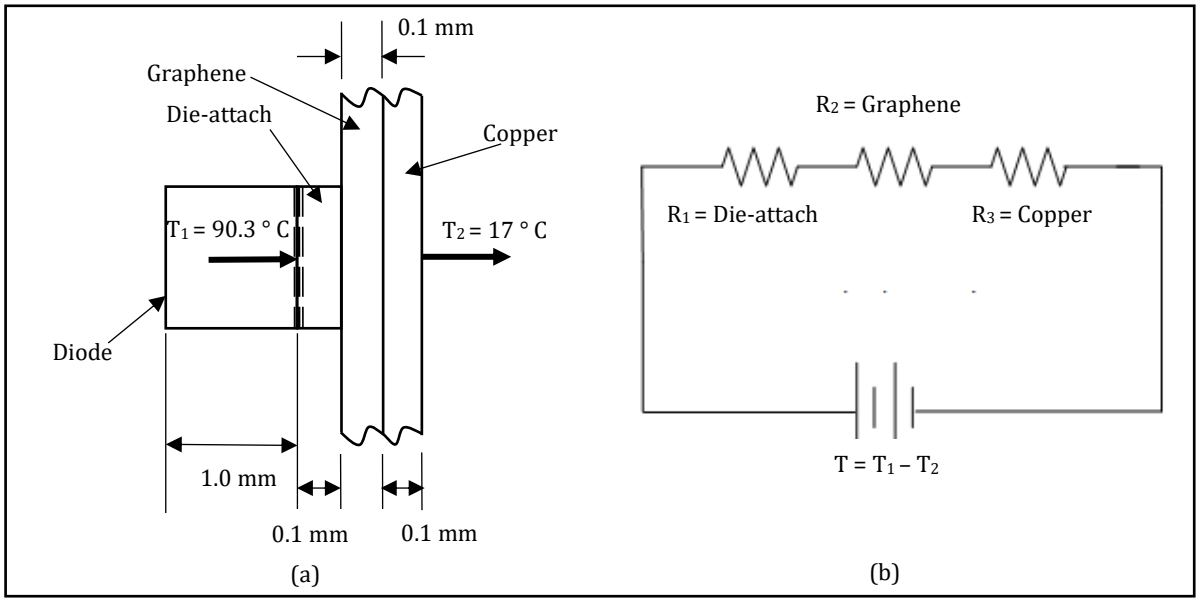

Figure 3: Schematic diagram of; (a) heat flows in the circuit. (b) heat conductance in series.

Where ΔT is the temperature difference across the materials. Table 2 demonstrates that, except for circuits that used epoxy die-attach material, all total heat flux values for each type of die-attach material are close to each other. This is because the thermal conductivity of epoxy is the lowest and very low when compared to other die-attach materials.

Table 2: Calculated total heat flux of die-attach materials circuit.

Material	Calculated Total Heat Flux (W/m^2)
Au/Sn (80/20) braze	3.3454×10^7
Nanoscale silver	3.8065×10^7
SAC alloy solder paste	3.348×10^7
Epo-Tek P1011 epoxy	0.4023×10^7

Table 3 shows the dependent and independent parameters chosen for this study. For each variation in independent parameters or combination of them, the output results obtained are four dependent parameters. This process can be repeated until all possible combinations are made (single, double, and triple faults). The conductive inks were used as circuits to connect all the diodes that use die-attach as adhesive. The simulation processed the independent parameters to generate results with dependent parameters. The total heat flux used the dependent parameters to learn the heat flow of the conductivity of the conductive ink and find the independent parameters that are affected by it. Heat flow performance was obtained from calculations with imposed conductivity specified as independent parameters from Figure 1. In addition, structural parameters such as the adhesive thickness and material properties are also dependent parameters that have the effect of conductivity development with the aid of thermal analysis.

Table 3: Chosen dependent and independent parameters.

Dependent parameters	Independent parameters
Conductive inks outlet temperature	Conductive inks heat flow
SiC dies outlet temperature	Diode area
Die-attach thickness	Die-attach heat flow
Substrate temperature	Substrate area

The material properties used for this FEA research are presented in Table 4. The material properties used in this paper are as obtained from previous research and other researchers.

Table 4: Material properties used for simulation analysis.

Materials	Properties			
	Density (kg/m^3)	**Thermal conductivity (W/m °K)**	**Specific Heat (J/kg-K)**	**Reference**
Graphene	2200	5300	5.09×10^5	Wahid *et al.*, (2021)
Copper	8300	401	385	ANSYS (2015)
SiC (Diode)	3100	120	750	Accuratus (2013)

3. RESULTS AND DISCUSSION

The modelling approach produced the best simulation results which accounted for the room temperature of the circuit at a constant 17 °C. Figures 4 and 5 show a surface plot of calculated surface temperatures and total heat flux, respectively on the board within 1.5 seconds of heating, with all four die-attach materials used in series. Before commencing the discussion on mesh and time refinement and various die-attach models, it is pertinent to present heat flow inside the circuit within the first 1.5 s. In both figures, the heat contour and the transient thermal on the conductive inks between 0.5 s and 1.5 s are presented.

Based on Figure 4 (a), the transient thermal data at 0.5 s shows the occurrence of divergence when the temperature spread to the entire circuit and shows the reaction of the temperature colour contour change on the circuit. Between 0.5 s and 1.0 s, the temperature spread with a high temperature to the substrate, and at 1.5 s, at 90.314 °C, the heat increasingly covers part of the area of the dies up to the substrate with a higher temperature. These temperature loads are observed in various time step sizes, mesh sizes, and circuit models presented in this paper. Figures 4 (b) and (c) are in the same scenario, except for Figure 4 (d), where die-attach epoxy material does not display variations in graphene land. The red portion is only on the diode that reaches the maximum temperature, and it begins to change colour from red to blue on the die-attach part.

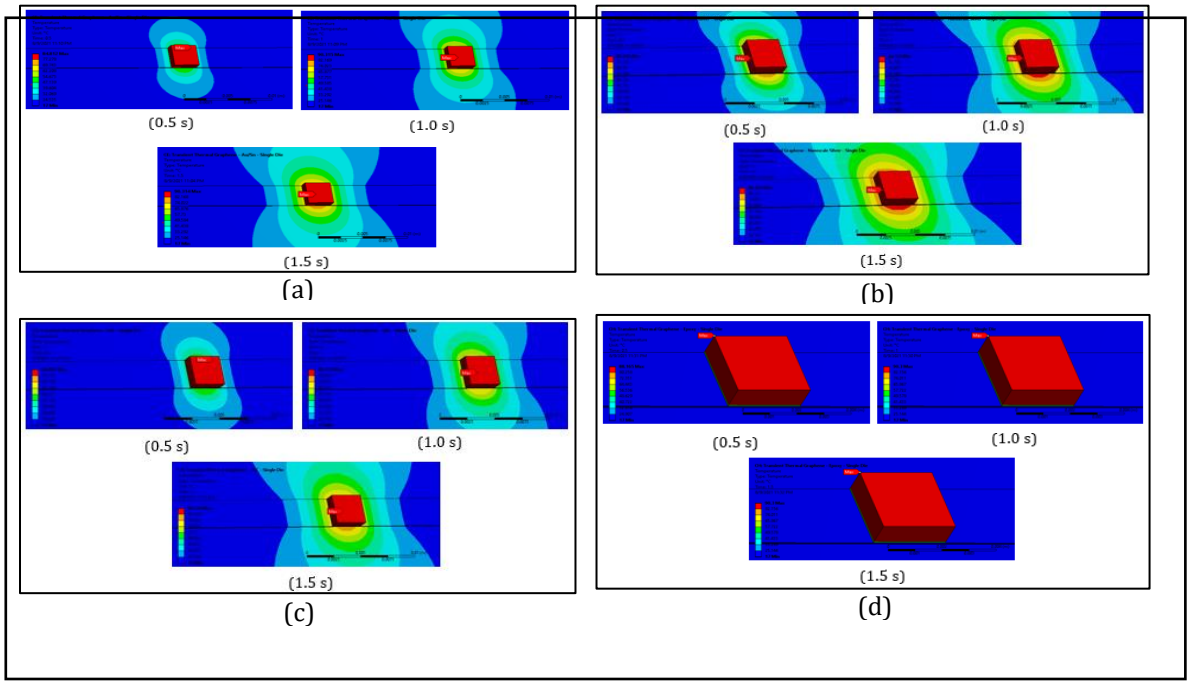

Figure 4: Temperature results of die-attach materials using transient thermal analysis. (a) Au/Sn (80/20) braze (b) Nanoscale silver, (c) SAC alloy solder paste, and (d) Epo-Tek P1011 epoxy.

Total heat flux or heat flow rate intensity results as shown in Figures 5 is a flow of energy per unit of area per unit of time in the circuit. The heat flux becomes higher after the time is increased. The adaptive time-stepping method was implemented in all four die-attach materials circuit models. The heat flows on the dies through die-attach materials to the conductive ink from 0 s to 1.5 s show a change in the colour contour on the surface of the circuit model. Figure 5 (a) shows the heat at 0.5 s generated between each die on the conductive ink surface. During the time change from 0.5 s to 1.0 s and 1.0 s to 1.5 s, the heat conduction expands along with the conductive ink. All four circuit models were initiated with the maximum allowed time step size that can maintain the stability of the solving process. Therefore, the same time-stepping method was used in all the circuit models. The same situation applies to Figures 5 (b), (c) and (d).

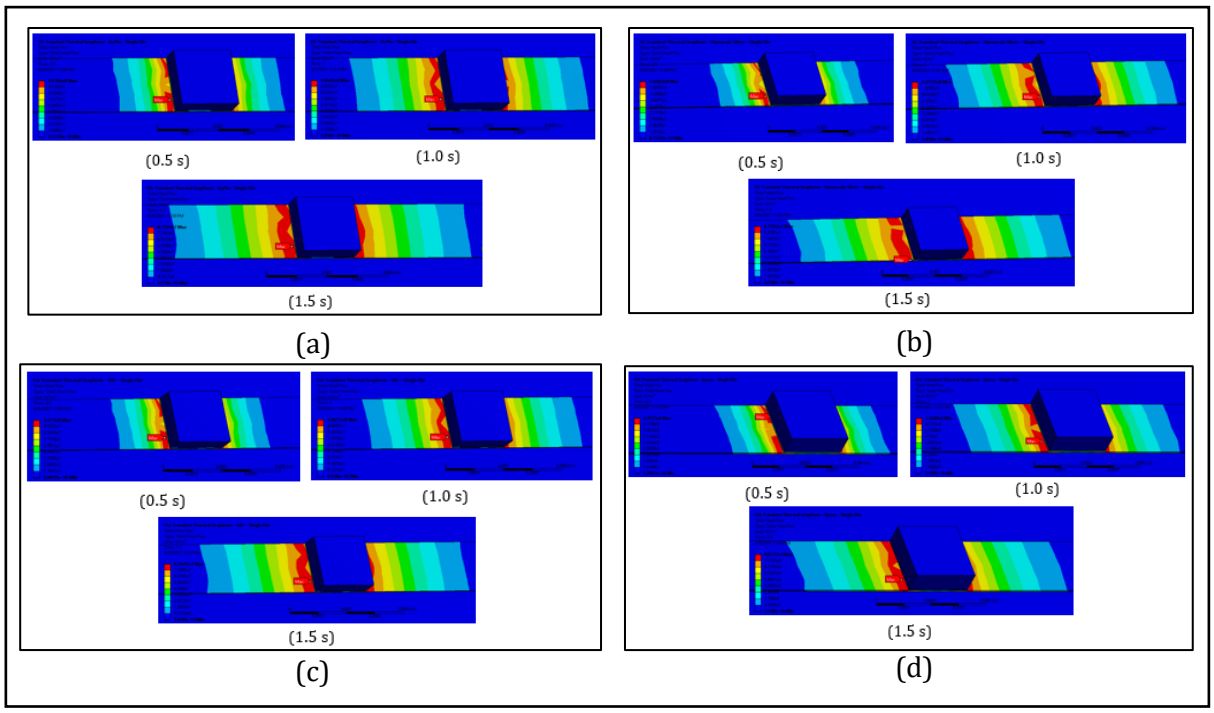

Figure 5: Total heat flux results of die-attach materials using transient thermal analysis. (a) Au/Sn (80/20) braze, (b) Nanoscale silver, (c) SAC alloy solder paste, and (d) Epo-Tek P1011 epoxy.

The results of the four die-attach materials show little variation in values. The transient thermal simulation results summarized in Table 5 show that the die-attach material, epoxy within time-dependent of 1.5 seconds has the lowest maximum temperature of 90.3 °C, and maximum total heat flux of 0.8073 x 10^7 W/m^2. The finding is consistent with the findings of calculated total heat flux, in which epoxy has the lowest thermal conductivity among other metallic die-attach materials. Despite the fact that epoxy has a lower thermal conductivity than metallic die-attach, the high specific heat value affects temperature conduction in the circuit. (Ovrebo, 2008). Nanoscale silver has the highest results of maximum temperature and total heat flux. Navarro *et al.* (2019) demonstrated this by conducting studies on Ag nanoparticles on copper as a substrate where the die-attached Ag nanoparticles can operate at high temperatures (Ag melting point 961 °C). This indicates that the heat transfer to the circuit on the silver nanoscale decreases due to the temperature differential on the diode (SiC) compared to the high thermal conductivity of the die-attach material. SAC alloy solder paste and Au/Sn (80/20) braze are two other metallic die-attach materials with temperature and total heat flux results that are practically identical when applying graphene conductive inks.

Table 5: Transient thermal results of die-attach materials simulation

Time (s)	Die-attach							
	Au/Sn (80/20) braze		Nanoscale silver		SAC alloy solder paste		Epo-Tek P1011 epoxy	
	Temp. (°C)	Total heat flux (W/m^2)	Temp. (°C)	Total heat flux (W/m^2)	Temp. (°C)	Total heat flux (W/m^2)	Temp. (°C)	Total heat flux (W/m^2)
0.5	84.812	10.706 x 10^7	85.079	16.465 x 10^7	84.807	10.73 x 10^7	88.165	0.4702 x 10^7
1.0	90.315	10.642 x 10^7	90.333	12.111 x 10^7	90.315	10.653 x 10^7	90.3	0.717 x 10^7
1.5	90.314	8.7595 x 10^7	90.325	9.2593 x 10^7	90.314	8.7641 x 10^7	90.3	0.8073 x 10^7

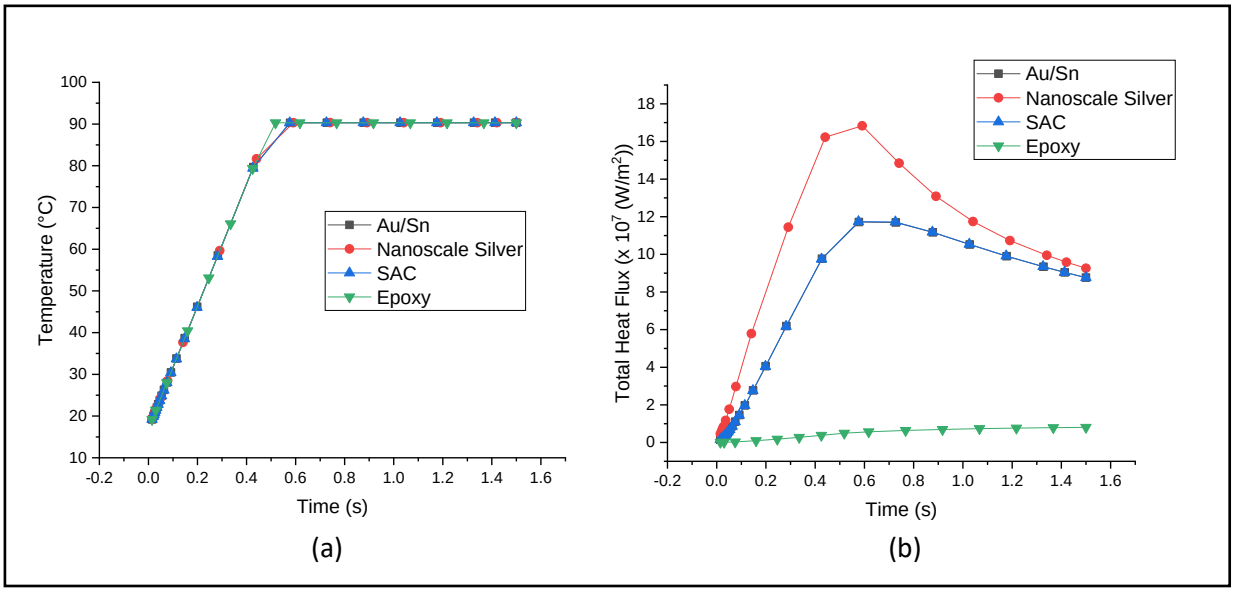

Figure 6: Trend of the lines probes during the test, comparison between all four die-attach materials specimen. (a) Temperature with respect to time. (b) Total heat flux with respect to time.

This simulation result can be varied by comparing the calculated total heat flux in Table 2 with the heat flux simulation result, which shows negligible changes. Figure 6(a) shows the linear relationship between temperature and time rise during heating within 1.5 s over a temperature range of 17 °C to 90.3 °C. Results showed that all die-attach material temperature increase as time increases but after about 0.6 s, the temperature from all die-attach materials circuits became flat or stable to the end. This is because the temperature became increasingly spread over the entire circuit, especially in graphene lands. The high thermal conductivity of graphene conductive ink allows for heat to spread over the material. A fitting line is established to determine a linear relationship with a temperature load of 90.3 °C. According to Figure 6(b), during the first 0.6 s of heating, the total heat flux of Au/Sn, nanoscale silver, and SAC increases dramatically, with the exception of epoxy (which only slightly increases), and then the total heat flux of Au/Sn, nanoscale silver, and SAC drops and becomes close to each other. This is demonstrated by the fact that epoxy has a substantially lower thermal conductivity than other die-attach materials. In comparison to other types of die-attach, the maximum total heat flux on the epoxy die-attach is the lowest. This demonstrates that epoxy provides high thermal resistance after measuring a temperature difference over a die-attach layer material with high thermal conductivity and 0.1 mm thickness. Because of the high thermal resistance, heat flows are more restricted through the epoxy die-attach. Metallic die-attach has a higher thermal conductivity than epoxy die-attach, which allows it to conduct temperature and heat more effectively.

Table 6 shows the calculated thermal resistance of die-attach materials obtained from Equation (1). The thermal conductivity coefficient and heat transfer area of a material are inversely proportional to its thermal resistance. The thermal resistance calculated on the die-attach layer is used to determine how much heat resistance the material possesses. The distance that heat must flow through the die-attach material is 0.1 mm, and the die-attach material's heat transfer area is 9×10^{-6} mm^2. The thermal conductivity value is determined by the type of die-attach material used. Thermal resistance decreases as thermal conductivity increases. The epoxy adhesive has the highest thermal resistance of all die-attach materials due to its low thermal conductivity value, which means that the temperature differential across the epoxy resists heat flow and heats the circuit for 1.5 s at a higher temperature than other adhesives. All of the metallic die-attach materials had lower predicted surface temperatures than epoxy die-attach materials. A small amount of heat is spreading across the circuit's face due to the use of high thermal resistance die-attach materials. If significant heat spreading had occurred, the diode would have influenced the whole circuit and raised the maximum temperatures on the diodes.

Table 6: Thermal resistance of die-attach materials.

Material	Thermal Resistance (°C/W)
Au/Sn (80/20) braze	0.195
Nanoscale silver	0.055
SAC alloy solder paste	0.194
Epo-Tek P1011 epoxy	8.61

4. CONCLUSION

By using transient thermal analysis, the study can effectively prove the optimal heat conductivity performance of various die-attach materials. A modelling approach based on previous research on conductive inks patterns related to thermal theories was developed and the varying effects of the different die-attach materials on graphene conductive ink materials were applied. Nanoscale silver gave the highest thermal value for conductive ink in terms of maximum temperature and total heat flux. The FEA indicated that the nanoscale silver, a metallic die-attach material, had the highest electrical conductivity and second-best thermal conductivity among metals with maximum temperature and total heat flux of 90.325 °C and 9.2593×10^7 W/m^2, respectively. Because of their low thermal conductivity, the findings of this transient thermal analysis were not considerably different, except for epoxy die-attach material, which had the lowest temperature and total heat flux value of 90.3 °C and 0.8073×10^7 W/m^2, respectively. All three die-attach materials produced close results between each other, in which the thermal conductivity and thickness could be the reasons. Temperature and heat flux conduction to the circuit are unaffected by the thinness of the die-attach materials layer. As the thickness of the die-attach material decreases, the thermal resistance tends to fall. As a result, epoxy die-attach materials with the best thermal resistance and lowest thermal conductivity have the potential to be good adhesives.

ACKNOWLEDGEMENT

Special thanks to the Advanced Manufacturing Centre (AMC) and Fakulti Kejuruteraan Mekanikal (FKM), Universiti Teknikal Malaysia Melaka (UTeM) for providing the laboratory facilities.

REFERENCES

Abidin, Z., Alim, M.A., Saidur, R., Islam, M.R., Rashmi, W., Mekhilef, S. & Wadi, A. (2013). Solar energy harvesting with the application of nanotechnology. *Renew. Sust. Energ. Rev*, **26**: 837-852.

Accuratus (2013) *Silicon Carbide Properties Datasheet*. Accuratus Corporation, Phillipsburg, New Jersey, US

Agnihotri, N., Chowdhury, A.D. & De, A. (2015). Non-enzymatic electrochemical detection of cholesterol using β-cyclodextrin functionalized graphene. *Biosens. Bioelectron*, **63**: 212-217.

ANSYS (2015). *ANSYS Release 16.0*. ANSYS Inc., Canonsburg, Pennsylvania, US.

Azeez, A. A., Rhee, K. Y., Park, S. J., & Hui, D. (2013). Epoxy clay nanocomposites–processing, properties and applications: A review. *Compos. Pt-B: Eng.*, **45**: 308-320.

Aziz, A., Lim, H. N., Girei, S. H., Yaacob, M. H., Mahdi, M. A., Huang, N. M. & Pandikumar, A. (2015). Silver/graphene nanocomposite-modified optical fiber sensor platform for ethanol detection in water medium. *Sensor Actuator B: Chem.*, **206**: 119-125.

Bkakri, R., Sayari, A., Shalaan, E., Wageh, S., Al-Ghamdi, A. A. & Bouazizi, A. (2014). Effects of the graphene doping level on the optical and electrical properties of ITO/P3HT: Graphene/Au organic solar cells. *Superlattice Microst*, **76**: 461-471.

Chidambaram, N.V., Ramachandra, C. & Vaideeswaran, J. (2017). Application of nano materials in thermal management of LEDs, *Int. J. Mat. Sci.*, **12**: 250-259.

Gong, J.R. (Ed.). (2011). *Graphene Simulation*. InTech, Rijeka, Croatia.

He, P., Zhang, J., Zhang, J, & Yin, L. (2017). Effects of die-attach quality on the mechanical and thermal properties of high-power light-emitting diodes packaging. *Adv. Mat. Sci. Eng.*, **Vol. 2017**: 8658164

Jiang, C., Fan, J., Qian, C., Zhang, H., Fan, X., Guo, W. & Zhang, G. (2018). Effects of voids on mechanical and thermal properties of the die attach solder layer used in high-power LED chip-scale packages. *IEEE T. Comp Pack. Man.*, **8**: 1254-1262.

Lian, Y., He, F., Wang, H. & Tong, F. (2014) A new aptamer/graphene interdigitated gold electrode piezoelectric sensor for rapid and specific detection of *Staphylococcus aureus*. *Biosens. Bioelectron*, **65C**: 314-319.

Melchor, L.A.N (2015). *Evaluation of Die Attach Materials for High Temperature Power Electronics Applications and Analysis of the Ag Particles Sintering Solution*. Doctoral dissertation, Universitat Autònoma de Barcelona, Barcelona, Spain.

Navarro, L.A., Perpiñà, X., Vellvehi, M., Aviño, O. & Jordà, X. (2019). Electrical behaviour of Ag sintered die-attach layer after thermal cycling in high temperature power electronics applications. *Surfaces*, **13**: 15.

Olabi, A.G., Abdelkareem, M.A., Wilberforce, T. & Sayed, E.T. (2021). Application of graphene in energy storage device–A review. *Renew. Sust. Energ. Rev.*, **135**: 110026.

Ovrebo, G. K. (2008). *Thermal Simulation of Four Die-Attach Materials*. Army Research Lab Adelphi Md Sensors and Electron Devices Directorate, Adelphi, Maryland, US.

Pokharel, P., Truong, Q.-T. & Lee, D.S. (2014) Multi-step microwave reduction of graphite oxide and its use in the formation of electrically conductive graphene/epoxy composites. *Compos. Pt-B*: *Eng.*, **64**: 187-193.

Ravikumar, S., Chandra, P.S., Harish, R. & Sivaji, T., (2017). Experimental and transient thermal analysis of heat sink fin for CPU processor for better performance. *IOP Conf Ser-Mat Sci* **197**: 012085.

Sun, W., Hu, R., Liu, H., Zeng, M., Yang, L., Wang, H. & Zhu, M., (2014). Embedding nano-silicon in graphene nanosheets by plasma assisted milling for high capacity anode materials in lithium ion batteries. *J. Power Sources*, **268**: 610-618.

Tan, K.S., Noordin, N.M., & Cheong, K.Y. (2017). An overview of die-attach material for high temperature applications. *AIP Conf. Proc.*, **1865**: 050011.

Tian, M., Qu, L., Zhang, X., Zhang, K., Zhu, S., Guo, X., Han, G., Tang, X. & Sun, Y. (2014). Enhanced mechanical and thermal properties of regenerated cellulose/graphene composite fibers. *Carbohyd. Polym.*, **111**: 456-462.

Wahid, A.K.A., Salim, M.A., Ali, M., Masripan, N.A., Dai, F. & Saad, A. M. (2021). Measurement of optimal stretchability graphene conductive ink pattern by numerical analysis. *Defence S&T Tech. Bull.*, **14**: pp. 43-54

Wei, Z., Ni, Z., Bi, K., Chen, M. & Chen, Y. (2011). Interfacial thermal resistance in multilayer graphene structures. *Phys. Lett. A*, **375**: 1195-1199.

Xu, Z., Zhang, J., Shan, M., Li, Y., Li, B., Niu, J., Zhou, B. & Qian, X. (2014) Organosilane-functionalized graphene oxide for enhanced antifouling and mechanical properties of polyvinylidene fluoride ultrafiltration membranes. *J. Membrane Sci.*, **458**: 1-13.

STUDY ON BRAKING EFFICIENCY OF MILITARY ARMOURED VEHICLES IN MALAYSIAN TROPICAL ENVIRONMENT

Shamsul Akmar Ab Aziz* & Fadzli Ibrahim

Mechanical & Aerospace Technology Division, Science and Technology Research Institute for Defence (STRIDE), Ministry of Defence, Malaysia

*E-mail: shamsulakmar.abaziz@stride.gov.my

ABSTRACT

Malaysia as a tropical country presents a challenge to vehicle manufacturers, especially military vehicles, in ensuring that the vehicles developed are able to meet the requirements of the variety of terrain profiles. Braking efficiency measurement is one of the tests that should be carried out to ensure that the vehicle is able to operate efficiently and safely. Realising that the performance of vehicles tested in the country of manufacture will not be the same as when operated in the actual field in Malaysia, an initiative has been taken to create a database of army vehicle performance, especially from the aspect of braking capability on the actual road surface. From the braking efficiency test results, it was found that there was a slight difference in the braking efficiency values for all military vehicles according to vehicle wheel drive – 8x8, 6x6 and 4x4. On the whole, the braking efficiency values for the three categories of armoured vehicles met the international standard of 50%.

Keywords*: Terrain profiles; braking efficiency; military vehicle; stopping distance; time to stop.*

1. INTRODUCTION

Malaysia is a tropical country with a variety of terrain profiles. These diverse terrain conditions present a challenge to vehicle manufacturers, especially military vehicles, in ensuring that the vehicles that they develop can meet the requirements of these terrains. For example, Aziz *et al*. (2017) demonstrated that the interaction between road surfaces and car tyres has a major effect on the noise generated inside passenger vehicle cabins, with rough roads exhibiting higher noise exposure variation as compared to smoother tarmacs. The capability of a vehicle measured by international standards should meet the prescribed safety and capability characteristics. In Malaysia, a military vehicle is tested by an evaluation team before it can be used in actual operations. Among the tests carried out include operating in muddy areas, sandy surfaces and river banks. Apart from vehicle performance tests, human comfort tests such as noise, whole-body vibration (WBV), hand-arm vibration (HAV) and heat stress are performed for vehicle drivers driving various military vehicles (Aziz *et al*., 2008, 2009, 2014, 2015, 2016, 2017; Gani & Aziz, 2008; Khan *et al*, 2010).

In order to ensure that a vehicle can withstand all the required tests, brake performance measurement must first be carried out to ensure that the vehicle is able to operate efficiently and safely. Thus, determination of braking efficiency values for vehicles operating in Malaysian road surfaces is important to be established as it reflects the actual road surface situation. Braking efficiency is a basic index for the evaluation of automobile braking performance, mainly including ground braking force, braking deceleration, braking distance and braking time (Chen, 2015; Šarkan *et al*., 2020; Volkov *et al*., 2021)

The braking efficiency test is one of the tests that must be performed on a military vehicle in fulfilling the procurement process. Although a military vehicle built by an overseas manufacturer is able to meet the standards set, the performance of vehicles tested in the country of manufacture will not be the same as when operated in the actual field in Malaysia. Therefore, an initiative has been taken to

create a database of military vehicle performance, especially from the aspect of braking capability on the actual road surfaces in Malaysia. The development of this database aims to analyse the braking capability patterns for each military vehicle tested and subsequently to develop its own standards that can be used as a reference in the future.

This study was conducted by the Science & Technology Research Institute for Defence (STRIDE) on several Malaysian Army armoured vehicles involving a series of tests during the evaluation and final acceptance test (FAT) of the vehicle procurement procedure. The list of vehicles tested is divided into three categories based on the type of vehicle drive - 8x8, 6x6 and 4x4. Table 1 shows the number and weight of armoured vehicles that have been tested by vehicle category.

Table 1: Tested armoured vehicles.

Category	Number of Vehicles	Vehicle Weight (Tonnes)
8x8	2	28 - 30
6x6	2	16 - 24
4x4	4	8 - 14

2. RESEARCH METHODOLOGY

Braking efficiency is defined as the ratio of retarding force or braking force to the weight of the vehicle, expressed as a percentage. Theoretically, if the retardation is equal to acceleration due to gravity, the braking efficiency would be 100%, a value that is seldom found in practice (Amedorme & Fiagbe, 2013). The value of the braking efficiency of a vehicle is obtained from the following equation:

$$\text{Braking efficiency} = \frac{F}{m\,g} \tag{1}$$

where F is the force while pressing the brake pedal in N, m is the weight of the vehicle tested in kg, and g is the gravitational acceleration value of 9.81 m/s^2.

Before the test was carried out, the tire air pressure and vehicle condition were checked to be at the recommended level. This test required a flat, paved road surface. This was based on the STRIDE test protocol (Adam *et al.* 2009) and performed at speed of 32 km/h (Turnkey 2001). Although the test is performed on a flat area, the results would be the same for other terrain profiles. Through the above formula, the value of braking efficiency is not closely related to the type of test surface whether pavement, dirt road or other road surfaces. The test was performed using a Turnkey portable brake tester (Figure 1), which provides results such as the value of braking force, braking distance and degree of turning when the brakes are applied. These parameters were analysed to obtain the data required in this study.

According to DVSA (2018), braking efficiency performance has different values according to the type of vehicle, such as number of tires and type of brakes used. The recommended braking efficiency value for vehicles manufactured before 1968 was only 25%, but the value increased to 58 % for new vehicles after 2010. In addition, the manufacturer of brake tester equipment (Turnkey, 2001) stated the braking efficiency for service brakes should be at least of 50%. Puspakom Sdn. Bhd. (PUSPAKOM) is the only company appointed by the Government of Malaysia to conduct vehicle inspections as well as to conduct braking efficiency tests. PUSPAKOM (2021) provides the values of braking efficiency according to type and weight of vehicles, which is between 45 and 58%.

Figure 1: Turnkey brake tester (Turnkey, 2001).

3. RESULTS AND DISCUSSION

In order to analyse the braking efficiency of the vehicles, three parameters were taken into account, namely braking efficiency, stopping distance and stopping time when the brakes were applied.

3.1 Braking Efficiency

Based on the standards adopted by STRIDE, the percentage of braking efficiency should not be less than 50%, which is the same level of efficiency used by DVSA (2018). The percentages of braking efficiency for the three vehicle categories are shown in Figure 2. Based on the figure, it is found that the braking efficiency for the 8x8 vehicles is 50.2 %, 53.3% for the 6x6 vehicles and 54.9% for the 4x4 vehicles. Given the state of the test site in Malaysia, based on the results obtained, in order to ensure that the braking efficiency values of the tested armoured vehicles are in line with the capability and safety of a vehicle for military use, the minimum recommended values of braking efficiency for each armoured vehicle category are as proposed in Table 2.

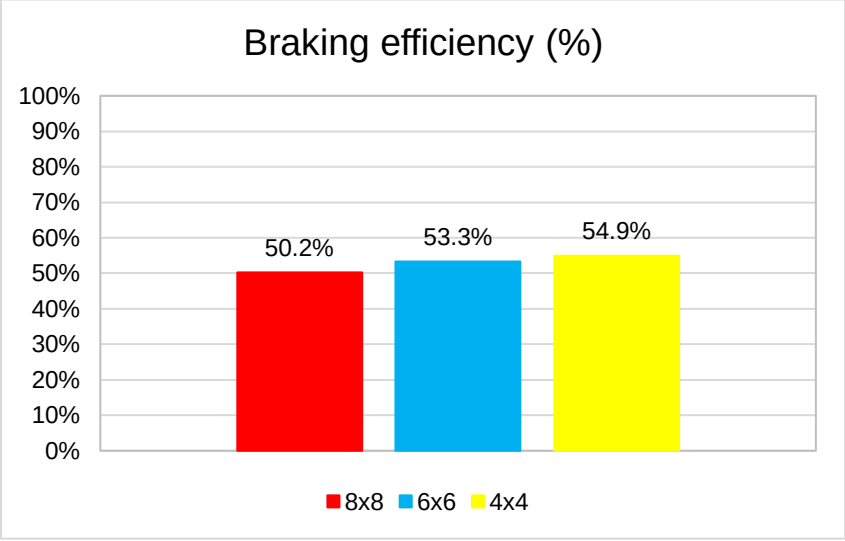

Figure 2: Braking efficiency for different vehicle categories.

Table 2: Proposed braking efficiency values for different military armoured vehicle categories.

Vehicle Category	Minimum Braking Efficiency (%)
8x8	50
6x6	53
4x4	55

3.2 Stopping Distance and Time to Stop

The stopping distance and time to stop for the three vehicle categories are shown in Figures 3 and 4 respectively. From the data obtained, it is shown that the stopping distance of the 8x8 vehicles is 8.5 m in 1.9 s. For the 6x6 vehicles, the stopping distance is 8.3 m in 1.8 s, while for the 4x4 vehicles, it is 8.2 m in 1.7 s. The weight of a vehicle determines the stopping distance based on the data obtained. Figure 5 shows the relationship between stopping distance and time to stop for the three vehicle categories. It shows that stopping distance is directly proportional to time to stop for all three vehicle categories.

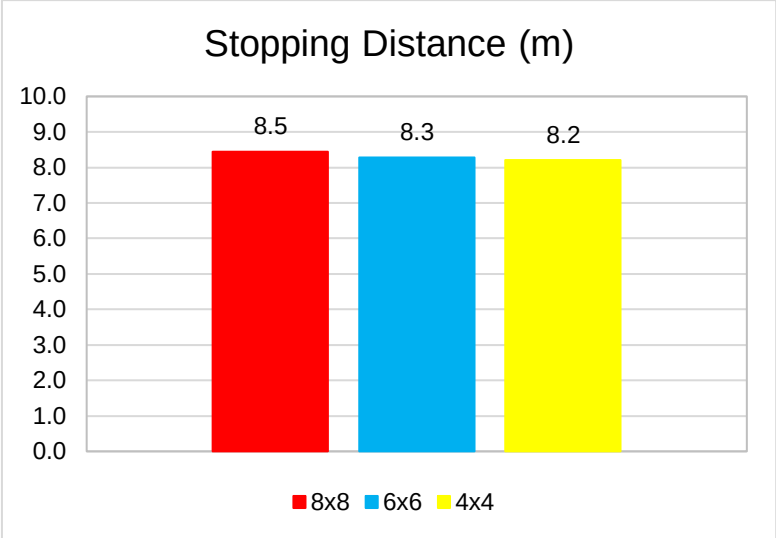

Figure 3: Stopping distance for different vehicle categories.

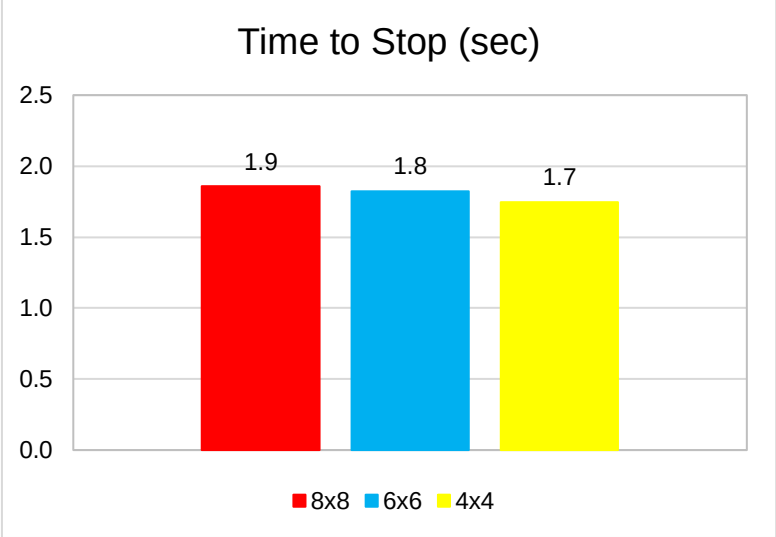

Figure 4: Time to stop for different vehicle categories.

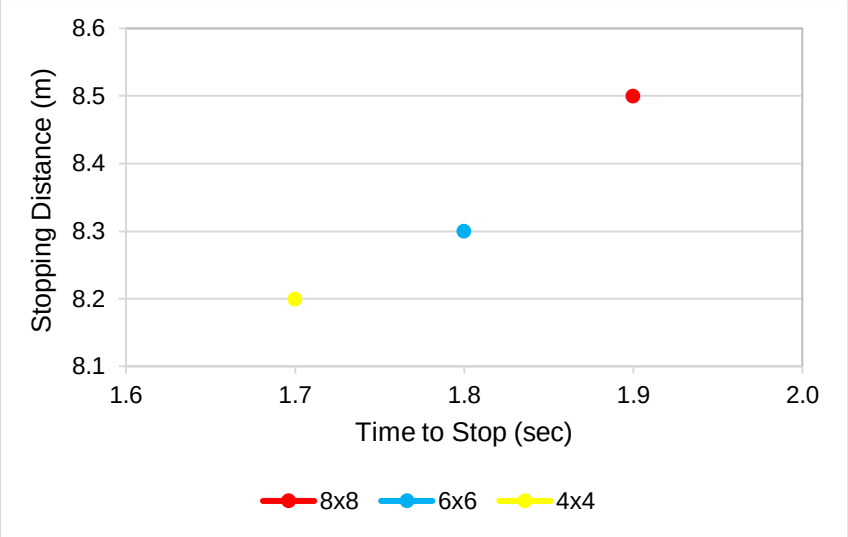

Figure 5: Correlation between stopping distance and time to stop for different vehicle categories.

4. CONCLUSION

From the braking efficiency test results, it was found that there were slight differences in the braking efficiency values for all the military vehicles according to vehicle wheel drive. Based on vehicle capability and safety for driver, passenger, and vehicle itself, the minimum recommended values of braking efficiency for each armoured vehicle category were proposed. Overall, the braking efficiency values for the three categories of armoured vehicles met the basic requirement. For improvement, future analysis will be carried out more comprehensively based on more detailed vehicle testing data for each vehicle category.

REFERENCES

Amedorme, S.K. & Fiagbe, Y.A.K. (2013). Investigation of braking system (efficiency) of converted Mercedes Benz buses. *Int. J. Sci. Tech.*, **2**:754-762.

Aziz, S.A.A., Gani. A. & Hassan, A.H. (2008). Whole body vibration (WBV) on Malaysian Armed Forces (MAF) vehicles. *Defence S&T Tech. Bull.*, **1**: 7–15.

Aziz, S.A.A., Gani. A. & Hassan, A.H. (2009). Pass-by noise of Malaysian Armed Firces (MAF) vehicles. *Defence S&T Tech. Bull.*, **2**, 10–19.

Aziz, S.A.A., Nuawi, M.Z, Nor, M.J.M. & Daruis, D.D.I. (2014). Study of noise exposure inside a Malaysian Army three-tonne truck driver's compartment using I-Kaz™. *Defence S&T Tech. Bull.*, **7**:107–111.

Aziz, S.A.A., Nuawi, M.Z. & Nor, M.J.M. (2015). New regression model for predicting hand-arm vibration (HAV) of Malaysian Army (MA) three-tonne truck steering wheels. *J. Occup. Health*, **57**: 513–20.

Aziz, S.A.A., Nuawi, M.Z. & Nor, M.J.M. (2016). Predicting whole-body vibration (WBV) exposure of Malaysian Army three-tonne truck drivers using integrated kurtosis-based algorithm for Z-notch. filter technique 3D (I-Kaz 3D). *Int. J. Ind. Ergon.*, **52**: 59–68.

Aziz, S.A.A., Nuawi, M.Z. & Nor, M.J.M. (2017). Monitoring of hand-arm vibration. *Int. J. Acoust. Vib.*, **22**: 34-43.

Aziz, S.A.A, Gani, A., Suhaimi, A.F., Kalil, S.., Yusuf, A.Y & Nuawi, M.Z., (2017). Noise exposure inside a passenger car cabin in tropical environmental condition. *Defence S&T Tech.*, **10**: 290-296.

Chen, P. (2015). The testing and data analyzing of automobile braking performance. *Int. Conf. Comput. Sci. Eng. 2015 (ICCSE 2015)*, pp. 440-444.

DVSA (Driver & Vehicle Standards Agency) (2018). *Inspection Manual: Cars and Passenger Vehicles*. Driver & Vehicle Standards Agency (DVSA), Nottingham, UK.

Gani. A. & Aziz, S.A.A., (2008) Heat stress on various types of military vehicles in malaysian climate. *Defence S&T Tech.*, **1**: 16-29.

Gani, A., Aziz, S.A.A. & Hassan, A.H. (2009). Test protocol for Malaysian Armed Forces (MAF) vehicles - Health hazard assessment (HHA) and vehicle performance. *Defence S&T Tech.*, **2**: 1-9.

Khan, M.K.J., Gani. A., Aziz, S.A.A. & Hassan, A.H., (2010). Determination of whole body vibration (WBV) of main battle tank (MBT) PT-91M. *Defence S&T Tech.*, **3**: 29–35.

PUSPAKOM. (2021). *Inspection Standards*. Available online at: https://www.puspakom.com.my/inspection-standards (Last access date: 28 February 2022).

Šarkan, B., Jaśkiewicz, M. & Kiktová, M. (2020). The impact of the truck loads on the braking efficiency assessment. *Open Eng.*, **10**: 105-112.

Turnkey, (2001). *BrakeSafe Operating Operations*. Turnkey Instruments Ltd., Northwich, UK.

Volkov, V., Gritsuk, I., Volkova, T., Berezhnaja, N., Pliekhova, G., Bulgakov, M., Marmut, I. & Volska, O. (2021). *System Approach to Forecasting Standards of Vehicles' Braking Efficiency*. SAE International, Warrendale, Pennsylvania, US.

APPLICATION OF DESIGN FOR MANUFACTURING AND ASSEMBLY (DFMA) METHOD TO VEHICLE DOOR DESIGN

Md Fahmi Abd Samad*[1, 2] & Kjeldsen Yusuf @ George[1]

[1]Faculty of Mechanical Engineering
[2]Centre for Advanced Computing Technologies
Universiti Teknikal Malaysia Melaka (UTeM), Malaysia

*Email: mdfahmi@utem.edu.my

ABSTRACT

Design for manufacturing and assembly (DFMA) guidelines aim to reduce part count, number of welds and number of operations. By doing so, production advantages such as shorter production time, higher management efficiency and greater customer satisfaction are achieved. In this paper, the effectiveness of the DFMA method was shown in vehicle door design. Two vehicle door designs were taken apart to investigate the feasibility of better designs using the Boothroyd and Dewhurst analysis. It employed quantitative analysis of various parts of the design, such as door frame, door board and screws. Each part of the design was rated with a numerical value depending on its assembly requirements. The product was then redesigned, using the numerical values as a goal to be minimised. Various factors concerning assembly were considered, such as symmetry and size of part. The outcome was designs that have shorter assembly time and assembly efficiency higher than 15%.

Keywords: *Assembly efficiency; automotive; design for manufacturing and assembly (DFMA); DFMA index; vehicle door design.*

1. INTRODUCTION

Ground automotive vehicles have been in use in many areas of our lives. In defence applications, vehicles are used to either transport troops to strategic locations or, with the ones equipped with weapons, for combat. They are designed in a variety of constructions and the lightweight ones are known by names such as military vehicle, utility vehicle, fighting vehicle, etc., and historically, originated from commercial civilian vehicles (Military-Today, 2021). Their modifications can still be found today, especially for fixing weapons and grafting armour. It is not unusual to note Toyota Hilux pickup trucks or Chevrolet Camaro cars to have been redesigned as military vehicles (Petrány, 2014).

When it comes to modifying a vehicle's design, one has to consider the body to be the biggest concern in terms of impact, time, cost and customer satisfaction. In terms of impact, the body is the part of a vehicle that has the most outstanding feature throughout a vehicle (Genta *et al*., 2014). Many vehicle designs begin with a layout of the vehicle's body. Models are often redesigned with completely new bodies. The vehicle body manufacturing always demand much time and stays on the critical vehicle development path. This is true as installing other parts to the body require much systematic approach to ensure efficient production. Related tooling needs to be developed to ensure production runs according to market demand. Alongside the power train, the cost for the body is one of the most costly vehicle system (Genta *et al.*, 2014). It is always important to consider the increase in cost when new changes are made to the body.

Many companies have turned to design for manufacturing and assembly (DFMA) to improve the design of their products and achieve competitive advantage. The data collected by McDonnell Douglas, an aerospace manufacturing company at St Louis on over 50 case studies revealed that many companies have achieved good results using the DFMA methodology (Herrera, 1997). Some of the

results are reduction in manufacturing cycle time, part count reduction, part cost reduction, time-to-market improvements, quality and reliability improvements and reduction in assembly time. The practice, known as the combination of design for assembly (DFA) and design for manufacturing (DFM), had their starts in the late 1970's at the University of Massachusetts (Boothroyd, 1994; Herrera, 1997). Between the two, companies are mostly interested in DFA.

Many have pointed out the advantages of using DFMA. Some recent applications include the application of DFA and DMA in washing machine design, where the authors concluded that the study as achieved an acceptable cost estimation (Annamalai, 2013). Da Silva *et al*. (2013) mentioned that DFMA enabled finding opportunities for improvement as they are applied for electronic voting machine printers. Barbosa & Carvalho (2013), who applied DFMA on aircraft electrical system design, listed the advantages as allowing low cost, high quality and best optimised condition. Yuan *et al*. (2018) mentioned good manufacturability and assemblability when applied in the construction industry. Tasallato *et al*. (2016) demonstrated DFMA application with welding as an independent design module, while Kim *et al*. (2016) applied it in bridge design. In the automotive industry, Suresh *et al*. (2015) studied the environmental impact of a charge alternator pulley designed using DFMA, while Ardayfio *et al*. (1998) applied DFMA in automotive electrical and electronic systems.

This paper focuses the applicability of DFMA to the design of vehicle doors. It begins with a reverse engineering approach to chosen vehicle models and followed by design analysis. The aim is to further simplify the design so that newly recommended designs allow better efficiency in its production, particularly in terms of assembly time and cost reduction.

2. BACKGROUND

2.1 Design for Assembly (DFA)

According to Kuo *et al*., (2001), DFA was pioneered by Boothroyd and Dewhurst. It began with the aim of reducing assembly cost by having the easiest method of assembly. This in turn is achieved by redesigning the parts. They classified the assembly system into three basic types, namely, manual, special-purpose machine and programmable machine assembly. Later on, they wrote a book called *Product Design for Assembly Handbook* that helped designers assign parts of an assembly with ratings based on the part's ease of handling and insertion.

The handbook described how design features may have constraints that slow down assembly, and hence increase production cost. Following this, Kuo *et al*. (2001) reported that other researchers introduced similar methods in rating parts or components to the extent of how easy (or difficult) they are to assemble. Some recent innovative ideas regarding this may be found in Harik & Sahmrani (2010) and Ahmad *et al*. (2018). Their works proved to provide cost reductions in product assembly.

2.2 Design for Manufacturing (DFM)

DFM is related to the process of selecting the appropriate processes for the manufacture of a particular part. This is based on the match between the part attributed to process capabilities. Among the considerations are raw material selection, process selection, modular design, standard component usage, multi-use part development, separate fasteners usage and assembly minimisation (Kirkland ,1988; Kuo *et al.*.2001).

DFM has been proven to be able to help companies achieve cost reduction estimation from the early stage of design. The method is known to be applicable in machining parts, injection molds, sheet metal stamping, die cast parts, construction and powder parts (Bogue, 2012; Gao *et al.*, 2020)

2.3 Similar Methods

There are a number of methods those are associated with DFMA. This includes the Lucas DFA methodology, which was adopted in Ahmad *et al*. (2018). In the Lucas DFA methodology, the processes are separated into three stages: (1) Function analysis, (2) Handling analysis, and (3) Fitting analysis. All the processes are carried out throughout the design process in order to identify the most cost-effective approach of the design.

Other well-known methods are the Cyber Cut and the Nippondenso methods (Whitney, 1993; Harik & Sahmrani, 2010). The Cyber Cut method simplifies the design by removing non-essential features of a product. The simplified design then is run through computer numerical control (CNC) machining processes. The Nippondenso method is better known for having sets of designs that are interchangeable. This reduces the need to have extra jigs and fixtures for new products.

3. METHODOLOGY

The study was carried out using a DFMA software based on the Boothroyd and Dewhurst analysis. The software can quickly calculate the costs involved for different materials and manufacturing processes as well as identify areas where the number of parts can be reduced.

Several important rules when evaluating part manual assembly are to:

- Reduce part count and type
- Eliminate necessity for adjustments
- Allow parts to be self-aligned and self-locating
- Ensure adequate access and vision
- Ensure ease of handling when parts are in bulk
- Minimise re-orientation
- Design parts that cannot be incorrectly installed
- Maximise part symmetry or make parts clearly asymmetrical

Several stages are carried out when implementing DFMA and the implementation is represented as in Figure 1 (Boothroyd *et al.*, 2010).

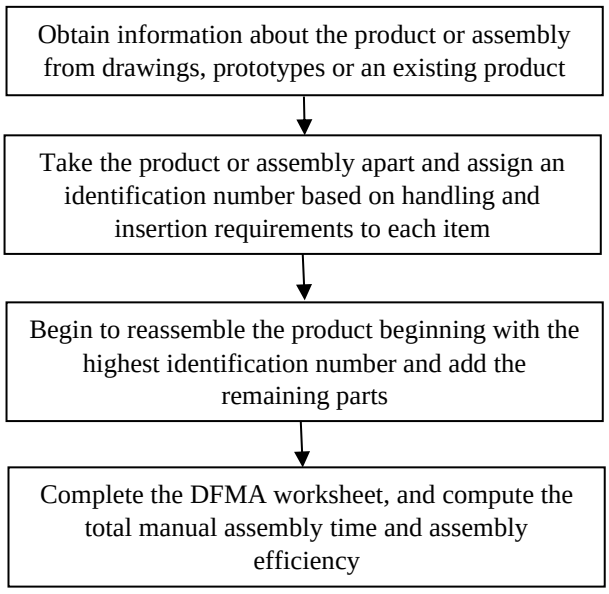

Figure 1: Stages of DFMA application.

In the third stage, when beginning to reassemble the product, at each stage of assembly:

- Rows of the DFMA worksheet is filled for each part respectively.
- Never assume that parts are grasped one in each hand and then assembled together first before placing them in a partially-completed assembly.

The study was focused on manual assembly where, based on Boothroyd *et al*. (2010), it can be divided naturally into two separate areas: (1) Handling (acquiring, orienting and moving the parts), and (2) Insertion and fastening (mating a part to another part or group of parts).

The assembly efficiency, which is known as the DFMA index (E_{ma}), is calculated based on:

$$E_{ma} = 3 \times N_{min} / t_{ma} \quad (1)$$

where:

N_{min} : theoretical minimum number of parts
t_{ma} : total assembly time

4. RESULTS

4.1 Vehicle Door 1

Shown in Figure 2 are two among many components of the first vehicle door that was disassembled and given identification numbers.

Figure 2: Component and one of the screw types of Vehicle Door 1.

Following the disassembly exercise, the components were then counted, given their handling and insertion codes. From their handling and insertion codes, handling and insertion times were calculated and hence, from the sum, assembly time for the parts was obtained. Analysis was done to identify strategies to simplify the design according to the rules provided and so, some parts were able to be eliminated. Table 1 shows the results before and after simplification (part elimination) of the design.

Table 2 shows the overall results of a new design developed after implementation of DFMA. Based on the criteria provided in the Boothroyd and Dewhurst analysis, the theoretical minimum number of parts is set as nine.

Table 1: Before and after simplification of Vehicle Door Design 1.

		Before part elimination		After part elimination	
No.	**Name of Part**	**Quantity**	**Assembly Time (s)**	**Quantity**	**Assembly Time (s)**
1	Door Frame	1	12	1	12
2	Door Board	1	10.10	1	10.10
3	External Door Handle	1	3	1	3
4	Internal Door Handle	1	2.63	1	2.63
5	Automatic Door Lock	1	15.6	1	15.6
6	Window Bar	1	5.34	1	5.34
7	Glass Window	1	11.50	1	11.50
8	Power Window	1	14.60	1	14.60
9	Side Mirror	1	2.63	1	2.63
10	Flat Head Screw	3	21.30	2	14.20
11	Pan Head Screw	3	21.30	2	14.20
12	Round Head Screw 1	6	42.60	4	28.40
13	Round Head Screw 2	6	42.60	4	28.40
14	Round Head Screw 3	1	7.10	1	7.10
15	Oval Head Screw	2	14.20	2	14.20
16	Indented Hexagon Washer Head Screw 1	2	14.20	2	14.20
17	Indented Hexagon Washer Head Screw 2	6	42.60	4	28.40
18	Indented Hexagon Washer Head Screw 3	2	14.20	2	14.20
19	Indented Hexagon Washer Head Screw 4	1	7.10	1	7.10
	Total	41	304.6	33	247.80

Table 2: Comparison of before and after DFMA application on Vehicle Door Design 1.

	Old design	**New design**	**% Change**
Number of parts	41	33	19.50 % reduction
Assembly time (second)	304.60	247.80	18.65 % reduction
Assembly efficiency (%)	9	11	22.2 % increment

By using DFMA, as many as eight parts were identified as suitable to be taken out from the assembly. No component was completely removed but the quantity was reduced. The reductions were as follows:

- Flat head screw from three to two parts
- Pan head screw from three to two parts
- Round head screw 1 from six to four parts
- Round head screw 2 from six to four parts
- Indented hexagon washer head screw 2 from six to four parts.

4.2 Vehicle Door 2

Shown in Figure 3 are two of the components of the second vehicle door that has been disassembled and given identification number.

Figure 3: Component and one of the screw types of Vehicle Door 2.

For this design, 15 different components were identified. Aside from six types of fasteners, the components were the same as Design 1. Table 3 shows the results before and after simplification (part elimination) of the design.

Table 3: Before and after simplification of Vehicle Door Design 2.

		Before part elimination		After part elimination	
No.	**Name of Part**	**Quantity**	**Assembly Time (s)**	**Quantity**	**Assembly Time (s)**
1	Door Frame	1	12	1	12
2	Door Board	1	10.10	1	10.10
3	External Door Handle	1	3	1	3
4	Internal Door Handle	1	2.63	1	2.63
5	Automatic Door Lock Device and Component	1	15.60	1	15.60
6	Window Bar	1	5.34	1	5.34
7	Glass Window	1	11.50	1	11.50
8	Power Window Component	1	14.60	1	14.60
9	Side Mirror	1	2.63	1	2.63
10	Round Head Screw	2	14.20	2	14.20
11	Flat Head Screw	3	21.30	2	14.20
12	Washer Head Screw	3	21.30	2	14.20
13	Indented Hexagon Washer Head Screw 1	8	56.80	5	35.50
14	Indented Hexagon Washer Head Screw 2	2	14.20	2	14.20
15	Indented Hexagon Washer Head Screw 3	1	7.10	1	7.10
	Total	28	194.30	23	176.80

Table 4 shows the result of a new design developed after implementation of DFMA for Vehicle Door 2. The theoretical minimum number of part is set as nine. For this design, only five parts were eliminated. Again, no component was completely removed but the quantity was reduced. The reductions were as follows:

- Flat head screw from three to two parts
- Washer head screw from three to two parts
- Indented hexagon washer head screw 1 from eight to five parts.

Table 4: Comparison of before and after DFMA application on Vehicle Door Design 2.

	Old design	New design	% Change
Number of parts	28	23	17.90 % reduction
Assembly time (second)	194.30	176.80	9 % reduction
Assembly efficiency (%)	13	15	15.4 % increment

5. DISCUSSION

The original assembly time is fairly large. This is because many parts in these case studies require two hands for manipulation. Some are heavy (door frame), some need very precise and careful handling (window glass), while some are large and flexible (door board). These were the initial considerations as assembly time was estimated.

An important factor that affects assembly time in one of the principal geometrical design feature is its symmetry. According to Boothroyd *et al.* (2010), the symmetry factor contributes much to the time required to grasp and orient a part. Assembly usually involves two parts – the part to insert, and the part or assembly to be inserted, also known as receptacle. In discussing symmetry as an important factor, one has to consider the need for orienting the part to the correct position. Orientation may be defined as the alignment of part, e.g., screw relative to the corresponding receptacle. It involves aligning the part to the axis of insertion and rotating it about the axis before insertion may begin. In the cases presented, the factor has been shown to be highly significant, hence fasteners became the primary focus on reduction of assembly time. For Vehicle Door 1, as many as eight fasteners (symmetrical screws) were eliminated, while for Vehicle Door 2, five fasteners were eliminated.

In agreement with Balasubramanian (2002), who discussed the development of a drug-delivery device, and also mentioned in Boothroyd *et al.* (2010), two other major factors in the current study that affect the time in manual assembly are the thickness and size of the part. The two cases presented involve a variety of fastener sizes. Time was reduced as some of these were able to be removed, especially some big ones. In bulk production, minor savings like this will greatly improve production efficiency. Even though the margin of assembly time difference between the old and new design is not much, simplifying the product by combining and eliminating parts is known to have great impact on reducing assembly time. From the case studies, the analysis has proven that these approaches are feasible and may improve the assembly processes. The quantity of fasteners may be considered to be reduced.

6. CONCLUSION

The study showed that, by applying DFMA, further improvement may be made to vehicle door designs. Fundamentally, areas that permit further improvement are parts that are symmetrical and small, such as fasteners. A calculated, increments of 22.2 and 15.4 % efficiency may be achieved if the new designs are adopted the two vehicle doors. DFMA has been shown to have another area for design improvement towards concurrent engineering, particularly in automotive industry, for a wide range of transportation requirements in many fields.

ACKNOWLEDGEMENT

The authors would like to acknowledge Universiti Teknikal Malaysia Melaka (UTeM) for the facilities and resources used, as well as all those involved either directly or indirectly in this work.

REFERENCES

Ahmad, M.N.B., Ariff, H.A., Maidin, N.A., Rahman, M.H.A., Wahid, M.K. & Osman, M.H. (2018). Reducing product cost by implementing DFMA methodology – Lucas Hill: A Case Study. *ESTEEM Acad. J.*, **14**: 12-23.

Annamalai, K., Naiju, C.D., Karthik S. & Mohan Prashanth, M. (2013). Early cost estimate of product during design stage using design for manufacturing and assembly (DFMA) principles. *Adv. Mater. Res.*, **622-623**:540-544.

Ardayfio, D.D., Paganini, L.M., Swanson, R.C. & Wioskowski, J. (1998). *SAE Technical Paper 980198: Applications of DFMA in Automotive Electrical and Electronic Systems*. SAE International, US.

Balasubramanian, A, (2002). *Development of an Electronically-Controlled, Multidose, Nasal, Drug-Delivery Device*, MSc Thesis, University of Kentucky.

Barbosa, G.F. & Carvalho, J. (2013). Design for Manufacturing and Assembly methodology applied to aircrafts design and manufacturing. *11th IFAC Workshop on Intell. Manuf. Sys.*, São Paulo, Brazil, pp. 116-121.

Bogue, R. (2012). Design for manufacture and assembly: Background, capabilities and applications. *Assembly Autom.*, **32**:112–118.

Boothroyd, G. (1994). Product design for manufacture and assembly. *Comput. Aided Design*, **26**: 505-520.

Boothroyd, G., Dewhurst, P. & Knight, W.A. (2010). *Product Design for Manufacture and Assembly. 3rd Ed.*, CRC Press, Florida, US.

Da Silva, C.E.S., Salgado E.G., Mello, C.H.P., da Silva Oliveira, E. & Leal, F. (2013). Integration of computer simulation in design for manufacturing and assembly. *Int. J. of Prod. Res.*, **52**: 2851-2866.

Gao S., Jin R. & Lu W. (2020). Design for manufacture and assembly in construction: a review, *Build. Res. Inform.*, **48**: 538-580.

Genta, G., Morello, L., Cavallino, F. & Filtri, L. (2014). *The Motor Car: Past, Present and Future*. Springer, Berlin, Germany.

Harik, R.F. & Sahmrani, N. (2010). DFMA+, A Quantitative DFMA Methodology. *Comput. Aided Design & Appl.*, **7**: 701-709.

Herrera, A. (1997). Design for manufacturing and assembly application on the design of the AH64D helicopter. *Proc. 12th Int. Forum DFMA*, Newport, Rhode Island., US.

Kim, M.K., McGovern, S., Belsky, M., Middleton, C. & Brilakis, I. (2016). A suitability analysis of precast components for standardized bridge construction in the United Kingdom. *Procedia Eng.*, **164**: 188-195.

Kirkland, C. (1988). Meet two architects of design-integrated manufacturing, *Plastics World*, December 1988: 46-50.

Kuo, T.C., Huang, S.H. & Zhang, H.C. (2001). Design for manufacture and design for 'X': concepts, applications, and perspectives. *Comp. & Ind. Eng.*, **41:** 241-260.

Military-Today (2021). *Technicals: Light Utility Vehicle*. Available online at: http://www.military-today.com/trucks/technicals.htm. (Last access date: 6 September 2021).

Petrány, M. (2014). *The Ten Best Civilian-to-Military Conversions*. Available online at: https://jalopnik.com/the-ten-best-civilian-to-military-conversions-1564653623. (Last access date: 1 September 2021).

Suresh, P., Ramabalan S. & Natarajan, U. (2015). Integration of DFE and DFMA for the sustainable development of an automotive component. *Int. J. Sust. Eng*. **9**(2): 117-108

Tasalloti, H., Eskelinen, H., Kah P. & Martikainen, J. (2016). An integrated DFMA–PDM model for the design and analysis of challenging similar and dissimilar welds. *Mater. Des.*, **89**: 421-431.

Whitney, D.E. (1993). Nippondenso Co. Ltd: A case study of strategic product design. *Res. Eng. Des.*, **5**: 1 – 20.

Yuan, Z., Sun C. & Wang, Y. (2018). Design for manufacture and assembly-oriented parametric design of prefabricated buildings. *Automat. Constr.*, **88**: 13-22.

A STUDY ON HYBRID NANOFLUIDS EXPOSED TO RADIATION AND HEAT

Nurfathin Zahrolayali[1], Yusliandy Yusof[2] & Mohd Rosdzimin Abdul Rahman[1*]

[1]Department of Mechanical Engineering, Faculty of Engineering, National Defence University of Malaysia (UPNM), Malaysia
[2]Kolej Kemahiran Tinggi MARA, Malaysia

[*]Email: rosdzimin@upnm.edu.my

ABSTRACT

This study aims to investigate the effects of radiation and heat generation on hybrid nanofluids. A 2D axisymmetric tube was used as a numerical domain. The inlet velocity was assumed to be uniform at the respective Reynolds number, and the outlet velocity was assumed as a fully-developed flow. A non-slip wall condition with constant heat flux was assigned at the tube's wall. The Hamilton-Crosser (HC) and Koo-Kleinstreuer-Li (KKL) models were utilised to calculate the nanofluid's properties. The results indicate that the KKL model presented relatively improved results as compared to the HC model. Moreover, the heat transfer coefficient increased correspondingly with the increase in the nanoparticle's concentration in the hybrid nanofluid alongside the Reynolds number. The investigation revealed an increment of 27.74% between the nanofluid and hybrid nanofluid samples. In the presence of radiation, the entropy generation decreased by 25.84%. It can be concluded that radiation strongly influences the thermal behaviour of hybrid nanofluids.

Keywords: *Hybrid nanofluid; heat generation; heat transfer; radiation; numerical work.*

1. INTRODUCTION

Conventional coolants, such as water, ethylene glycol and oil, have poor thermal conductivity. Furthermore, the heat transfer capacity of these fluids is poor due to their low thermal conductivity, which limits the associated heat processes. A new breed of coolants known as nanofluids are increasingly being used, as it is a promising coolant that helps to improve the thermal performance for heat exchange processes (Arshad & Ali, 2017; Azmi *et al.*, 2017). Previous researchers have conducted studies on nanofluids to improve the understanding of the behaviour associated with nanofluids, as the heat transfer mechanism enhancement will benefit various industrial applications. The findings of this work is hoped to help to achieve the desired working temperatures for devices in various applications, including in the transportation and electronics industries (Sofiah *et al.*, 2021).

Several studies have found that nanofluids exhibit the desired characteristics and behaviour, such as improved heat transfer as a function of Reynolds number and nanoparticle concentration (Karimipour *et al.*, 2017). For example, Abbas *et al.* (2016) assessed silver (Ag) and copper (Cu) nanoparticles, Raei *et al.* (2016) investigated the pressure drop characteristics of gamma-alumina (γ-Al_2O_3) / water, Ho *et al.* (2016) studied the effect of temperature-dependent characteristics of alumina (Al_2O_3) / water nanofluid in a circular tube, and Zhao *et al*. (2016) investigated the effect of using a flat tube. In addition, Sheikholeslami *et al*. (2016, 2017) studied the thermal radiation effect on Al_2O_3 / water nanofluids free

magnetohydrodynamic (MHD) convection, and observed that the heat transfer increase was directly related to viscous dispersion and radiation parameters. Pandey & Kumar (2017) used Cu / water nanofluids to study the effect of thermal radiation and viscous dissipation, and showed that velocity could enhance the parameters of the natural convection process. Dogonchi *et al.* (2019b) investigated the flow of copper (II) oxide (CuO) / water nanofluids for thermal radiation and porous medium properties, and found that nanoparticles in platelet form depicted higher rate of heat transfer than other types of nanoparticles.

Previous studies have used several types of hybrid nanofluids and their performance in comparison with that of nanofluids has been proven. In Afrand *et al*. (2016), hybrid nanofluid was introduced by adding small amounts of different nanoparticles into the main nanofluid to significantly improve its thermal properties. Devi & Devi (2016) performed statistical investigations on hybrid nanofluids of Al_2O_3-Cu / water by studying the effects of the Lorenz force on a Newtonian heated 3D stretched layer. They found that hybrid nanofluids have high efficiency and thermal conductivity, enhanced heat transfer, as well as strong aspect ratios. The thermal behaviour of hybrid nanofluids using multiphase-mixed and multiphase-Eulerian models were discussed by Rahman *et al.* (2017). Minea (2017) found that the hybrid nanoparticle's suspension could increase the thermal transfer performance of pure water. In terms of radiation effects, Hayat & Nadeem (2017) used thermal radiation, heat generation, and chemical reactions in Ag-CuO / water hybrid nanofluids. The authors concluded that when radiation increases, it can increase temperature and radiative heat flow. Maskeen *et al.* (2019) tested the effect of Al_2O_3-Cu / water hybrid nanofluids on magnetic external fields, mixed convection, heat absorption, as well as dissipation of energy and light. They observed the effects of the related parameters and discovered that Nusselt number increased by raising the radiation and convection parameters, whereas when the curvature parameter and Eckert number increased, it had an opposite effect. Dogonchi *et al.* (2019a) researched the impact of iron (II, III) oxide (Fe_3O_4) / water nanofluid parameters and found that the average Nusselt number increased with the rise in Rayleigh number, radiation parameter and nanoparticle's volume fraction. Abbasian *et al.* (2019) investigated the effects of fluid flow and heat transfer of the thermal radiation of cobalt (II,III) oxide (CO_3O_4) - diamond / ethylene glycol hybrid nanofluids in a square enclosure, and found that the influence of the thermal radiation was not significant at high Rayleigh numbers.

The present study is aimed at improving the understanding of the effects of radiation and constant heat flux on the heat transfer and flow characteristics of Al_2O_3-Cu / water hybrid nanofluids. This study also investigates the effectiveness of the Hamilton-Crosser (HC) and Koo-Kleinstreuer-Li (KKL) models to calculate the thermal properties of hybrid nanofluids. The findings from the present study will help to enhance the understanding of the characteristics of hybrid nanofluids in the presence of radiation and heat fluxes.

2. METHODOLOGY

2.1 Geometry and Boundary Conditions

Figure 1 shows the numerical domain of a 2D axisymmetric aluminium tube with length of 1,000 mm, and diameter of 10 mm. It is similar to the geometry used by Suresh *et al.* (2012), whereby the authors utilised a heat flux constant of $\dot{q} = 9{,}549.29\ W/m^2$. At the inlet, a uniform axial velocity was given based on Reynolds number. Table 1 shows the characteristics of the base fluid and nanoparticles.

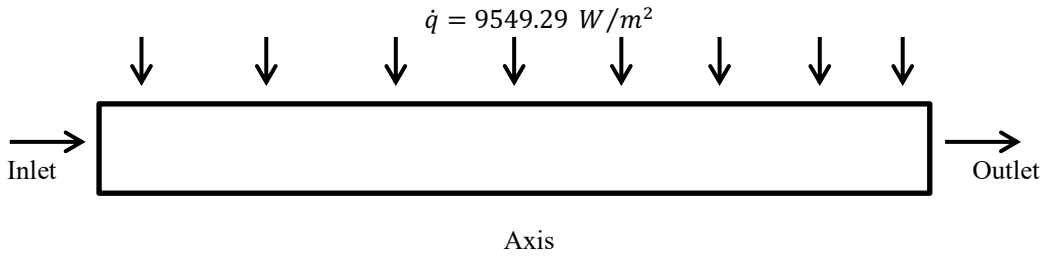

Figure 1: Numerical domain.

Table 1: Physical properties of water and nanoparticles (Sheikholeslami *et al.*, 2013).

	Density (ρ) (kg/m^3)	Specific heat capacity(C_p) (J/kgK)	Thermal conductivity (k) (W/mK)	Particle diameter (d_p) (nm)	Viscosity (μ) ($mPa\ s$)	Volume expansion coefficient ($\beta \times 10^5$) (K^{-1})
Pure water	997.1	4179	0.613	-	0.000855	21
Al_2O_3	3970	765	25	47	-	0.85
Cu	8933	385	401	15	-	1.67

2.2 Nanofluid and Hybrid Nanofluid Thermal Properties

The HC and KKL models are continuous phase models that are widely used in nanofluid simulation research works.

2.2.1 Hamilton-Crosser (HC) Model

The physical and thermal properties referred to are as follows (Dogonchi *et al.*, 2019a):

$$\rho_{nf} = \rho_f(1-\emptyset) + \rho_s\emptyset \tag{1}$$

$$\rho_{hnf} = \rho_f\left(1-\emptyset_{Cu}-\emptyset_{Al_2O_3}\right) + \emptyset_{Cu}\rho_{Cu} + \emptyset_{Al_2O_3}\rho_{Al_2O_3} \tag{2}$$

$$\left(\rho c_p\right)_{nf} = \left(\rho c_p\right)_f(1-\emptyset) + \left(\rho c_p\right)_s\emptyset \tag{3}$$

$$\left(\rho c_p\right)_{hnf} = \left(\rho c_p\right)_f\left(1-\emptyset_{Cu}-\emptyset_{Al_2O_3}\right) + \emptyset_{Cu}Cp_{Cu} + \emptyset_{Al_2O_3}Cp_{Al_2O_3} \tag{4}$$

$$\mu_{nf} = \frac{\mu_f}{(1-\emptyset)^{2.5}} \tag{5}$$

$$\mu_{hnf} = \frac{\mu_f}{\left(1-\emptyset_{Cu}-\emptyset_{Al_2O_3}\right)^{2.5}} \tag{6}$$

$$k_{nf} = k_f\left[\frac{k_s+(m+1)k_f-(m+1)\emptyset\left(k_f-k_s\right)}{k_s+(m+1)k_f+\emptyset\left(k_f-k_s\right)}\right] \tag{7}$$

$$k_{hnf} = k_f\left[\frac{\frac{\emptyset_{Cu}k_{Cu}+\emptyset_{Al_2O_3}k_{Al_2O_3}}{\emptyset}+(m+1)k_f-(m+1)\emptyset\left(k_f-\frac{\emptyset_{Cu}k_{Cu}+\emptyset_{Al_2O_3}k_{Al_2O_3}}{\emptyset}\right)}{\frac{\emptyset_{Cu}k_{Cu}+\emptyset_{Al_2O_3}k_{Al_2O_3}}{\emptyset}+(m+1)k_f+\emptyset\left(k_f-\frac{\emptyset_{Cu}k_{Cu}+\emptyset_{Al_2O_3}k_{Al_2O_3}}{\emptyset}\right)}\right] \tag{8}$$

where *m* is the shape factor for the model used in Equation 8, with the numerical values for various shapes displayed in Table 2.

Table 2: The shape factor values for various shapes of nanoparticles (Sobamowo, 2018; Benkhedda *et al.*, 2020).

No	Name	Shape Factor (*m*)
1	Sphere	3.0
2	Platelet	5.7
3	Cylinder	4.8
4	Lamina	16.2
5	Brick	3.7
6	Blades	8.6

2.2.2 Koo-Kleinstreuer-Li (KKL) Model

Brownian movement greatly influences active thermal conductivity. The KKL model suggests that active thermal conductivity consists of the typical static components in the sample, and in a section of the Brownian motion (Yang, 2008). The model of thermal conductivity has two components that are considered as the consequences of particle volume fractions, the particle's size and temperature dependency:

$$k_{eff} = k_{static} + k_{Brownian} \tag{9}$$

$$\frac{k_{static}}{k_f} = 1 + \frac{3\left(\frac{k_p}{k_f}-1\right)\emptyset}{\left(\frac{k_p}{k_f}+2\right)-\left(\frac{k_p}{k_f}-1\right)\emptyset} \tag{10}$$

where k_{static} is the standard Maxwell-based static thermal conductivity. In addition to the temperature influence in the system, the model merges the interaction between the nanoparticles by adding two experimental functions (β and f), which culminates in:

$$k_{Brownian} = 5 \times 10^4 \beta \emptyset \rho_f c_{p,f} \sqrt{\frac{1.38\text{x}10^{-23}T}{\rho_p d_p}} f(T, \emptyset) \tag{11}$$

The task should be different for different liquids and different nanoparticles. The existing research includes only water-based nanofluids. This function follows the format used for Al_2O_3 / water nanofluids:

$$g'^{(T,\emptyset,d_p)} = \left(a_1 + a_2 ln(d_p) + a_3 ln(\emptyset) + a_4 ln(\emptyset) ln(d_p) + a_5 ln(d_p)^2\right) \ln(T) + \left(a_6 + a_7 \ln(d_p) + a_8 \ln(\emptyset) + a_9 \ln(\emptyset) \ln(d_p) + a_{10} ln(d_p)^2\right) \tag{12}$$

The coefficients a_i (i = 0, 1,2, ... 10) are based on the shape of the nanoparticles, with the coefficients for Al_2O_3 / water nanofluids listed in Table 3. Eventually, the correlation of the KKL is as follows:

$$k_{Brownian} = 5 \times 10^4 \beta \emptyset \rho_f c_{p,f} \sqrt{\frac{1.38\text{x}10^{-23}T}{\rho_p d_p}} g'(T, \emptyset, d_p) \tag{13}$$

Table 3: The coefficient values of Al_2O_3 / water nanofluids (Sheikholeslami *et al.*, 2013).

Coefficient	Al_2O_3 / Water
a_1	52.813488759
a_2	6.115637295
a_3	0.6955745084
a_4	4.17455552786E−02
a_5	0.176919300241
a_6	−298.19819084
a_7	−34.532716906
a_8	-3.9225289283
a_9	−0.2354329626
a_{10}	−0.999063481

Koo & Kleinstreuer (2005) further investigated the laminar nanofluid's flow in micro-heat sinks using an active nanofluid thermal conductivity model. The proposed correlation for the active viscosity in the suspension due to micro-mixing is as follows:

$$\mu_{eff} = \mu_{static} + \mu_{Brownian} = \mu_{static} + \frac{k_{Brownian}}{k_f} \times \frac{\mu_f}{Pr_f} \tag{14}$$

where $\mu_{static} = \frac{\mu_f}{(1-\emptyset)^{2.5}}$ is the nanofluid's viscosity, as originally suggested by Brinkman (1952).

2.3 Numerical Procedure

ANSYS Fluent 2020 R2, was used to solve a set of partial nonlinear differential equations. The convergence was set at 10^{-6}, with an optimised mesh size that was set to reduce the computing cost. Five different grid refinement levels were used. In order to lower the computational cost, mesh size optimisation was implemented. Figure 2 shows that the grid size of 1,000 × 10 fits with the grid sizes of 1,000 × 50, 3,000 × 10 and 3,000 × 30 for the velocity magnitude of water at the pipe outlet. Thus, this grid size was used for all the simulation cases in order to lower the computational cost.

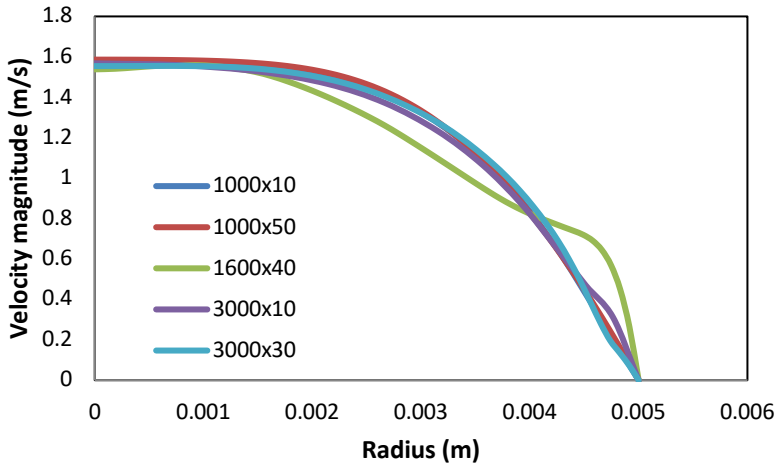

Figure 2: Mesh independent study.

2.3.1 Validation of the Numerical Work

Model validation for the HC and KKL models was conducted by comparing the average Nusselt number for the Reynold's numbers *Re* = 800 to *Re* = 2,300 of the current statistical study, which was in agreement with the experimental work by Suresh *et al.* (2012). The average Nusselt number was acquired from Equations 15 and 16, while the local Nusselt number was from Equations 17 to 22.

$$Nu_{ave} = \frac{hD}{k} \tag{15}$$

$$h_{ave} = \frac{\dot{q}}{T_{out} - T_{in}} \tag{16}$$

$$Nu = \frac{hD}{k_{nf}} \tag{17}$$

$$h = \frac{\dot{m} c_{p_{nf}} (T_{b,out} - T_{b,in})}{A_{surface}\, \Delta T} \tag{18}$$

$$\dot{m} = \rho_{nf} A V = \rho_{nf} \left(\frac{\pi D^2}{4}\right) V \tag{19}$$

$$A_{surface} = \pi D L \tag{20}$$

$$\Delta T = T_S - T_b \tag{21}$$

$$T_b = \frac{T_{in} + T_{out}}{2} \tag{22}$$

2.3.2 Effect of Particle Volume Concentration

The impact of the concentration of the nanoparticles on the heat transfer efficiency at different Reynolds numbers was observed. The density of the Al_2O_3-Cu nanoparticles in water ranges between 0.04 to 4% when maintaining the ratio of 70:30 between the Al_2O3 and Cu nanoparticles respectively. The characteristics of the flow and heat transfer are expressed in terms of the Nusselt number at varying percentages of nanoparticles and shapes. The dimensionless friction factor for the pressure drop determination, as shown in Equation 23, was then compared with the Hagen-Poiseuille equation in Equation 24 for the theoretical values. Equation 25 was used to calculate the entropy generation rate per unit tube length (Bejan, 2012).

$$f = \frac{\Delta P}{0.5 \rho u^2} . \frac{D}{L} \tag{23}$$

$$f = \frac{64}{Re} \tag{24}$$

$$S'_{gen} = \frac{q'^2}{\pi k T^2 Nu} + \frac{32 \dot{m}^3 f}{\pi^2 \rho^2 T D^5} \tag{25}$$

3. RESULTS AND DISCUSSION

3.1 Validation

Figure 3 shows the simulation validation of the study with the experimental data by Suresh *et al.* (2012). The result depicts an agreement between the simulation and experimental works.

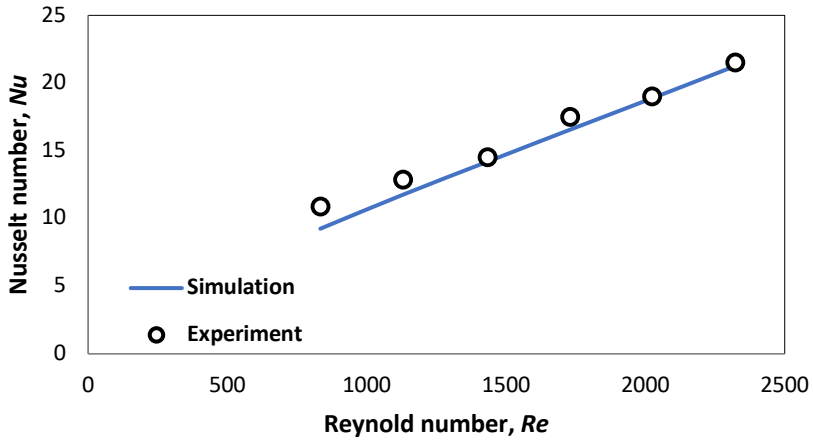

Figure 3: Validation of simulation with experimental results.

Figure 4 shows the comparison of Nusselt numbers between the experimental data from Suresh *et al.* (2012), and the numerical data from the HC and KKL models for 0.1% Al_2O_3-Cu / water hybrid nanofluid. It illustrates that both models predicted the pattern well based on the experimental data. The KKL model had significant influence on thermal efficiency, while the HC model incorporated the shape factors. Thus, the KKL model has was chosen for the present study.

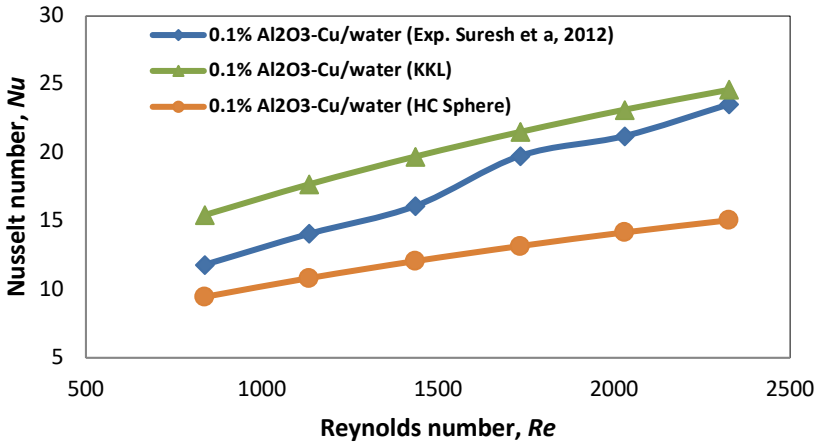

Figure 4: Comparison of Nusselt number for the numerical works with the experimental data for 0.1% Al_2O_3 –Cu / water hybrid nanofluids.

Figure 5 shows the effect of the concentration of the hybrid nanoparticles across different Reynolds numbers. It can be seen that there is an increase in the particle concentration when the Nusselt number increases. The increment in the Nusselt number is related to the thermal conductivity of the hybrid nanofluids. It is seen that an increase in volume concentration will increase the density and viscosity of the hybrid nanofluids.

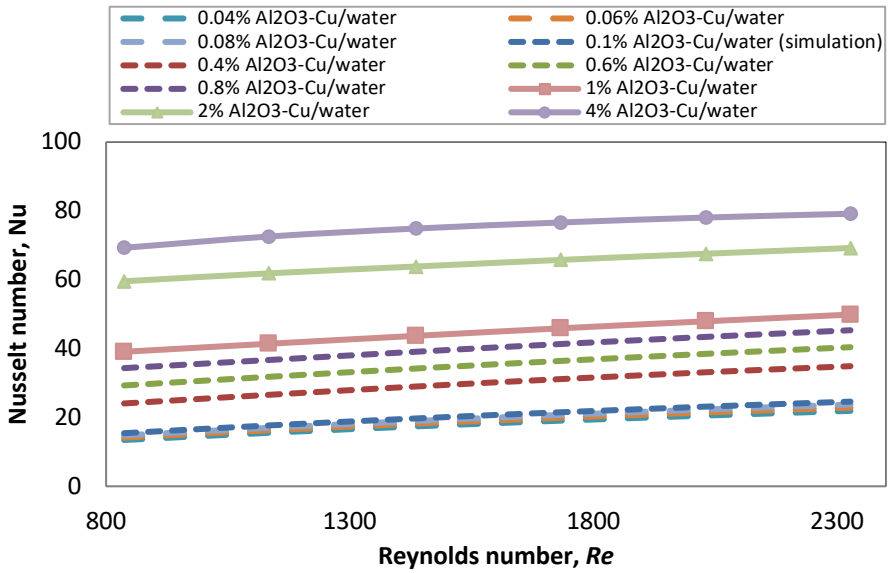

Figure 5: Effect of the Al_2O_3-Cu nanoparticle concentration at various Reynolds numbers.

Figure 6 shows the effect of Reynolds number on friction factor using the KKL model. Friction factor represents the pressure drop in a pipe. It can be seen that increase in Reynolds number resulted in decrease in friction factor. Similar trends were found experimentally by Suresh *et al.* (2012). Decrease in friction factor at high Reynolds numbers is due to decrease in laminar boundary layer thicknesses in the pipe. Increase in the nanoparticle's volume concentration could increase the friction factor. Higher friction factor at higher nanoparticles volume concentration most likely took place due to increase in viscosity and density of the nanofluids.

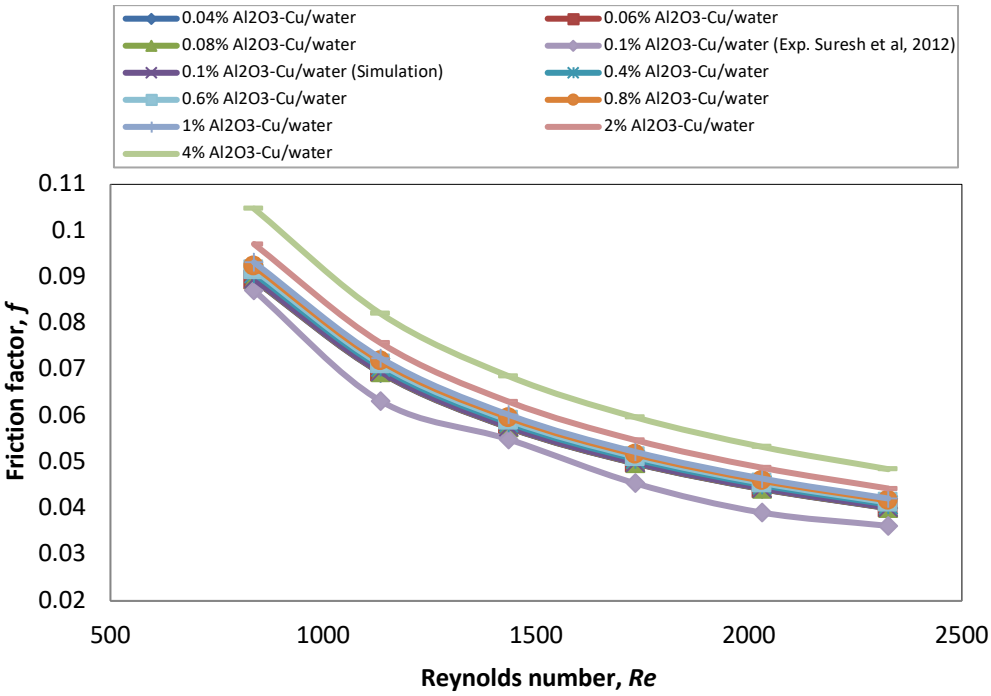

Figure 6: Friction factor at different concentrations using the KKL model.

Figure 7 shows the effect of hybrid nanoparticle concentration with radiation at various Reynolds numbers. It can be seen that as the particle concentration increased, Nusselt number increased as well. The increase in Nusselt number was due to the rise in the radiation hybrid nanofluid's thermal conductivity. The increase in density and viscosity of the hybrid nanofluids increased the particle's volume concentration. However, the increase in the density and viscosity decreased the velocity for the same Reynolds number, and increased the coefficient of heat transfer.

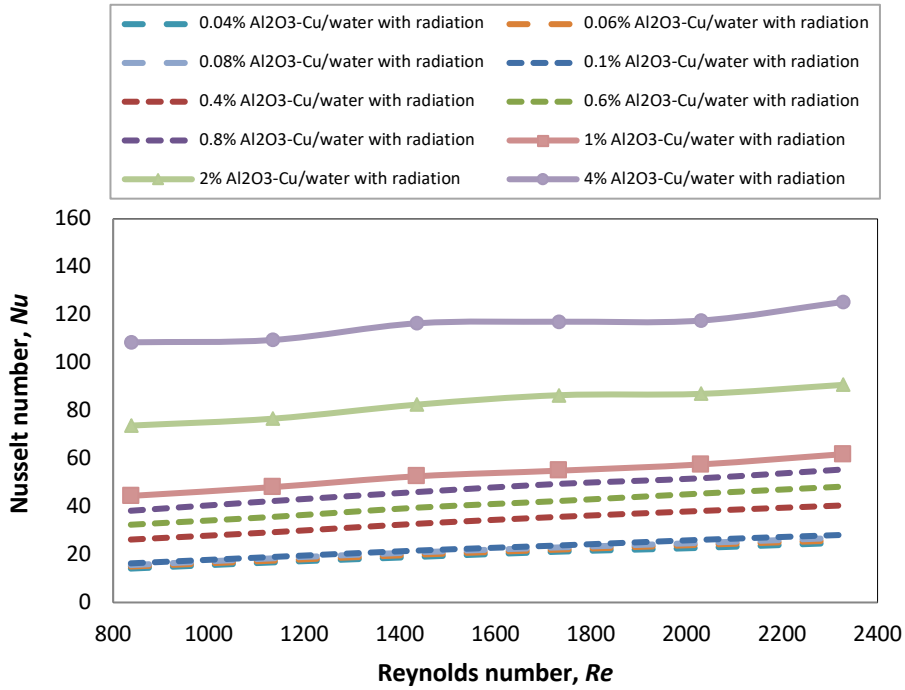

Figure 7: Effect of the Al_2O_3-Cu nanoparticle concentration with radiation at various Reynolds numbers.

Figure 8 shows the Al_2O_3-Cu / water hybrid nanofluids with the radiation effect of the Reynolds number for the friction factor. The increase in the Reynolds number was shown to decrease the friction factor. The reduction in the friction factor at the high Reynolds number was due to the reduced thickness of the pipe's laminar boundaries. The increased volume concentration of the nanoparticles will increase the friction factor. The higher friction factor is most likely due to an increase in the nanofluid's viscosity and density at high volume concentrations of nanoparticles.

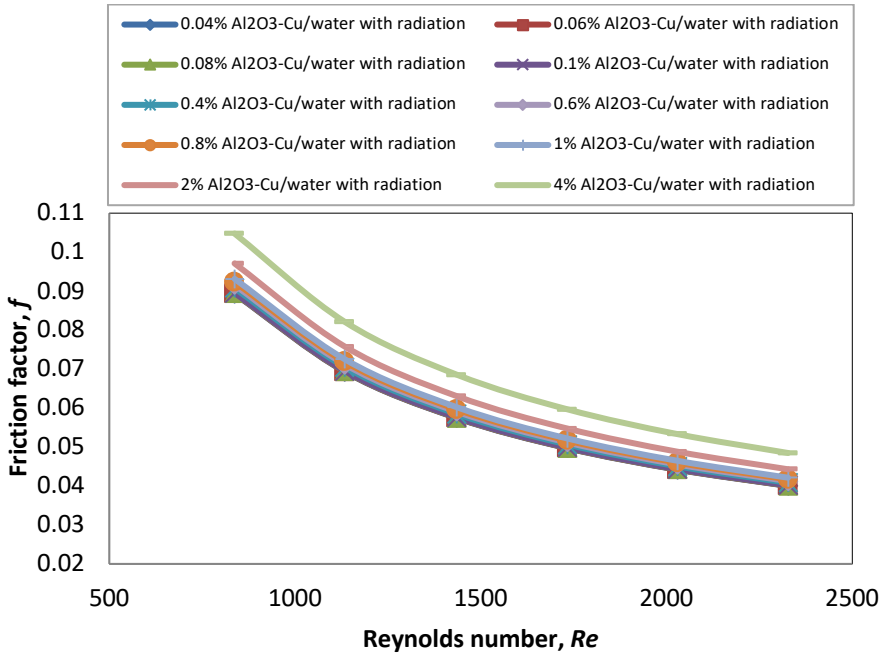

Figure 8: Friction factor at different concentrations using the KKL model.

Figure 9 shows the effect of Reynolds number on Nusselt number for the Al_2O_3-Cu / water hybrid nanofluids. It illustrates that the hybrid nanofluid with radiation depicted thermal behavioural characteristics similar to that of the hybrid nanofluid. It is also shown that for increasing Reynolds numbers across all the samples, the average coefficient of heat transfer also increased. In addition, for the average hybrid nanofluid with radiation, the coefficient of heat transfer was more similar to the hybrid nanofluid than that of the experimental hybrid nanofluid results. This was due to the physical properties of the hybrid nanofluids and Al_2O_3 nanoparticles being much more dominant in the radiation of the Al_2O_3-Cu / water hybrid nanofluid. As compared to the hybrid nanofluid, the density and viscosity were higher, but lower than the experimental data in Suresh *et al.* (2012). However, at the same Reynolds number, the velocity for the hybrid nanofluid with radiation was lower than that of the hybrid nanofluid. In addition, the hybrid nanofluid's thermal characteristics were affected by thermal conductivity. The Cu nanoparticles were more thermally conductive than the Al_2O_3 nanoparticles using a ratio of 70:30 for the Al_2O_3 and Cu nanoparticles in the hybrid nanofluid. The hybrid nanofluid with radiation was rather similar to the hybrid nanofluid in terms of characteristics.

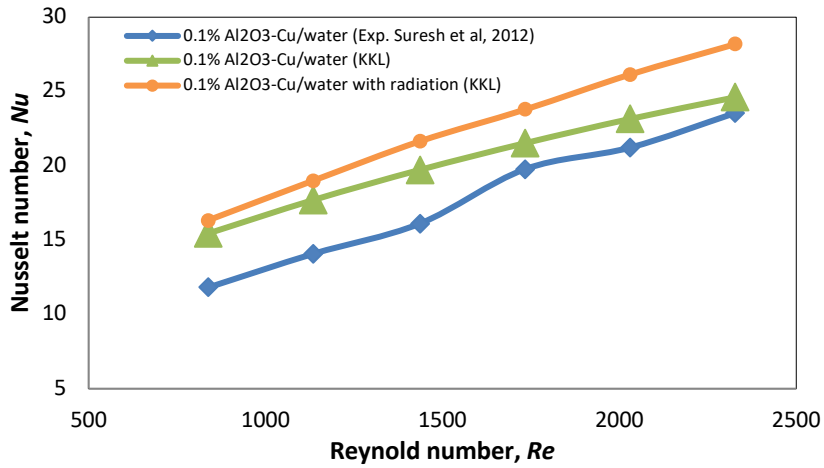

Figure 9: Effect of Reynolds number on Nusselt number.

Figure 10 shows the effect of Reynolds number on friction factor for the Al_2O_3-Cu / water hybrid nanofluids. Increase in Reynolds number is shown to decrease the friction factor. Reduction of friction factor at high Reynolds number is due to the reduced thickness of the boundary layer. In addition, the differences of friction factor between the hybrid nanofluid with radiation and hybrid nanofluid are higher at low Reynolds numbers. According to the flows at the end of the laminar fluid flow and entering the transition fluid flow, there is a slight variation in friction factor at high Reynolds numbers in this study.

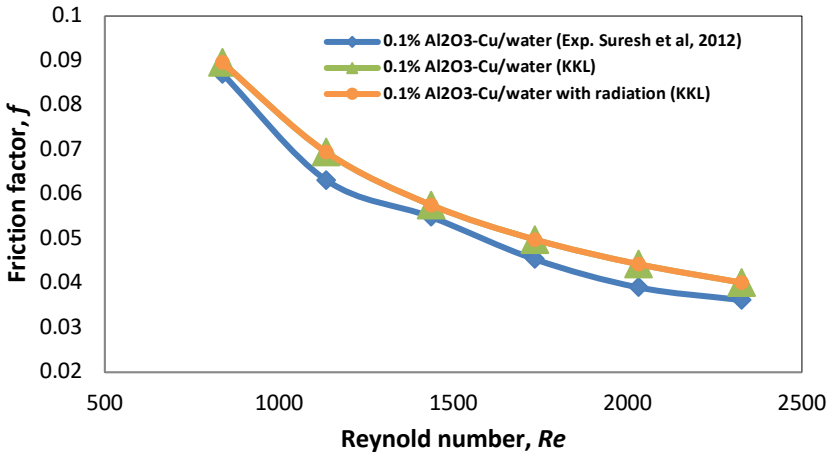

Figure 10: Effect of friction factor on Reynolds number.

Figure 11 shows the effect of Reynolds number on the entropy generation of the Al_2O_3-Cu / hybrid nanofluids. It was found that Reynolds number directly affected the entropy generation. Increase in Reynolds number decreases the contribution of the entropy generation amount due to the fluid's turbulence and heat transfer in the boundary layers. The increase in the Reynolds number disturbed the fluid and culminated in instability that occurred in the flow of the fluid. As the Reynolds number decreased, the entropy generation increased. It is seen that the entropy generation of the hybrid nanofluid increased by about 27.74% as compared to the nanofluid. Moreover, by introducing radiation, the entropy generation decreased by about 25.84%.

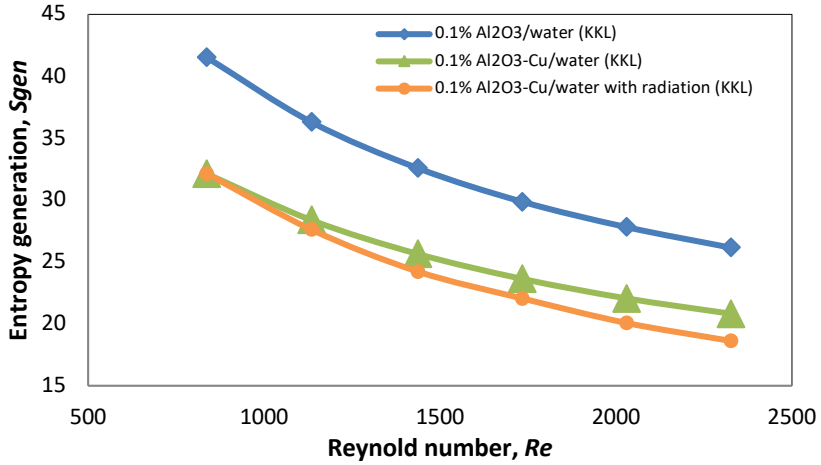

Figure 11: Effect of the Reynolds number on entropy generation.

4. CONCLUSION

An internal forced convective heat transfer with radiation of Al_2O_3-Cu / water hybrid nanofluids was numerically investigated to enhance the heat transfer performance in heat exchange processes. The results showed that numerical data from the HC and KKL models were coherent with the experimental results. The heat transfer coefficient was significantly enhanced as there was a radiation effect. The thermal behaviour of the hybrid nanofluids was strongly influenced by the percentage of hybrid nanoparticles in the base fluid. Therefore, it is believed that the friction factor increased with an increase in the hybrid nanoparticle's percentage. This study confirmed that hybrid nanofluids improved the heat transfer performance in the presence of radiation and heat generation of hybrid nanofluids.

ACKNOWLEDGMENT

The authors would like to acknowledge the National Defense University of Malaysia (UPNM) for their financial support under the grant number UPNM/2021/GPPP/TK/3.

Nomenclature

Ag	Silver
Al_2O_3	Alumina
Cu	Copper
CuO	Copper Oxide
Fe_3O_4	Iron oxide
SiO_2	Silicon Dioxide
TiO_2	Titanium Dioxide
A	Area (m^2)
$A_{surface}$	Surface area
C_p	Specific heat capacity ($J/kg/K$)
D	Diameter (m)
L	Length (m)
P	Pressure (Pa)
P_y	Fluid yield stress
T	Temperature (K)
V	Velocity (m^2/s)
a_n	Coefficient values
d	Particle diameter (nm)
e_{ij}	Deformation rate
f	Friction factor
h	Heat transfer coefficient (W/m^2K)
k	Thermal conductivity (W/mK)
k_b	Boltzmann constant
m	Shape factor
$\dot{m}$	Mass flow rate (kg/s)
$\dot{q}$	Heat flux (W/m^2)
vol%	Volume percentage
Nu	Nusselt number

Pr	Prandtl number
Re	Reynolds number

Greek letters

Γ	Gamma
β	Volume Expansion Coefficient (K^{-1})
ρ	Density (kg/m^3)
μ	Viscosity (mPa s)
τ	Shear stress (N/m^2)
τ_o	Casson yield stress
$\emptyset$	Volume concentration
Ψ	Sphericity
$\dot{\sigma}$	Shear rate
π	Deformation element
π_C	Product critical value

Subscript

ave	average
Brownian	Brownian motion
b	bulk
eff	Effective
f	Fluid
hnf	Hybrid Nanofluid
in	Pipe inlet
L	Local
nf	Nanofluid
out	Pipe outlet
p	Particle
static	Static
s	Solid
w	Wall

REFERENCES

Abbasian Arani, A.A., Monfaredi, F., Aghaei, A., Afrand, M., Chamkha, A.J. & Emami, H. (2019). Thermal radiation effect on the flow field and heat transfer of Co3O4-diamond/EG hybrid nanofluid using experimental data: A numerical study. *Eur. Phys. J. Plus*, **134**:. Art. Num. 13.

Abbas, Z., Naveed, M. & Sajid, M. (2016). Hydromagnetic slip flow of nanofluid over a curved stretching surface with heat generation and thermal radiation. *J. Mol. Liq.*, **215**: 756–762.

Afrand, M., Toghraie, D. & Ruhani, B. (2016). Effects of temperature and nanoparticles concentration on rheological behavior of Fe3O4-Ag/EG hybrid nanofluid: An experimental study. *Exp. Therm. Fluid Sci.*, **77**: 38–44.

Arshad, W. & Ali, H.M. (2017). Experimental investigation of heat transfer and pressure drop in a straight minichannel heat sink using TiO2 nanofluid. *Int. J. Heat Mass Transf.*, **110:** 248–256.

Azmi, W.H., Usri, N.A., Mamat, R., Sharma, K.V. & Noor, M.M. (2017). Force convection

heat transfer of Al2O3 nanofluids for different based ratio of water: Ethylene glycol mixture. *Appl. Therm. Eng.*, **112**: 707–719.

Bejan, A. (2012). Entropy generation minimization : The new thermodynamics of finitesize devices and finitetime processes. *J. Appl. Phys.*, **79**: 1191.

Brinkman, H.C., (1952). The viscosity of concentrated suspensions and solutions. *J. Chem. Phys*., **20**:571–581.

Devi, S. S. U. & Devi, S. P. A. (2016). Numerical investigation of three-dimensional hybrid Cu-Al2O3/water nanofluid flow over a stretching sheet with effecting Lorentz force subject to Newtonian heating. *Can. J. Phys.*, **94**: 490–496.

Dogonchi, A.S., Waqas, M., Seyyedi, S.M., Hashemi-Tilehnoee, M. & Ganji, D.D. (2019a). CVFEM analysis for Fe3O4–H2O nanofluid in an annulus subject to thermal radiation. *Int. J. Heat Mass Transf.*, **132**: 473–483.

Dogonchi, A.S., Waqas, M., Seyyedi, S.M., Hashemi-Tilehnoee, M. & Ganji, D. D. (2019b). Numerical simulation for thermal radiation and porous medium characteristics in flow of CuO-H2O nanofluid. *J. Braz. Soc. Mech. Sci. Eng.*, **41**: 1–13.

Hayat, T. & Nadeem, S. (2017). Heat transfer enhancement with Ag–CuO/water hybrid nanofluid. *Results Phys.*, **7**: 2317–2324.

Ho, C. J., Chang, C. Y., Cheng, C.Y., Cheng, S.J., Guo, Y. W., Hsu, S. T. & Yan, W.M. (2016). Laminar forced convection effectiveness of Al2O3-water nanofluid flow in a circular tube at various operation temperatures: Effects of temperature-dependent properties. *Int. J. Heat Mass Transf.*, **100**: 464–481.

Karimipour, A., D'Orazio, A. & Shadloo, M. S. (2017). The effects of different nano particles of Al2O3 and Ag on the MHD nano fluid flow and heat transfer in a microchannel including slip velocity and temperature jump. *Phys. E: Low-Dimens. Syst. Nanostr.*, **86**: 146–153.

Koo, J. & Kleinstreuer, C. (2005). Laminar nanofluid flow in microheat-sinks. *Int. J. Heat Mass Transf.*, **48**: 2652–2661.

Maskeen, M.M., Zeeshan, A., Mehmood, O.U. & Hassan, M. (2019). Heat transfer enhancement in hydromagnetic alumina–copper/water hybrid nanofluid flow over a stretching cylinder. *J. Therm. Anal. Calorim.*, **138**: 1127–1136.

Minea, A.A. (2017). Hybrid nanofluids based on Al2O3, TiO2 and SiO2: Numerical evaluation of different approaches. *Int. J. Heat Mass Transf.*, **104**: 852–860.

Pandey, A.K.,& Kumar, M. (2017). Natural convection and thermal radiation influence on nanofluid flow over a stretching cylinder in a porous medium with viscous dissipation. *AEJ - Alex. Eng. J.*, **56**: 55–62.

Raei, B., Shahraki, F. & Jamialahmadi, M. (2016). Experimental investigation on the heat transfer performance and pressure drop characteristics of γ-Al2O3/water nanofluid in a double tube counter flow heat exchanger. *Trans. Phenom. Nano Micro Scale*, **5**: 64–75.

Rahman, M.R.A., Leong, K.Y., Idris, A.C., Saad, M.R. & Anwar, M. (2017). Numerical analysis of the forced convective heat transfer on Al2O3–Cu/water hybrid nanofluid. *Heat Mass Transf.*, **53**: 1835–1842.

Sheikholeslami, M., Gorji-Bandpy, M. & Ganji, D. D. (2013). Numerical investigation of MHD effects on Al2O3-water nanofluid flow and heat transfer in a semi-annulus enclosure using LBM. *Energy*, **60**: 501–510.

Sheikholeslami, M., Hayat, T. & Alsaedi, A. (2016). MHD free convection of Al2O3-water nanofluid considering thermal radiation: A numerical study. *Int. J. Heat Mass Transf.*, **96**: 513–524.

Sheikholeslami, M., Ziabakhsh, Z. & Ganji, D.D. (2017). Transport of Magnetohydrodynamic nanofluid in a porous media. *Colloids Surf. A: Physicochem. Eng. Asp.*, **520**: 201–212.

Sofiah, A.G.N., Samykano, M., Pandey, A.K., Kadirgama, K., Sharma, K. & Saidur, R. (2021). Immense impact from small particles: Review on stability and thermophysical properties of nanofluids. *Sustain. Energy Technol. Assess.*, **48**: 101635.

Suresh, S., Venkitaraj, K.P., Selvakumar, P. & Chandrasekar, M. (2012). Effect of Al 2O 3-Cu/water hybrid nanofluid in heat transfer. *Exp. Therm. Fluid Sci.*, **38**: 54–60.

Yang, B (2008). thermal Conductivity Equations Based on Brownian Motion in Suspensions of Nanoparticles (Nanofluids). ASME *J. Heat Transfer*. **130**: 042408.

Zhao, N., Yang, J., Li, H., Zhang, Z. & Li, S. (2016). Numerical investigations of laminar heat transfer and flow performance of Al2O3-water nanofluids in a flat tube. *Int. J. Heat Mass Transf.*, **92**: 268–282.

THE THREAT OF PLANT TOXINS AND BIOTERRORISM: A REVIEW

Gian Marco Ludovici[1,2*], Daniela Arduini[1], Pasqualino Gaudio[1,2], Andrea Chierici[2,3], Guglielmo Manenti[4] & Andrea Malizia[4]

[1] International Master Courses in Protection against CBRNe Events, University of Rome Tor Vergata, Italy
[2]Department of Industrial Engineering, University of Rome Tor Vergata, Italy
[3]Department of Civil and Industrial Engineering, University of Pisa, Italy
[4]Department of Biomedicine and Prevention, University of Rome Tor Vergata, Italy

[*]Email: gianmarco.ludovici@alumni.uniroma2.eu

ABSTRACT

The intentional use of highly pathogenic microorganisms, such as bacteria, viruses or their toxins, to spread mass-scale diseases that destabilize populations (with motivations of religious or ideological belief, monetary implications, or political decisions) is defined as bioterrorism. Although the success of a bioterrorism attack is not very realistic due to technical constraints, it is not unlikely and the threat of such an attack is higher than ever before. It is now a fact that the capability to create panic has allured terrorists for the use of biological agents (BAs) to cause terror attacks. In the era of biotechnology and nanotechnology, accessibility in terms of price and availability has spread fast, with new sophisticated BAs often being produced and used. Moreover, there are some BAs that are becoming increasingly important, such as toxins produced by bacteria (e.g., Botulinum toxin, BTX), or Enterotoxyn type B, also known as Staphylococcal Enterotoxin B (SEB)) and extractions from plants. The most increasing records are with regards to the extraction / production of ricin, abrin, modeccin, viscumin and volkensin, which are the most lethal plant toxins known to humans, even in low amounts. Moreover, ricin was also developed as an aerosol biological warfare agent (BWA) by the US and its allies during World War II, but was never used. Nowadays, there are increasing records that show how easy it can be to extract plant toxins and transform them into biological weapon agents (BWAs), regardless of the scale of the group of individuals.

Keywords: *Biological warfare agent (BWAs)*; *plant toxins*; *biosecurity*; *biocrimes*; *bioterrorism.*

1. INTRODUCTION

The current concept of terrorism has as its main objective to threaten and terrorize large groups of humans, governments, armies or societies (Cenciarelli *et al.*, 2013; Barras & Greub, 2014). Concerning bioterrorism, it is assumed that this type terrorism involves the use of biological agents (BAs) by actors or groups, motivated by various reasons, such as political belief, religious convictions, etc., with the goal of achieving a specific aim (Christopher *et al.*, 1997; Mannik, 2009; Oliveira *et al.*, 2020). With regards to the latter topic, the debate has emerged in recent years regarding the transcendence of biological warfare, specifically with respect to public health, individual criminal acts, bioterrorism, wars and international laws directed towards the elimination of biological warfare agents (BWAs) (Gori & Tomar, 2020). At present, bioterrorism is one of the most intricate topics of discussion, posing unresolved problems and opening up new ethical challenges. Many scientists define acts of biological warfare as the absolute perversion of medical science (Atlas, 2002; Koch *et al.*, 2020; Oliveira *et al.*, 2020).

Besides being coherent and true in regards to the current political and scientific concerns, this affirmation of the transcendence of biological warfare and bioterrorism also has important historical significance. The reasoning behind the threat and menace to public health seems to be as ancient as humanity itself (Riedel, 2004). The historical study of biological warfare and bioterrorism is a matter that needs to be debated cautiously as it deals with a variety of factors that need to be controlled and examined in depth (Oliveira *et al.*, 2020). The lack of reliable scientific data on alleged bioterrorism attacks, particularly those that happened before the rise of modern microbiology and the conditions concerning any of the presumed attacks,

in other words the availability to documentation, is susceptible to a multitude of manipulative factors such as political, scientific, as well as historical distance between older stories of attacks and their potential misunderstandings when interpreted with today's current objectives and motivations (Riedel, 2004; Thavaselvam & Vijayaraghavan, 2010; Klietmann & Ruoff, 2011; Barras & Greub, 2014; Lee & Kim, 2021). Given such a multitude of factors implied, it is difficult to differentiate natural epidemic events from alleged biological attacks (Koch *et al.*, 2020).

1.1 Biological Warfare in History

In ancient history, one of the well-known attempts to use BAs was the one that happened during the 14th century medieval siege of Kaffa (Cenciarelli *et al.*, 2013; Oliveira *et al.*, 2020). In this event, the Tartars who attacked Kaffa spread dead and dying victims of the plague into the city in an attempt to further spread the disease (Christopher *et al.*, 1997; Wheelis, 2002). In another documented incident in Fort Pitt (USA), the British army deliberately spread smallpox among the native Indian population by presenting them with blankets and linens used by smallpox victims (Ranlet, 2000). There is historical evidence that shows attempts of spreading smallpox disease via infected British soldiers during the American Revolutionary War (1776-1781) and by contaminated clothing during the American Civil War (1861–1865) (Becker, 2004). The importance of BAs has become increasingly significant in the present century due to several wars and multiple threats spread. In spite of the 1972 Biological Weapons Convention, records have shown how accidental release and deliberate use have occurred, for example, of anthrax from a military testing facility in the former Soviet Union in 1979, along with the Iraqi army and its possession of BTX, anthrax and various aflatoxins (AFs) (e.g.. AFB and AFG) during the Gulf War (Black & Read, 2007; D'Amelio *et al.*, 2015). Other more recent examples have occurred in Dalles, Oregon ,US, where the Rajneeshees attempted to influence local elections by contaminating salad bars with *Salmonella typhimurium*, which is a bacteria that can cause food poisoning, and again in the US in 2001, where letters containing anthrax spores rekindled the fear of bioterrorism and biological warfare (Thavaselvam &Vijayaraghavan, 2010; D'Amelio *et al.*, 2015; Sharma *et al.*, 2016). All this makes it possible to see how research and development of these toxins and BAs is heavily widespread. The most important aspects linked to the use of BAs in a bioterrorism event are accessibility to the agents, the scientific experience for the management and large scale production of the latter together with accessibility in providing the correct equipment for its widespread diffusion (Kaufer *et al.*, 2020).

1.2 Biological Warfare Agents (BWAs)

BWAs are microorganisms, such as virus, bacteria, fungi, protozoa or toxins produced by the latter themselves, that give birth to diseases in humans, animals or plants, particularly when deliberately dispersed in an area (Jansen *et al.*, 2014; Janik *et al.*, 2019). These agents can cause large-scale mortality, disable large numbers of people in a short time and have serious adverse effects on human health. The use of BWAs can be hidden or obvious, and differ from conventional weapons due to several unique properties (Riedel, 2004; Sharma *et al.*, 2016). The effects of these agents are not instantaneous and require from a few hours to weeks before the symptoms appear in the affected population. Biological attacks only require a release of small amounts of viable agents (Ludovici *et al.*, 2015). For example, viruses are a small collection of genetic code, either DNA or RNA, surrounded by a protein coat. A virus cannot replicate alone. Viruses must infect cells and use components of the host cell to make copies of themselves. Often, they kill the host cell in the process, and cause damage to the host organism. Bacteria are mono-cellular prokaryotic organisms and possess a determined cell wall. Fungi are unicellular or multicellular organisms, eukaryotes and have no chlorophyll, unlike plants. Many fungal species are known to cause diseases in plants and humans (Cenciarelli *et al.*, 2013). Toxins are secondary metabolites produced by bacteria, fungi, algae, plants, fish and crustaceans (and also discovered in viruses), and are known to act in very low concentrations affecting cell functioning (Thavaselvam &Vijayaraghavan, 2010). Many plant species produce different and extremely lethal types of toxins and have the potential to be used as a BWA (Jansen *et al.*, 2014; Sharma *et al.*, 2016; Janik *et al.*, 2019; Kaufer *et al.*, 2020; Dass, 2021).

2. PLANT TOXINS

A large number of plants produce ribosome inactivating proteins (RIPs), which are catalytic enzymes that act intracellularly, inhibiting eukaryotic protein synthesis, thus leading to apoptosis and cell death (Endo *et al.*, 1998; Craik *et al.*, 2002; Giansanti *et al.*, 2010). RIPs have been identified in more than 60 different plant species, and have also been found in fungi, bacteria and algae. Currently, more than 50 type I RIPs and approximately 15 type II RIPs have been identified (Sha *et al.*, 2010; Yang *et al.*, 2016). Type I RIPs are the most numerous and are all synthesized as a single chain enzyme of approximately 30 kD. Contrarily, type II RIPs show two polypeptide chains: a smaller A-chain and a larger B-chain, connected by a disulfide bond. The lectin properties of the B chain (~35 kDa) enable toxin binding to cell-surface carbohydrates, while the A-chain (~30 kDa) possesses catalytic activity (de la Cruz *et al.*, 1995; Walsh *et al.*, 2013; Yang *et al.*, 2016). Lectins such as ricin, abrin, modeccin, viscumin and volkensin come under the group of toxic lectins of A-and B-chains. The enzyme component is not active until released by the native toxin (A + B) (Patočka & Středa, 2003; Bolognesi *et al.*, 2016; Polito *et al.*, 2019). Isolated A subunits are enzymatically active but do not have the ability to bind at the cellular level. Instead, isolated B subunits can bind to target cells (and even block the binding of the native toxin), but their activity is non-toxic (de la Cruz *et al.*, 1995). The initial binding of the B-chain to the glycoside residues on the glycoproteins and on the glycolipids on the cell membrane causes endocytosis of the toxin. All plant RIPs, including all type I toxins and the A-chains of type II toxins, are RNA N-glycosidases capable of hydrolyzing the nitrogen–carbon glycosidic bond of a specific adenosine located in the sarcin / ricin domain of the largest ribosomal RNA (Endo *et al.*, 1998; Yang *et al.*, 2016). However, recent evidence shows that RIPs not only deadenylate ribosomal RNA, but are also capable of removing adenine residues from DNA and several other polynucleotide substrates. Thus, it has been proposed to rename RIPs as polynucleotide-adenosine-glycosidases (PAGs) (Shakirova & Bezrukova, 2007).

The B-chain is able to bind the glycoside residues on glycoproteins and glycolipids, causing endocytosis of the toxin. Intracellular toxin transport occurs due to the endosomal system until reaching the Golgi apparatus, with this transport seemingly being regulated by the intracellular Ca^{2+} levels (Lord & Roberts, 1998). Subsequently, the association with the Golgi apparatus appears to be necessary for the consequent trafficking of the endoplasmic reticulum (ER) (Endo *et al.*, 1998). Once delivered to the ER, the disulfide isomerase protein can reduce the disulfide bridge between subunits, promoting retrograde transport of the A-chain (Lord & Roberts, 1998). Afterwards, at the cytoplasmic level, the A-chain can interact with the ribosome, which acts as a suicidal chaperone stimulating proper refolding and resumption of catalytic activity. It cleaves one specific adenosine residue (A4324) near the 3'-end of 28S ribosomal RNA. This targeted cleavage blocks elongation factors (EFs) 1 and 2 from binding, thus inhibiting protein synthesis (Lord & Roberts, 1998; Bolognesi *et al.*, 2016; Sowa-Rogozińska *et al.*, 2019). Ribosomal inactivation disrupts cell repair mechanisms and induces cell death by apoptosis. Unlike their type II counterparts, type I RIPs exhibit low toxicity because they are not able to bind and cross the cell membrane efficiently. In contrast, type I RIPs are cytotoxic to some cells such as macrophages (Polito *et al.*, 2019). Cells can absorb type I RIPs through the pinocytosis mechanism resulting in cell death. Recently, a new type of RIP, called type III RIP, has been isolated from *Hordeum vulgare*, the common barley plant (De Zaeytijd & Van Damme, 2017). This protein consists of an amino-terminal domain similar to type I RIP and is linked to an uncorrelated carboxyl-terminal domain with unknown function (Bolognesi *et al.*, 2016; De Zaeytijd & Van Damme, 2017).

As all RIPs are very similar to each other, consequently the poisoning symptoms are almost identical and the action mechanism of the toxic proteins is the same (de Virgilio *et al.*, 2010; Walsh *et al.*, 2013). Toxic effects of ricin have a latent period and take 2 to 24 hours to develop. After ingestion, the main symptoms are abdominal pain, vomiting and diarrhea, often with blood. The toxin causes intestinal bleeding and can also cause widespread nephritis as well as multiple necrosis in the liver and kidneys (Assiri, 2012; Moshiri *et al.*, 2016). In the myocardium, the myofibrils undergo degeneration. Within several days, there is severe dehydration, decrease in urine, thirst, burning throat, headache and the patient may die from hypovolemic shock. The patients' temperature decreases before death, and they often undergo characteristic shivering. Death occurs in exhaustion or cramp (Patočka & Středa, 2003; de Virgilio *et al.*, 2010; Walsh *et al.*, 2013).

When given parenterally, ricin is twice as toxic as the most dangerous snake venoms and is probably the most toxic parenteral substance in the plant kingdom. After parenteral administration, the patient may be present with fever, leukocytosis, and then falling blood pressure and temperature. The primary target organs are the kidney, liver and pancreas. Currently, from the literary data, abrin is the most toxic (Patočka & Středa, 2003). Due to the extreme toxicity of these compounds and their capacity to be used as BWAs, they are in the schedules of controlled BAs and toxins (Janik *et al*., 2019).

2.1 Ricin

Ricin toxin, discovered in 1888, is known as the first plant lectin from the seeds of the castor plant, *Ricinus communis* L. (*Euphorbiaceae*) (Winder, 2004). *R. communis* is autochthonous to the southeastern Mediterranean region, eastern Africa and India, but is now diffuse throughout temperate and subtropical regions. It has been cultivated primarily for castor oil (de la Cruz *et al.*, 1995; Worbs *et al.*, 2011). In Ancient Egypt, Europe, India and China, castor oil has been used for lighting, body ointments, and for purgative and cathartic use. As this plant is commonly found in the wild and often used as an ornamental plant, it is easily accessible. Ricin can be made from the waste material left over from the processing of castor oil (Audi *et al.*, 2005; Griffiths, 2011). Ricin at room temperature is stable, but can be inactivated by heat above 80 °C. After oil extraction and inactivation of ricin, the defatted mash and seed husks are used as animal feed and fertilizer respectively (Endo *et al.*, 1998; Polito *et al.*, 2019). In the last decade, ricin has been used for studies of cell biology mechanisms, immunology, treatment against AIDS and cancer (Yang *et al.*, 2016; Janik *et al.*, 2019). Castor seed poisoning is very common in countries where the plant is abundant, as only five seeds are needed to induce a toxic dose. Given its production costs and its multiple uses, castor seeds are currently being produced in more than 30 countries in the world with annual production of more than 1.5 million metric tons (Patel *et al.*, 2016). The accessibility and high toxicity of ricin toxin renders it as a high-risk asymmetric threat agent to national security and public health. Due to these characteristics, ricin is classified as a Category B agent by the US Centers for Disease Control and Prevention (CDC) (CDC, 2003). Agents in this category are considered as moderately easy to disseminate and able to cause low / middle mortality. Ricin is also monitored as a Schedule 1 agent under the Chemical Weapons Convention. This concern is due to the fact that during World War II, the US army tested artillery shells loaded with high doses of ricin (Cenciarelli *et al.*, 2013; Berger *et al.*, 2016).

2.2 Abrin

Abrin is derived from seeds of *Abrus precatorius* L. plant (*Fabaceae* or *Leguminosae*) that has more than 30 common names, one of which is rosary pea plant (Wellner *et al.*, 1995). This species of plant is native to Southeast Asia, and grows well in both tropical and subtropical areas of the world where it has been introduced (Patočka & Středa, 2003). It has been recorded in Ayurvedic medicine that the leaves of *Abrus precatorius* are laxative, expectorant and aphrodisiac, while the seeds are reportedly purgative, emetic, tonic, antiphlogistic, aphrodisiac and anti-ophthalmic. The easy availability of abrin toxin and its high toxicity lead to concerns that it could pose a severe threat to public health (Lin, 1994; Liu *et al.*, 2016). The mechanism of toxic action of abrin is identical to that of ricin, but the toxicity of abrin in mice is 75 times higher that of ricin (0.04 μg/kg for abrin as compared to 3μg/kg for ricin). The diagnosis, clinical features, treatment, protection and prophylaxis is also the same for both abrin and ricin intoxications (Patočka & Středa, 2006). Hence, abrin is classified as a Category B agent by the CDC and placed in the category of Biological Select Agents or Toxins by the US Department of Health and Human Services (HHS) (Janik *et al.*, 2019). It should be reported that in 2019, the terrorist group called Jamaah Ansharut Daulah (JAD) produced bombs containing abrin. The attack was promptly stopped by local law enforcement without causing casualties. Although there is currently no further data regarding the use of abrin as a BA, it represents one of the possible candidates for a bioterrorist attack (Cenciarelli *et al.*, 2013; Dass, 2021).

2.3 Modeccin

Modeccin is a lectin from the roots of *Adenia digitata*, an African succulent plant that is comparable in toxicity to ricin and acts by the same mechanism (Endo *et al.*, 1998). The plant does not seem to have any specific use (e.g., food, drugs or animal feed) and so is not available in quantities comparable to abrin or ricin (Patočka & Středa, 2006). However, the seeds do seem to be readily available. The subunits are isolated of modeccin (later referred to as modeccin 4B) and purified from the roots of *Adenia digitata* using affinity chromatography on Sepharose 4B (called Modeccin 4B). As previously described on the structure of lectins, modeccin also has a subunit A (~26 kDa), which inhibits protein synthesis and a B subunit (~ 31 kDa), which binds to cells (Patočka & Středa, 2006; Worbs *et al.*, 2011). A second form of modeccin is purified using affinity chromatography on acid-treated Sepharose 6B, with this form subsequently termed as modeccin 6B. The latter has a molecular weight indistinguishable from that of modeccin 4B, and consists of two subunits of 27 and 31 kDa, linked by a disulphide bond. As compared with modeccin 4B, modeccin 6B is slightly less toxic to animals, does not agglutinate erythrocytes, and is a more potent inhibitor of protein synthesis, giving 50% inhibition at the concentration of 0.31 mg/ml (Patočka & Středa, 2006).

2.4 Viscumin

Viscumin (Mistletoe lectin I, ML I), belonging to the RIPs family, was identified in the late 1980s as the main pharmacologically-active ingredient of mistletoe (*Viscum album*) extract and is largely responsible for its toxicity. Very similar heterodimeric toxic viscumin was isolated from a partial-parasite obtained from Indian western Himalayas (Patočka & Středa, 2006). The purified viscumin from this source shows considerable sequence and structural differences with the European viscumin. The root mean-square-deviations (rms) calculated for α–carbon atoms of European ML-1 and Indian viscumin shows higher deviations for the A chain and lower for the B chain (Endo *et al.*, 1998). The highest deviations are found for the residues on the surface. The association of A- and B-subunits is predominantly hydrophobic in nature (de la Cruz *et al.*, 1995; Endo *et al.*, 1998; Patočka & Středa, 2006; Worbs *et al.*, 2011). In terms of toxicity it is comparable with the ricin, and like all RIPs, it has the same mechanism of action previously described (Ochocka & Piotrowski, 2002).

2.5 Volkensin

Volkensin is a lectin from *Adena volkensii* (kilyambiti plant) that is comparable in toxicity to ricin and has the same mechanism of action (like a RIP) (Olsnes *et al.*, 1982; Endo *et al.*, 1998). The plant is a relatively unattractive and toxic succulent plant found in Africa that appears to be of little interest. However, it has proven useful as a research reagent in neurology because of its ability to be taken up and transported by some types of nerve (Olsnes *et al.*, 1982; Stirpe *et al.*, 1982). There may be pressure to develop commercial sources for the research community (Patočka & Středa, 2006).

3. PLANT TOXINS AS BIOWEAPONS

During World War I, ricin was taken into consideration as a potential offensive BWA (Pita, 2009; Cenciarelli *et al.*, 2013). However, the thermal instability (stable under 80 °C) of ricin constrained its initial use in exploding shells, while ethical and treaty issues limited its use as a poison or blinding agent (Moshiri *et al.*, 2016; Polito *et al.*, 2019). The war ended before ricin was weaponized and tested as BWA (Morse, 2012; Cenciarelli *et al.*, 2013). During World War II, ricin was produced, armed into W-bombs (bombs containing ricin) and tested, but apparently was never used in battlefield. Interest in ricin continued for a short period after World War II, but soon subsided when the US Army Chemical Corps began a program to weaponize another more lethal agent, sarin (Seto *et al.*, 2007; Cenciarelli *et al.*, 2013). During the Cold War, the Soviet Union also studied ricin as a possible BWA. Ken Alibek, a former top official involved in Russia's BWA program who defected to the US, claimed that Russia developed ricin toxin as BWA, and that the ricin toxin used against the Bulgarian exiles Georgi Markov and Vladimir Kostov was created in Russian

laboratories (Roxas-Duncan & Smith, 2014). In 1989, around 10 L of concentrated ricin solution was produced in Iraq, some of which were used as a payload in artillery shells. In addition, further evidence demonstrated the manufacture and storage of large quantities of AFs and BTX in Iraq (Riedel, 2004). In 1992, around 120 tons of castor beans were identified through non-government sources in Iran, presumably for the production of ricin, while in 2001, ricin was found in Afghanistan after the fall of the Taliban government (Cenciarelli *et al.*, 2013). Although the potential use of ricin as a military weapon has been studied, its usefulness as a weapon of mass destruction as compared to conventional weapons still remains controversial. It has been estimated that eight tons of ricin should be aerosolized over an area of 100 km^2 to obtain about 50% of losses, while only a small quantity of kilograms of anthrax spores would have the same effect (Ludovici *et al.*, 2015). Furthermore, large-scale ricin dispersion is logistically impractical. Therefore, even if ricin is easy to produce, it is not so likely that it could cause large-scale victims as compared to other possible agents (Madsen, 2001). Abrin is not known (to date) to have been used successfully in any wars or terrorist attacks, but there has been an attempt made by a terrorist group to incorporate abrin poison into suicide bombs (Dass, 2021). However, a large number of abrin poisoning incidents have been documented (Roxas-Duncan & Smith, 2014). Other cases of intoxication were caused by exposure to modeccin, viscumin and volkensin. Many scientists, mainly from the US Department Homeland of Security (DHS), have repeatedly pointed to the dangers of these substances that could be used as BWAs (Cenciarelli *et al.*, 2013).

3.1 Umbrella Murder

Although ricin is not considered as an effective weapon of mass destruction, its potential as a BWA should be taken into account. The most emphasized case, known as the Umbrella Murder by the Bulgarian dissident Georgi Markov in 1978, is the first case in the recent history of biocrime (Papaloucas *et al.*, 2008; Musshoff & Madea, 2009; Polito *et al.*, 2019). Markov was a 49 year old Bulgarian novelist and writer who left Bulgaria to move to England in the 1970s. In London, he had published and broadcasted anti-communist points of view. On 7 September 1978, while waiting at a bus station, he felt a painful blow to his right leg and immediately saw a man with an umbrella (Polito *et al.*, 2019). The next day, he was admitted to the hospital with high fever, vomiting and difficulty speaking. He showed a wound with 6 cm of diameter with inflammation and hardening in the thigh (Musshoff & Madea, 2009). Three blood cultures were negative. His white blood cell count was 10,600 cells per µL. The next day, Markov suffered from a septic shock syndrome with vascular collapse. Subsequently, his white blood cell count rose to 26,300 cells per µL. Later, Markov stopped passing urine and the vomit became bloody. Four days after the attack, his electrocardiogram showed a complete conduction block (Papaloucas *et al.*, 2008). A few hours later, Markov died. Autopsy revealed pulmonary edema, fatty change of the liver, hemorrhagic necrosis of the small intestines, as well as interstitial hemorrhage in the testicles, pancreas and inguinal lymph nodes (Papaloucas *et al.*, 2008).

Vladimir Kostov was another Bulgarian exile who fled to Paris. On 26 August 1978, just two weeks before Markov's murder, Kostov felt a similar blow on his shoulders while on the subway. Kostov had high fever and was hospitalized for 12 days, but he recovered completely (Musshoff & Madea, 2009). X-rays showed a metallic foreign body in his back. An identical one was removed from Markov's leg (Riedel, 2004). Kostov wore heavy clothes, and perhaps that is why the metal body did not penetrate deep enough into his body to melt the wax casing. It has been estimated that the holes could have contained 500µg of lethal substance inside. Although no substance has ever been found in these two granules, agents such as BTX or SEB have been considered as possible causes (Riedel, 2004; Papaloucas *et al.*, 2008; Musshoff & Madea, 2009). The circumstances suggested that probably ricin was used in the attacks. It has always been thought that the instigator of these two murders was the Bulgarian government. Instead it was reported that ricin was produced and sent to Bulgaria by the Soviet Union. However, this has not been demonstrated (Riedel, 2004; Musshoff & Madea, 2009). Despite the KGB's denial, high-profile defectors Oleg Kalugin and Oleg Gordievsky have since confirmed the KGB's involvement (Riedel, 2004).

3.2 Ricin and Abrin: Biocrimes & Bioterrorism – 1981-2020

All major events, starting from 1981 until 2020, in which ricin was used intentionally as BW are listed as follows. An attack by terrorist organizations aimed at hitting a large number of individuals is to be considered as a bioterrorist attack; while the use, albeit intentional, carried out for example by problematic ordinary citizens or by petty criminals who could easily obtain minimal amounts of ricin is classified as biocrimes.

- In 1981, exposed CIA double agent Boris Korczak was reportedly shot with a ricin-laced pellet. He survived this assassination attempt that was probably organized by the KGB (CDC, 2003).
- In 1982, W. Chanslor, a Texas lawyer was fined and sentenced to jail for plotting to kill his wife with ricin (CDC, 2003).
- In 1985, Montgomery Todd Meeks, a high school senior, was convicted of attempted murder in a plot to kill his father using ricin (CDC, 2003).
- In 1991, members of the Minnesota Patriots Council acquired castor beans and planned to use ricin to assassinate local deputy sheriffs, US Marshals, and IRS agents. They were convicted in 1994 and 1995 under the Biological Weapons Anti-Terrorism Act (BWATA) law (Roxas-Duncan & Smith, 2014).
- On 21 April 21 1992, the Washington Post published an article about an unsuccessful attempt to poison Soviet political opponent Alexander Solzhenitsyn with ricin (Bozza *et al.*, 2015).
- In 1995, Deborah Green, a non-practicing oncologist from Kansas, US, attempted to kill her husband, Michael Farrar, a cardiologist, with ricin (Bozza *et al.*, 2015).
- In November 1999, FBI agents apprehended James Kenneth Gluck in Tampa, Florida, US for threatening to murder court officials in Jefferson County, Colorado, US with ricin (Roxas-Duncan & Smith, 2014).
- In August 2002, the Sunni militant group Ansar-al-Islam was reported to have been testing BWAs, including ricin, at a small facility in Iraq, experimenting on animals and humans (CDC, 2003).
- In December 2002, six terrorist suspects were arrested in Manchester, UK. Their apartment was serving as a ricin laboratory. Among them was a chemist who was producing the toxin (CDC, 2003).
- In January 2003, authorities arrested six Algerians in Wood Green, UK, whom they claimed were manufacturing ricin as part of a plot for a bioterrorist attack on the London Underground (Edwards & Gomis, 2011).
- In October 2003, a package and letter sealed in a ricin contaminated envelope was intercepted at a post office in Greenville (South Carolina, USA). The letter was signed "Fallen Angel" and threatened to poison water supplies if demands were not met (CDC, 2003).
- In November 2003, a letter addressed to the White House was intercepted. The letter contained a fine powdery substance that later tested positive for ricin, which investigators said was of low potency and was not considered a health risk (Bhalla & Warheit, 2004).
- In February 2004, traces of ricin were discovered on an automatic mail sorter in the mailroom of the Dirksen Senate Office building in Washington DC, which handled mails addressed to the Senate Majority Leader, Bill Frist (Bhalla & Warheit, 2004).
- In January 2005, the FBI arrested a man in Florida, USA after agents found ricin in his home (Roxas-Duncan & Smith, 2014).
- On 3 October 2006, a man from Phoenix, Arizona, US was sentenced to seven years in prison for attempting to manufacture ricin (Roxas-Duncan & Smith, 2014).
- In 2007, traces of ricin had been found at Limerick Prison, Ireland. The ricin was smuggled into Ireland from the US. in a contact lens case, to be used in a murder plot (Roxas-Duncan & Smith, 2014).
- In February 2008, authorities recovered castor beans, a weapons cache, a copy of "The Anarchist Cookbook" with a page about ricin marked, and 4 g of ricin in Las Vegas, Nevada, US (Schieltz *et al.*, 2011; Shea & Gottron, 2013).
- In June 2009, Ian Davison was arrested after the discovery of ricin at a house in County Durham, UK. Davidson, a British white supremacist and neo-Nazi, was sentenced to 10 years of prison in May 2010 for preparing acts of bioterrorism (Roxas-Duncan & Smith, 2014).

- In January 2011, the FBI arrested a man from Coventry Township, Ohio, US for unlawful possession of ricin (Roxas-Duncan & Smith, 2014).
- In June 2011, Michael Crooker was sentenced to 15 years in prison for illegally possessing ricin and threatening a prosecutor (Roxas-Duncan & Smith, 2014).
- In June 2011, a British citizen, Asim Kauser, was brought to court on charges including possessing instructions for producing ricin (Roxas-Duncan & Smith, 2014).
- In August 2011, the US government discovered information that terrorist groups were attempting to obtain large amounts of castor beans for weaponizing ricin (Shea & Gottron, 2013).
- On 1 November 2011, four elderly men from Georgia, US were arrested relating to plans to obtain ricin for use in attacks against other US citizens, as well as government personnel and officials (Bjelopera, 2017).
- On 16 April 2013 an envelope addressed to Senator Roger Wicker of Mississippi tested positive for ricin at the US Capitol's off-site mail facility. A few days later, the Secret Service announced that a letter addressed to the US President, Barrack Obama, containing a "suspicious substance", was intercepted at the White House's off-site mail facility on that day. Later that the day, the FBI confirmed that the letter tested positive for ricin (Gibb & Kes, 2013).
- In March 2014, at a student at Georgetown University, US, Daniel Harry Milzman was arrested and charged for possessing a biological toxin after admitting he made ricin in his dorm room. Milzman was later sentenced to one year in prison (Mickolus, 2016).
- On 4 June 2014, Jeff Boyd Levenderis was convicted of possessing ricin for use as a weapon and also possessing of ricin and making false statements to agents of the FBI. He was later sentenced to six years in prison (Burke, 2017).
- On 30 November 2017, 71 year old Betty Miller was arrested and charged with unregistered possession of a select agent (Burke, 2017).
- In June-July, 2018, a Tunisian man was arrested in the German city of Cologne for allegedly obtaining ingredients for the production of ricin on the internet. Furthermore, the man bought 1,000 castor oil seeds and an electric coffee grinder from an internet mail order company. A month later, the Tunisian man wife's was also arrested for complicity. Both were accused of being supporters of the Islamic State (Flade, 2018).
- In October 2018, authorities arrested a US Navy veteran in Utah over suspicious envelopes sent to the US President, Donald Trump and top military chiefs. Officials suspected the envelopes to have contained ricin (Yang *et al.*, 2021).
- In October 2019, the Indonesian police foiled a bomb attack plot by the Islamic State-affiliated terrorist group JAD, who manufactured bombs that after several analyses showed they contained abrin (Dass, 2021).
- In September 2020, a package containing ricin, which was addressed to President Donald Trump, was intercepted by law enforcement. A Canadian woman suspected of sending it was arrested when she tried to cross to the Canadian-US border (Yang *et al.*, 2021).

4. CONCLUSION

Biowarfare and bioterrorism represent a serious threat to the health of human beings and to the socioeconomic stability of counties. Among the possible agents that can be used for biothreat purposes, plant toxins represent a novel and still not completely explored field. Specifically, plant proteins with toxic effects, such as ricin, abrin, modeccin, viscumin and volkensin, have aroused interest due to their ease of availability and dangerousness for the purpose of being used as BWAs. The role of these enzymatic proteins, namely RIPs in plant physiology is not entirely clear. Based on their varied activity at the ribosomal level, different possible roles have been proposed, including antiviral activity, antifungal activity, defense against herbivores, a role in stopping cellular metabolism during periods of senescence and finally as reserve proteins.

Ricin and abrin, among others, have been used in the recent past in several occasions to perpetrate biocrimes due to their availability and ease of extraction from the plants' seeds, as well as due to their toxicity. In many cases, their use resulted in serious consequences and even in the death of the victims. The use of biological

agents with the aim to perpetrate crimes is an actual and serious threat. Currently, the use of plant toxins for offensive purposes represents a real possibility, and research and development of strategies and approaches to mitigate their possible development and use cannot be neglected.

REFERENCES

Assiri, A.S. (2012). Ricin poisoning causing death after ingestion of herbal medicine. *Ann. Saudi. Med.*, **32**: 315-317.

Atlas, R.M. (2002). Bioterrorism: from threat to reality. *Ann. Rev. Microbiol.*, **56**: 167-185.

Audi, J., Belson, M., Patel, M., Schier, J. & Osterloh, J. (2005). Ricin poisoning: a comprehensive review. *JAMA.*, ***294***: 2342-2351.

Barras, V. & Greub, G. (2014). History of biological warfare and bioterrorism. *Clin. Microbiol. Infect.*, **20**: 497-502.

Becker, A.M. (2004). Smallpox in Washington's army: Strategic implications of the disease during the American Revolutionary War. *J. Mil. Hist.*, **68**: 381-430.

Berger, T., Eisenkraft, A., Bar-Haim, E., Kassirer, M., Aran, A.A. & Fogel, I. (2016). Toxins as biological weapons for terror-characteristics, challenges and medical countermeasures: a mini-review. *Disaster. Mil. Med.*, **2**: 7.

Bhalla, D.K. & Warheit, D.B. (2004). Biological agents with potential for misuse: a historical perspective and defensive measures. *Toxicol. Appl. Pharmacol.*, **199**: 71-84.

Bjelopera, J.P. (2017). Domestic terrorism: An overview. *Washington, DC: Congressional Research Service*.

Black, R.M. & Read, R.W. (2007). Environmental and biomedical sample analysis in support of allegations of use of chemical warfare agents. *Toxin Rev.*, **26**: 275-298.

Bolognesi, A., Bortolotti, M., Maiello, S., Battelli, M.G. & Polito, L. (2016). Ribosome-Inactivating Proteins from Plants: A Historical Overview. *Molecules.*, **2**: 1627.

Bozza, W.P., Tolleson, W.H., Rosado, L.A.R. & Zhang, B. (2015). Ricin detection: tracking active toxin. *Biotechnol. Adv.*, **33**: 117-123.

Burke, R.A (2017). Counter-terrorism for emergency responders. *CRC Press*.

Cenciarelli, O., Rea, S., Carestia, M., D'Amico, F., Malizia, A., Bellecci, C., Gaudio, P., Gucciardino, A. & Fiorito, R. (2013). Biological Weapons and Bio-Terrorism: a review of History and Biological Agents. *Defence S&T Tech. Bull.*, **6**: 111-129.

Christopher, L.G.W., Cieslak, L.T.J., Pavlin, J.A. & Eitzen, E.M. (1997). Biological warfare. A historical perspective. *JAMA.*, **278**: 412-417.

Control and Prevention (CDC). (2003). Investigation of a ricin-containing envelope at a postal facility-South Carolina, 2003. *MMWR Morb. Mortal. Wkly. Rep.*, **5**2: 1129-1131.

Craik, D.J., Daly, N.L., Plan, M.R., Salim, A.A. & Sando, L. (2002). Structure and function of plant toxins (with emphasis on cystine knot toxins). *Toxin Rev.*, **21**: 229-271.

D'Amelio, E., Gentile, B., Lista, F. & D'Amelio, R. (2015). Historical evolution of human anthrax from occupational disease to potentially global threat as bioweapon. *Environ. Int.*, **85**: 133-146.

Dass, R.A.S. (2021). Bioterrorism. *CTTA*, **13**: 16-23.

de la Cruz, R.R., Pastor, A.M. and Delgado-Garcia, J.M. (1995). The neurotoxic effects of Ricinus communis agglutinin-II. *Toxin Rev.*, **14**: 1-46.

de Virgilio M., Lombardi, A., Caliandro, R. & Fabbrini, M. S. (2010). Ribosome-inactivating proteins: from plant defense to tumor attack. *Toxins*., **2**: 2699-2737.

De Zaeytijd, J. & Van Damme, E.J. (2017). Extensive Evolution of Cereal Ribosome-Inactivating Proteins Translates into Unique Structural Features, Activation Mechanisms, and Physiological Roles. *Toxins.*, **9**: 123.

Edwards, J. & Gomis, B. (2011). Islamic Terrorism in the UK since 9/11: Reassessing the 'Soft' response. *International Security Programme Paper–ISP*.

Endo, Y., Morishita, R., Imashevich, K.M. & Yoshinari, S. (1998). Mechanisms of action of ribotoxins. *Toxin Rev.*, **17**: 427-439.

Flade, F. (2018). The June 2018 Cologne Ricin Plot: A New Threshold in Jihadi Bio Terror. *CTC. Sentinel.*, **11**: 1-4.

Giansanti, F., Di Leandro, L., Koutris, I., Cialfi, A., Benedetti, E., Laurenti, G., Pitari, G. & Ippoliti R. (2010). Ricin and saporin: plant enzymes for the research and the clinics. *Curr. Chem. Biol.*, **4**: 99-107.

Gibb, J. & Kes, T. (2013). The Parthenon, April 18, 2013. *Parthenon.*, 217.

Gori, S. & Tomar A.S. (2020). Bioterrorism & Biodefense: An Environmental and Public Health Preparedness. *Rupkatha J. Interdiscip. Stud. Humanit.*, **12**: 1-15.

Griffiths, G.D. (2011). Understanding ricin from a defensive viewpoint. *Toxins.*, **3**: 1373-1392.

Janik, E., Ceremuga, M., Saluk-Bijak, J. & Bijak, M. (2019). Biological Toxins as the Potential Tools for Bioterrorism. *Int. J. Mol. Sci.*, **20**: 1181.

Jansen, H.J., Breeveld, F.J., Stijnis, C. & Grobusch, M.P. (2014). Biological warfare, bioterrorism, and biocrime. *Clin. Microbiol. Infect.*, **20**: 488-496.

Kaufer, A.M., Theis, T., Lau, K.A., Gray, J.L. & Rawlinson, W.D. (2020). Biological warfare: the history of microbial pathogens, biotoxins and emerging threats. *Microbiol. Aust.*, **41**:116-122.

Klietmann, W.F. & Ruoff, K.L. (2011). Bioterrorism: implications for the clinical microbiologist. *Clin. Microbiol. Rev.*, **14**: 364-381.

Koch, L., Lopes, A.A., Maiguy, A., Guillier, S., Guillier, L., Tournier, J.N. & Biot, F. (2020). Natural outbreaks and bioterrorism: How to deal with the two sides of the same coin?. *J. Glob. Health*, **10**: 020317.

Lee, E. & Kim, Y. (2021). Factors affecting the competency of nursing students regarding bioterrorism. *Iran. J. Public Health*, **50**: 842-843.

Lin, J.Y. (1994). Antitumor protein: abrin. *Toxin Rev.*, **13**: 219-228.

Liu, X., Zhao, Y., Sun, C., Wang, X., Wang, X., Zhang, P., Qiu, J., Yang, R. & Zhou, L. (2016). Rapid detection of abrin in foods with an up-converting phosphor technology-based lateral flow assay. *Sci. Rep.*, **6**: 34926.

Lord J.M. & Roberts, L.M. (1998). Toxin entry: retrograde transport through the secretory pathway. *J. Cell. Biol.*, **140**: 733-736.

Ludovici, G.M., Gabbarini, V., Cenciarelli, O., Malizia, A., Tamburrini, A., Pietropaoli, S., Carestia, M., Gelfusa, M., Sassolini, A., Di Giovanni, D., Palombi, L., Bellecci, C. & Gaudio, P. (2015). Innovative techniques for the detection of Biological Warfare Agents. *Defence S&T Tech. Bull.*, **8**: 17-26.

Madsen, J.M. (2001). Toxins as weapons of mass destruction. A comparison and contrast with biological-warfare and chemical-warfare agents. *Clin. Lab. Med.*, **21**: 593-605.

Mannik, E. (2009). Terrorism: Its Past, Present and Future Prospects. *ENDC Proceedings*., **12**: 151-171.

Mickolus, E. (2016). Terrorism, 2013-2015. *A world chronology. McFarland & Company*.

Morse, S.S. (2012). Public health surveillance and infectious disease detection. *Biosecur. Bioterror.*, **10**: 6-16.

Moshiri, M., Hamid, F. & Etemad, L. (2016). Ricin Toxicity: Clinical and Molecular Aspects. *Rep. Biochem. Mol. Biol.*, **4**: 60-65.

Musshoff, F. & Madea, B. (2009). Ricin poisoning and forensic toxicology. *Drug. Test. Anal.*, **1**: 184-191.

Ochocka, J.R. & Piotrowski, A. (2002). Biologically active compounds from European mistletoe (Viscum album L.). *Can. J. Plant Pathol.*, **24**: 21-28.

Oliveira, M., Mason-Buck, G., Ballard, D., Branicki, W. & Amorim, A. (2020). Biowarfare, bioterrorism and biocrime: A historical overview on microbial harmful applications. *Forensic Sci. Int.*, **314**: 110366.

Olsnes, S., Stirpe, F., Sandvig, K. & Pihl, A. (1982). Isolation and characterization of viscumin, a toxic lectin from Viscum album L. (mistletoe). *J. Biol. Chem.*, **257**: 13263-13270.

Papaloucas, M., Papaloucas, C. & Stergioulas, A. (2008). Ricin and the assassination of Georgi Markov. *Pak. J. Biol. Sci.*, **1**: 2370-2371.

Patel, V.R., Dumancas, G.G., Viswanath, L.C.K., Maples, R. & Subong, B.J.J. (2016). Castor Oil: Properties, Uses, and Optimization of Processing Parameters in Commercial Production. *Lipid. Insights.*, **9**: 1-12.

Patočka, J. & Středa, L. (2003). Plant toxic proteins and their current significance for warfare and medicine. *J. Appl. Biomed.*, **1**: 141-147.

Patočka, J. & Středa, L. (2006). Protein biotoxins of military significance. *Acta. Medica.*, **49**: 3-11.

Pita, R. (2009). Toxin weapons: from World War I to jihadi terrorism. *Toxin Rev.*, **28**: 219-237.

Polito, L., Bortolotti, M., Battelli, M.G., Calafato, G. & Bolognesi, A. (2019). Ricin: An Ancient Story for a Timeless Plant Toxin. *Toxins.*, **11**: 324.

Ranlet, P. (2000). The British, the Indians, and smallpox: what actually happened at Fort Pitt in 1763?. *Pa. Hist.*, **67**: 427-441.

Riedel, S. (2004). Biological warfare and bioterrorism: a historical review. *Proc. (Bayl. Univ. Med. Cent.)*, **17**: 400-406.

Roxas-Duncan, V.I. & Smith, L.A. (2014). Of beans and beads: ricin and abrin in bioterrorism and biocrime. *J. Bioterror. Biodef.*, 5.

Schieltz, D.M., McGrath, S.C., McWilliams, L.G., Rees, J., Bowen, M.D., Kools, J.J., Dauphin, L.A., Gomez-Saladin, E., Newton, B.N., Stang, H.L., Vick, M.J., Thomas, J., Pirkle, J.L. & Barr, J.R. (2011). Analysis of active ricin and castor bean proteins in a ricin preparation, castor bean extract, and surface swabs from a public health investigation. *Forensic. Sci. Int.*, **209**: 70-79.

Seto, Y., Kanamori-Kataoka, M., Tsuge, K., Ohsawa, I., Iura, K., Itoi, T., Sekiguchi, H., Matsushita, K., Yamashiro, S., Sano, Y., Sekiguchi, H., Maruko, H., Takayama, Y., Sekioka, R., Okumura, A., Takada, Y., Nagano, H., Waki, I., Ezawa, N., Tanimoto, H., Honjo, S., Fukano, M. & Okada, H. (2007). Development of an on-site detection method for chemical and biological warfare agents. *Toxin Rev.*, **26**: 299-312.

Sha, O., Yew, D.T.W., Ng, T.B., Yuan, L. & Kwong, W.H. (2010). Different in vitro toxicities of structurally similar type I ribosome-inactivating proteins (RIPs). *Toxicol. In Vitro.*, **24**: 1176-1182.

Shakirova, F.M. & Bezrukova, M.V. (2007). Current knowledge about presumable functions of plant lectins. *Zh. Obshch. Biol.*, **68**: 109-125.

Sharma, D., Mishra, A., Newaskar, V. & Khasgiwala, A. (2016). Bioterrorism: Law Enforcement, Public Health & Role of Oral and Maxillofacial Surgeon in Emergency Preparedness. *J. Maxillofac. Oral. Surg.*, **15**: 137-143.

Shea, D.A. & Gottron, F. (2013). Ricin: technical background and potential role in terrorism. *Library of Congress Washington DC Congressional Research Service.*

Sowa-Rogozińska, N., Sominka, H., Nowakowska-Gołacka, J., Sandvig, K. & Słomińska-Wojewódzka, M. (2019). Intracellular Transport and Cytotoxicity of the Protein Toxin Ricin. *Toxins.*, **11**: 350.

Stirpe, F., Sandvig, K., Olsnes, S. & Pihl, A. (1982). Action of viscumin, a toxic lectin from mistletoe, on cells in culture. *J. Biol. Chem.*, **257**: 13271-13277.

Thavaselvam, D. & Vijayaraghavan, R. (2010). Biological warfare agents. *J. Pharm. Bioallied. Sci.*, **2**: 179-188.

Walsh, M.J., Dodd, J.E. & Hautbergue, G.M. (2013). Ribosome-inactivating proteins: potent poisons and molecular tools. *Virulence.*, **4**: 774-784.

Wellner, R.B., Hewetson, J.F. & Poli, M.A. (1995). Ricin: mechanism of action, detection, and intoxication. *Toxin Rev.*, **14**: 483-522.

Wheelis, M. (2002). Biological warfare at the 1346 siege of Caffa. *Emerg. Infect. Dis.*, **8**: 971-975.

Winder, C. (2004). Toxicity of ricin. *Toxin. Rev.*, **23**: 97-103.

Worbs, S., Köhler, K., Pauly, D., Avondet, M.A., Schaer, M., Dorner, M.B. & Dorner, B.G. (2011). Ricinus communis intoxications in human and veterinary medicine-a summary of real cases. *Toxins.*, **3**: 1332-1372.

Yang, G. L., Li, S. M. & Wang, S. Z. (2016). Research progress in enzyme activity and pharmacological effects of ribosome-inactivity protein in bitter melon. *Toxin. Rev.*, **35**: 128-132.

Yang, J., Wang, C., Luo, L., Li, Z., Xu, B., Guo, L. & Xie, J. (2021). Highly sensitive MALDI-MS measurement of active ricin: insight from more potential deoxynucleobase-hybrid oligonucleotide substrates. *Analyst*, **146**: 2955-2964.

PERFORMANCE IMPROVEMENT IN WIRELESS SENSOR NETWORKS USING WHALE OPTIMISATION ALGORITHM (WOA) AND BUTTERFLY OPTIMISATION ALGORITHM (BOA)

Vaibhav Godbole

Department of Artificial Intelligence & Data Science,
Fr. Conceicao Rodrigues College of Engineering, India

Email: godbole@fragnel.edu.in

ABSTRACT

A sensor in wireless sensor networks (WSNs) senses, processes and transmits sensed information simultaneously. A large number of sensors are deployed for performing distributed sensing of the target field. During the data transmission, there is wastage of some energy. Therefore, minimising energy consumption is one of the challenges involved in the design and deployment of WSNs. The other WSN design and deployment challenges include precise node localisation, selection of cluster heads and high network lifetime. This paper evaluates the performance of whale optimisation algorithm (WOA) and butterfly optimisation algorithms (BOA) to overcome these challenges. We also compare the performance of WOA and BOA with reappointment low-energy adaptive clustering hierarchy (Re-LEACH) and fuzzy clustering algorithm (FCA). Our experiments show that WOA performs better than other algorithms regarding energy consumption and number of live nodes. Our analysis also indicates that WOA outperforms BOA by about 32.4%.

Keywords: *Wireless sensor network (WSN); Whale optimisation algorithm (WOA); butterfly optimisation algorithm (BOA); node localisation; energy efficient clustering.*

1. INTRODUCTION

Wireless sensor networks (WSNs) consist of many tiny, low-cost autonomous sensor nodes (either homogeneous or heterogeneous) to observe physical and environmental conditions. Correspondence range, adaptability, energy efficiency and throughput are significant requirements of WSN. At remote locations, sensor nodes continue to work until they are short on power. During the operation of WSNs, the energy consumption rate mainly depends on the node performance and its quantity (Liu *et al.*, 2017; Singh *et al.*, 2020). The sensor uses a wireless channel for data transmission. The allocation of the range of operating frequencies, channel bandwidth and synchronisation of available frequencies for communication are a few crucial issues in wireless communications (Kos *et al.*, 2019). In WSN, sensor nodes are formed, called clusters, for efficient data transmission. A cluster head (CH) is selected using a suitable technique for every cluster. Creating clusters and setting cluster heads is a challenging issue in WSN (Fanian *et al.*, 2019).

In WSN, nodes sense, process and gather data from the environment over wireless networks to the base station or the sink node, which act as the end node (Cui *et al.*, 2020). It is essential to know the origin of collected data and reported incidents in many sensor network applications. The localisation can be defined as the perseverance of the position of the unknown sensor nodes, known as target nodes, using the known position of the sensor nodes, known as anchor nodes, based on the measurement of parameters such as time difference of arrival, time of arrival, angle of arrival, triangulation and maximal likelihood (Arora *et al.*, 2017a). The localisation issue of WSN can be resolved by using a Global Positioning System (GPS) receiver with each sensor node, but this is not favourable due to energy, cost and size issues.

In this paper, we present the applications of a few swarm intelligence algorithms, namely whale optimisation (WOA) (Mohammed *et al.*, 2019) and butterfly optimisation (BOA) (Arora *et al.*, 2019; Maheshwari *et al.*, 2021) to resolve various problems in WSNs, such as energy consumption, network

lifetime and node localisation (Okwu *et al.*, 2020). We also evaluate the performance of these algorithms and compare them with that of other algorithms, namely fuzzy clustering algorithm (FCA) (Godbole, 2012) and a very recently proposed variant of low-energy adaptive clustering hierarchy (LEACH) - reappointment LEACH (Re-LEACH) (Pandey *et al*., 2019).

The rest of the paper is summarised as follows. Section 2 describes the problem domains in WSNs. The mathematical foundations of WOA and BOA are elaborated in Section 3. The performance evaluation of the algorithms is presented in Section 4. Finally, the conclusion and future scope are presented in Section 5.

2. WSN AND OPTIMISATION

Major factors such as energy efficiency, complexity of routing protocols, scalability, data aggregation for maximum throughput, network lifetime as well as the need for cluster formation are introspected by the designers while developing WSNs (Singh *et al.*, 2020). However, there is invariably a trade-off between one and the other factors. For example, if we need higher throughput, then more power is required. Therefore, to form better WSNs, we need to optimise these factors. One way of doing this is to use a more convenient optimiser or algorithm. We first discuss the problem domains in WSNs and then review the optimisation techniques available to date to solve them.

2.1 Problem Domains in WSNs

In this paper, we focused on the following problem domains:

- Network lifetime
- Node localisation
- Efficient node clustering

We briefly discuss each of these problem domains, followed by the work done to solve these issues using WOA and BOA in Section 4.

2.1.1 Network Lifetime

Network lifetime is the time period from the network's initial deployment to the first loss of coverage either due to loss of node energy or network partitioning such that there is no communication between sub-networks. As such, network lifetime can alternatively be defined as the time until the first node dies or time until several percentages of the nodes die (Yetgin *et al.*, 2017; Engmann *et al.*, 2018).

Various techniques can improve the network lifetime of WSN. Topology control for battery preservation (Ahmed *et al*.,2017) and adjusting the distance between a source node and sink to save the battery (Ahmed *et al.*, 2019) are a few of them.

2.1.2 Data Aggregation

Data aggregation combines the sensor data using aggregation approaches (Randhawa *et al.*, 2017). In WSN, data aggregation is necessary to minimise the available resources and minimise nodes' energy consumption. Figure 1 shows different methods for data aggregation. In the centralised approach, every node transmits its sensed data to the central node, an influential node in balanced energy and bandwidth. Every node transmits the data to the central node via multiple hops in this approach. Multi-hop-supported protocols are used for data transmission. In the in-network approach, various

aggregate functions such as min, max and sum are applied to the data before they are transmitted to the intermediate node. Data is transmitted to the root node via the parent node in the tree-based approach. Then, the root node transmits the data on behalf of other nodes. The cluster member sends the data to the cluster head (CH) in the cluster-based approach. Then CH transmits the data to a centralised transmitter (Cui *et al.*, 2020).

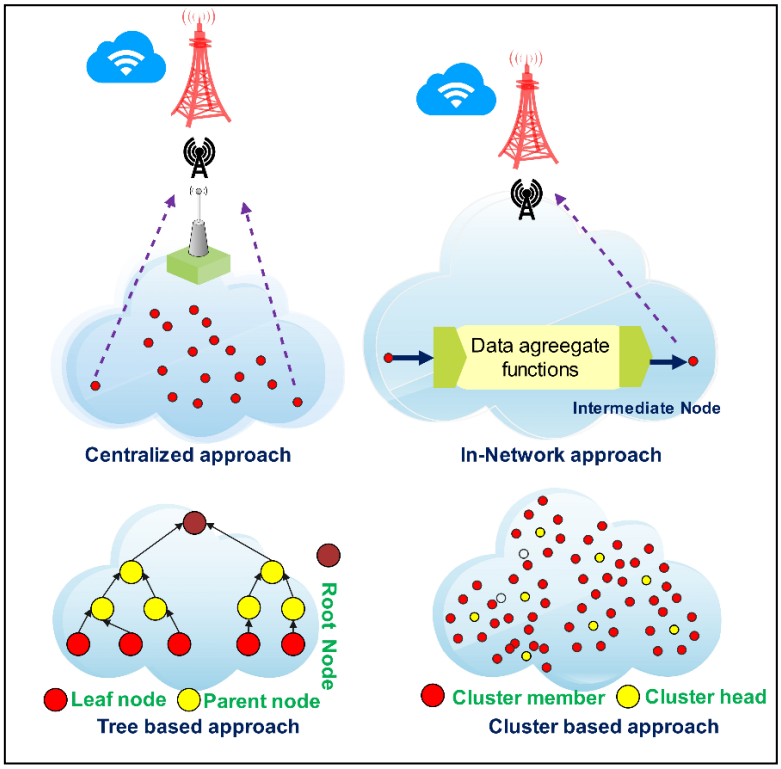

Figure 1: Data aggregation approaches (Cui *et al.*, 2020).

2.1.3 Node Localisation

Node localisation can be defined as determining the locations of nodes connected within a WSN (Randhawa *et al.*, 2017). The principal objective of localisation is to compute the target location. The use of Global Positioning System (GPS) is incredibly costly due to additional GPS devices and their energy consumption. Therefore, sensors are required to self-organise coordinate system. Localisation is the estimated unknown node position through communication between localised and un-localised nodes. Hence, localisation algorithms are used to find the locations of all the nodes within a WSN (Arora *et al.*, 2017a).

Figure 2 shows the classification of localisation algorithms. A central node collects all relevant information from other nodes within a network in a centralised scheme. Then by computing parameters such as distance and travel time, the central node computes the position of all the nodes in the network. Each sensor node exchanges information with its neighbour or a group of nearby sensor nodes in the distributed scheme and estimates parameters locally. A central node is optional in this scheme. An anchor-based scheme uses anchors (nodes with known locations) to localize nodes with unknown positions. The precision of this scheme depends upon the number of anchor nodes in this scheme. There is no anchor node with a perfectly known location in the anchor-free method. Nodes communicate with each other to estimate relative locations instead of computing absolute locations (Arora *et al.*, 2017a).

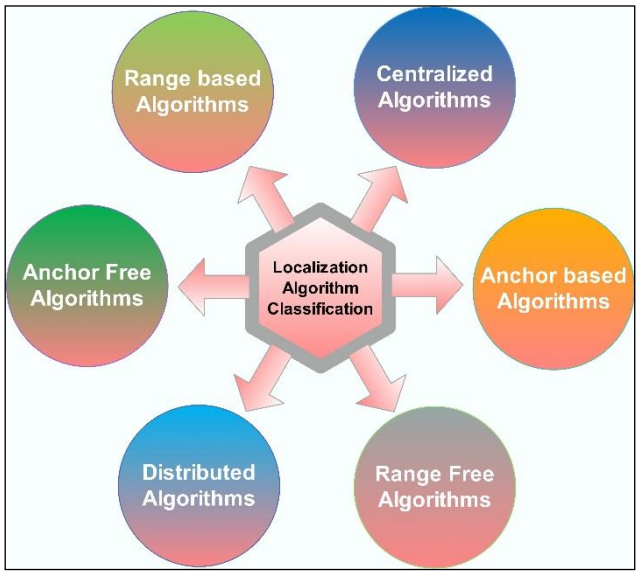

Figure 2: Node localisation (Arora *et al.* 2017a).

2.1.4 Efficient Node Clustering

Clustering is a technique in which the sensors are organised in groups, called a cluster. In each cluster, one node acts as a cluster head (CH), and the remaining nodes form the cluster members. The member nodes of the cluster sense their physical surroundings and transmit the data to the CH. The CH is responsible for aggregating the received data and reporting the data to the sink or BS. The cluster members often send the data to the CH in a single-hop fashion, which is termed as intra-cluster topology (Kalla *et al.*, 2018). Figure 3 shows the variety of clustering techniques and their features.

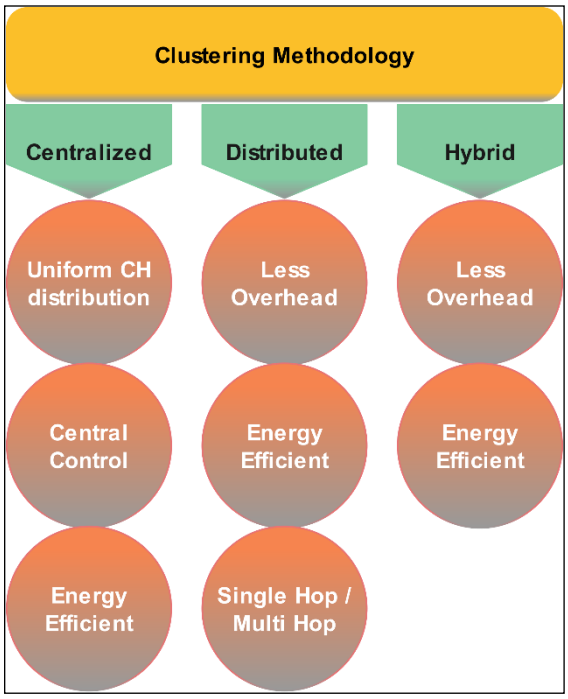

Figure 3: Classification of clustering techniques (Kalla *et al.*, 2018).

In centralised clustering, the clusters and cluster heads are formed by a centralised system. The cluster heads are selected based on residual energy, the location of members of the cluster, etc. In distributed clustering, all the nodes in the clusters can decide to become cluster heads for the current round. To become a cluster head, every node exchange information, such as residual energy value, with its neighbouring node, which will be used to form the cluster head. Hybrid clustering is the combination of both centralised and distributed methodology. Several algorithms exist for efficient clustering based on fuzzy logic, genetic algorithms, neural network, reinforcement learning and swarm intelligence paradigms (Wohwe *et al.*, 2019).

3. THEORETICAL BACKGROUND OF SWARM INTELLIGENCE ALGORITHMS

3.1 Mathematical Foundation of Swarm Intelligence Algorithms

In this subsection, we discussed the mathematical representation of few swarm intelligence algorithms for WSN. In any swarm intelligence-based algorithm with n parameters, $p = (p_1, p_2 .... p_n)$ and m random variables, $\rho = (\rho_1, \rho_2 ... \rho_m)$ can be mathematically expressed as (Singh *et al.*, 2021):

$$X^{t=1} = \phi(x^t, p(t), \rho(t)) \tag{1}$$

where φ represents the non-linear mapping from the current solution (at t) to the better solution (at $t+1$). In Equation 1, parameter p is an algorithm-dependent parameter, and ρ represents a random variable used to describe randomness in the algorithm. This mathematical representation can include all the swarm intelligence algorithms discussed in this paper.

3.2 Whale Optimisation Algorithm (WOA)

The behaviour of whales while searching for prey is modelled to solve optimisation problems. There are seven different main species of this huge mammal; killer, minke, sei, humpback,right, finback and blue (Rana *et al.*, 2020). Humpback whales can recognise and surround the location of the prey methodologically. Identifying the precise position in the a priori search space in the whale is generally not imaginable. The following equations are used to build a mathematical model for the behaviours of whales:

$$\vec{D} = |\vec{C}\overrightarrow{X^*_{(t)}} - X_{(t)}| \tag{2}$$

$$\overrightarrow{X_{(t+1)}} = \overrightarrow{X^*_{(t)}} - \vec{A}\dot{\vec{D}} \tag{3}$$

The above equations represent the iteration in progress. $\overrightarrow{A}$ and $\overrightarrow{C}$ represent coefficient vectors; $X^{*`}$ means the best solution in terms of position vector; $\overrightarrow{X}$ represents the existing location vector; || represents the absolute value. The parameter $\overrightarrow{A}$ and $\overrightarrow{C}$ can be further expressed as:

$$\vec{A} = 2\vec{a}\dot{\vec{r}} - \vec{a} \tag{4}$$

$$\vec{C} = 2\dot{\overrightarrow{Ar}} \tag{5}$$

where $\overrightarrow{A}$ is linearly decreased from 2 to 0 in a linear manner in successive iterations and r is a random vector in [0,1]

3.3 Butterfly Optimisation Algorithm (BOA)

Based on scientific observations, it is found that butterflies have a very accurate sense of locating the source of fragrance. Furthermore, they can separate different fragrances and sense their intensities. The butterflies are best known for having the power to analyse and receive smell in the air, thereby tracing and discovering the direction. A butterfly by nature can generate fragrance with some power that relates to its contentment. Often, they gather and can swarm from one location to another while exercising their strength, which constantly fluctuates. The fragrance released will stimulate and spread quickly for other available butterflies around the neighbourhood to perceive. This behaviour of butterflies is used to solve multidiscipline optimisation problems. The mathematical model of BOA is presented as follows (Arora *et al.*, 2019):

Let:

- f - degree of formulation of fragrance by the butterfly
- c - the modality or pattern of sensory
- I - stimulus strength or level of concentration
- x^t - solution vector x_i for i^{th} butterfly in iteration number t
- g^* - current best solution found among all the solutions in the current iteration
- f_i and r - fragrance of i^{th} butterfly and a random number in [0, 1].

Then mathematically:

$$f = C \times I^a \tag{6}$$

where a and c are parameters in the range [0, 1]. When a = 1, the total amount of fragrance discharged by a given butterfly at a particular location is perceived or sensed by another butterfly group of butterflies at another location. When a = 0, as butterflies emit fragrance, no other butterflies around the defined neighbourhood can sense it in any way. The value of c varies from [0, ∞], which determines the algorithm's behaviour in terms of navigational speed of the butterfly during the period of convergence, especially when a butterfly is tracing another butterfly to a given location due to the level of concentration of fragrance detected at that zone. The iteration phase is represented by:

$$x_i^{t+1} = x_i^t + (r^2 \times g^* - x_i^t) \times f_i \tag{7}$$

$$x_i^{t+1} = x_i^t + (r^2 \times x_j^t - x_k^t) \times f_i \tag{8}$$

The parameters x_k^t and x_j^t are the k^{th} and j^{th} butterflies within the solution space. (Arora & Singh, 2019)

4. PERFORMANCE EVALUATION OF SWARM INTELLIGENCE ALGORITHMS

In this section, we evaluate the performance of swarm intelligence algorithms to solve the optimisation problems discussed in Section 2.

4.1 Performance Evaluation of WOA

In this subsection, we evaluate the performance of WOA for optimum clustering and lifetime of WSNs.

4.1.1 Energy Efficient Clustering Using WOA

Algorithm 1 denotes the application of WOA for efficient clustering of WSNs. Steps 2-3: Encircling the prey phase; Steps 4-8: Search for the prey phase; and Steps 9-10: Hit the target phase.

1: $X_i \rightarrow$search agent
2: C_{ik};$i^{th} \rightarrow$ search agent and j^{th} cluster vector in the cluster C_{ik}
3: $X_i = [C_{i1}, C_{i2}, C_{i3} \ldots C_{ik}]$
4: Objective Function (Initial Energy) (1) $\rightarrow F_1 = \frac{1}{E_i} E_i \rightarrow$ initial energy of i^{th} node
5: Objective Function (Avg. energy of a node)(2) $\rightarrow$
6: $F_2 = \frac{1}{N}\sum_{i=1}^{N} E_{(}i)$
7: Objective Function (Energy consumption rate)(3) $\rightarrow$
8: $F_3 = \sum_{i=1}^{N} \left(E_{p(i)} - E_{RC(i)} \,/\, (E_{p(i)})\right)$
9: $E_{RC(i)} \rightarrow$ Energy consumed in the current round by i^{th} node
10: $E_{p(i)}i_{th}$ node energy in the previous round
11: The fitness function
12: (F) $\rightarrow 1 \,/\, \left[(\gamma \times F_1) + (\theta \times F_2) + \omega \times F_3\right]$
13: $(\gamma, \theta, \omega) \rightarrow$ constant values such that γ+θ+ω = 1

Algorithm 1: WOA for energy-efficient clustering.

In each round of the scenario, cluster heads are selected, and clusters are formed. Next, each ordinary node forwards predetermined bits of data to its cluster head. Each cluster head aggregates the received data and forwards it to the base station with a particular routing protocol or directly transmits the aggregated data to the base station. The region of deployed WSN is 200 m x 200 m. Each ordinary sensor node transmits 4,000 bits of data to its cluster head in each round. The cluster head, which receives the data from its cluster members, aggregates the received data with a certain aggregation ratio. This aggregation ratio is set to 10% in our simulations. For the scenario, we provide a summary result table representing the values of first node dead (FND) and half node alive (HNA) metrics for each of the simulated algorithms. After that, we provide a summary chart that illustrates the values of FND and HNA metrics visually. We also generate charts for the distribution of the number of live sensor nodes and the number of clusters per round. By using these simulation results, we comment on the performance of the simulated algorithms.

Table 1 shows the detailed configuration of the WSN that we have considered to obtain the performance of WOA and BOA. We used MATLAB version 2019b for the simulation.

Table 1: Configuration parameters.

Parameter	Value
Network size	400 m × 400 m
Base Station Location	200 m × 200 m
Num. Of Sensor Nodes	200
Initial Energy	1 J
Data packet type	CBR
Aggregation ratio	20%

Figure 4 shows the distribution of live nodes according to the number of rounds for each simulated algorithm. We have compared the performance of the WOA algorithm with FCA (Godbole, 2012; Lata *et al.*, 2020) and Re-LEACH (Pandey *et al.*, 2019). The number of live sensor nodes using WOA is substantially better than FCA and Re-LEACH.

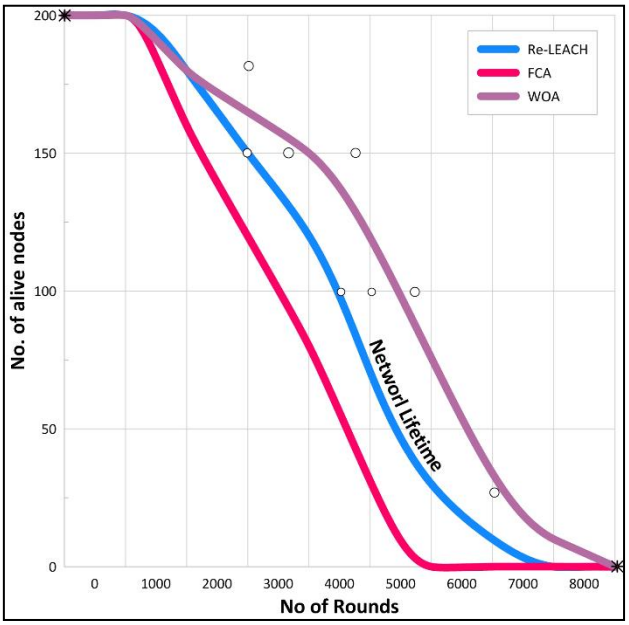

Figure 4: Distribution of live sensor nodes according to number of rounds.

From Table 2, it can be seen that the sensor nodes using FCA and Re-LEACH die early as compared with WOA. In general, WOA outperforms FCA by about 45.8% and beats Re-LEACH by about 69.4%.

Table 2: Values of FND and HND for each algorithm.

Algorithm	FND	HND
Re-LEACH	640	4250
FCA	780	4900
WOA	2160	6126

Figure 5 shows energy consumption by the sensor nodes fora different number of nodes. The other parameters for the network are the same as mentioned in Table 1. From these results, we can say that the energy consumption of the nodes using WOA is less than Re-LEACH and FCA.

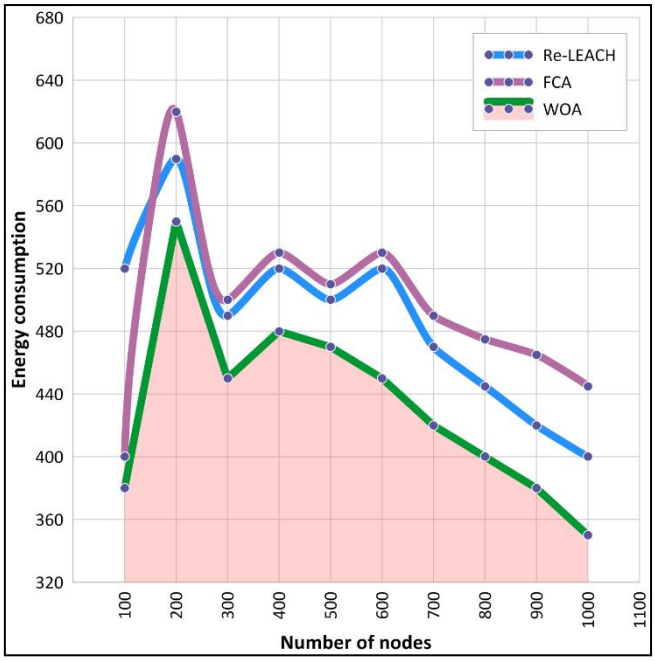

Figure 5: Energy consumption.

4.1.2 Node Localisation Using WOA

Node localisation is a technique used to find the unknown coordinates of sensors using known coordinates of sensors (anchor nodes) (Baidar *et al.*, 2019). Algorithm 2 shows node localisation using WOA. We have used the same parameters as mentioned in Table 1 to obtain the results.

$\mathcal{M} \rightarrow$ Nodes to be localized
$\mathcal{N} \rightarrow$ Anchor nodes
for i=1, i≤n, i=i++ **do**
  $\mathcal{N} \rightarrow$ transmit their co-ordinates
  (Encircling prey) Every $\mathcal{M}_i^{th}$ node $(1 < i < \mathcal{M})$ computes distance (d) between them and N_j^{th} node $(1 < j < \mathcal{N})$ using distance formula:
  $d_i = \sqrt{(x - x_i)^2 + (y - y_i)^2}$
  (Exploitation) the co-ordinates of localized nodes are found using the function:
  $f(x, y) = \frac{1}{N} \sum_{i=1}^{\mathcal{N}} \sqrt{(x - x_i)^2 + (y - y_i)^2}$
  $Where \mathcal{N} \geq 3$
  (Exploration) Add localized sensor nodes in the current stage to the anchor node list and remove them from the unknown node list
end for

Algorithm 2: WOA for node localisation.

Figure 6 shows the total number of nodes localised after every 10^{th} iteration and the corresponding time taken in seconds. From this result, as the number of iterations increases, the total number of nodes with known coordinates also increases. Our findings show that all the nodes get localised after the 94^{th} iteration. The figure also shows the time required for localisation of nodes after every 10^{th} iteration.

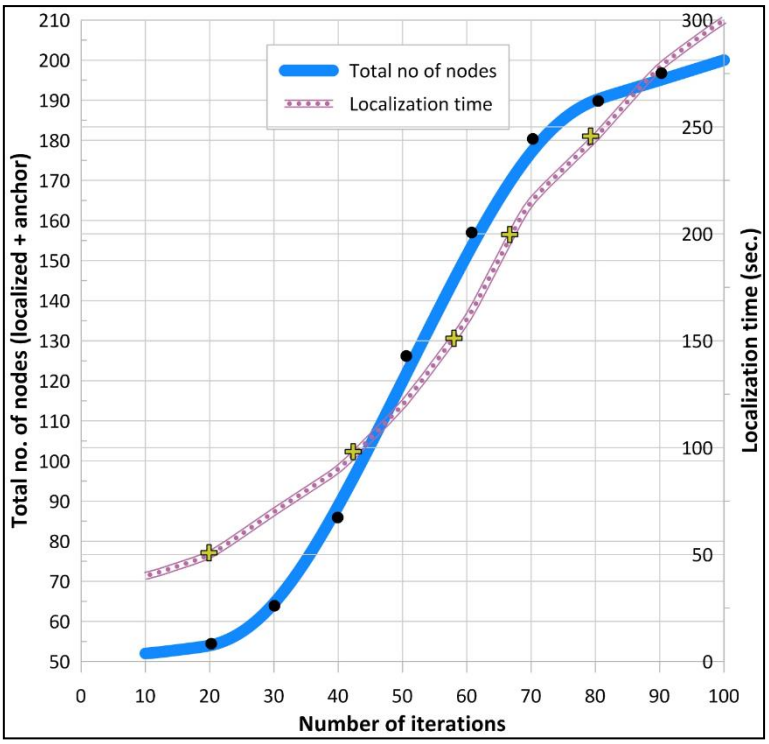

Figure 6: Node localisation using WOA (number of anchor nodes = 50).

4.2 Performance Evaluation of BOA

In this subsection, we evaluate the performance of BOA for optimum clustering and lifetime of WSNs.

4.2.1 Energy Efficient Clustering Using BOA

The BOA chooses the optimal CHs between all sensors by using node degree, node centrality, distance to its neighbours, distance to the base station (BS) and residual energy. Algorithm 3 shows the algorithm for CH selection using BOA. As shown in line 17 of Algorithm 3, the weights (δ_i) are decided as per precedence such that weight (δ_i) $\propto$ precedence. We have considered the configuration as shownin Table 1 to test the performance of BOA.

Table 3 shows FND and HND values for the given simulation scenario. From Table 3 it can be seen that the sensor nodes using FCA and Re-LEACH die early as compared with BOA. In general BOA outperforms Re-LEACH by about 28.3% and beats FCA by about 10.4%.

As shown in Figure 7, BOA performs better than the FCA and Re-LEACH algorithms in terms of the number of live nodes per round. From Figure 8, we see that for a lesser number of nodes, the performance of FCA is better than BOA, and for a more significant number of nodes, BOA performs better in terms of energy consumption.

Butterfly representation and Initialization

$\mathcal{M} \rightarrow$ No. of CHs

$\mathcal{N} \rightarrow$ No. of nodes in the network

For each node id

for i=1, i$\leq \mathcal{N}$, i=i++ **do**

Butterfly position improvisation

$x_i^{t+1} = x_i^t + (r^2 \times g^* - x_t^i) \times f_i$

$x \rightarrow$ butterfly position, $t \rightarrow$ iteration no.

$r \rightarrow$ random(0,1), $g^* \rightarrow$ current iteration

$f_i \rightarrow i^{th}$ butterfly fragrance

$f \rightarrow \mathcal{C}I^a$

$f \rightarrow$ fragrance, $\mathcal{C}$ sensory modality, $i \rightarrow$ stimulus intensity

Fitness function

The residual energy $\rightarrow \mathcal{F}_1 = \sum_{i=1}^{\mathcal{M}} \frac{1}{E_{CH_i}}$

The distance from the normal sensors to CH $\rightarrow \mathcal{F}_2 = \sum_{j=1}^{\mathcal{M}} \left\{ \frac{\sum_{i=1}^{k_j} D(s_i, CH_j)}{K_j} \right\}$

The function of dist. between the CH and the BS

$\mathcal{F}_3 = \sum_{i=1} \mathcal{M} \times D(CH_j, BS)$

The node degree $\rightarrow \mathcal{F}_4 = \sum_{i=1}^{\mathcal{M}} I_i$

Node centrality $\rightarrow \mathcal{F}_5 = \sum_{i=1}^{\mathcal{M}} \frac{\sqrt{D^2(i,j)/P_i}}{Areaof Network}$

P_i = number of neighboring node of CH_i

$\mathcal{F} = \delta_1 \mathcal{F}_1 + \delta_2 \mathcal{F}_2 + \delta_3 \mathcal{F}_3 + \delta_4 \mathcal{F}_4 + \delta_5 \mathcal{F}_5$

Where $\sum_{i=1}^{5} \delta_i = 1$

end for

Algorithm 3: BOA for energy efficient clustering.

Table 3: Values of FND and HND for each algorithm.

Algorithm	FND	HND
Re-LEACH	640	4250
FCA	780	4900
BOA	1040	5235

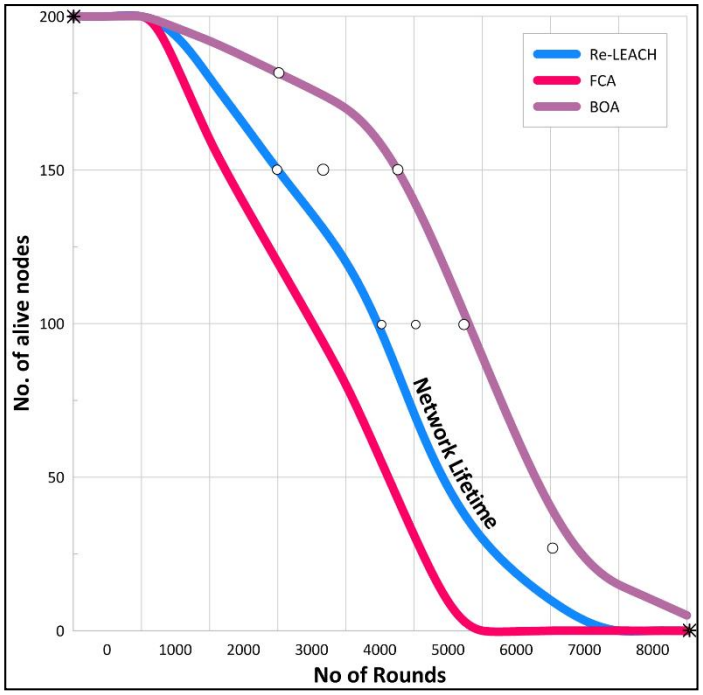

Figure 7: Distribution of live sensor nodes according to several rounds.

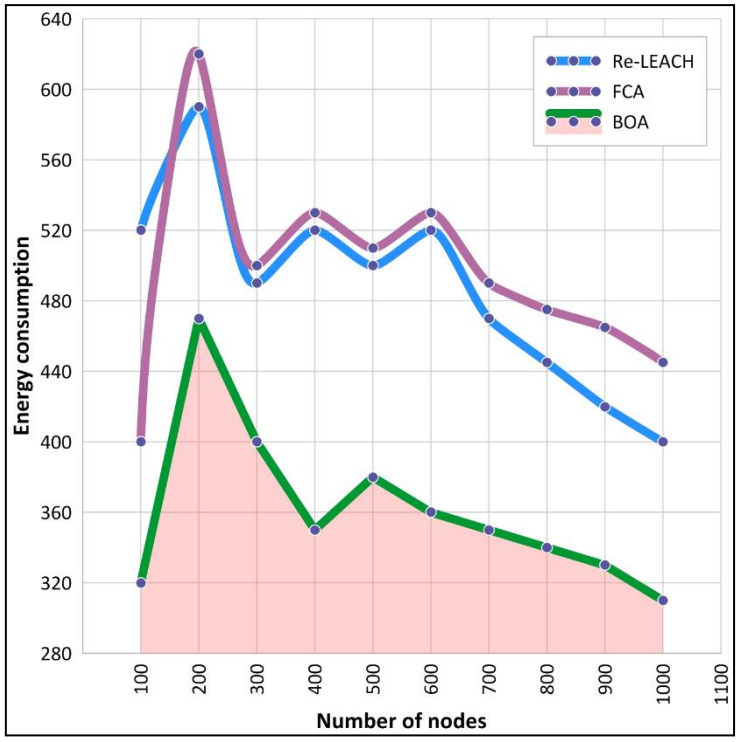

Figure 8: Energy consumption.

4.2.2 Node Localisation Using BOA

Algorithm 4 shows node localisation algorithm using BOA (Arora & Singh, 2017b).

Initialization

1: $\mathcal{M} \rightarrow$ No. of target nodes with location-awareness

2: $\mathcal{N} \rightarrow$ No. of anchor nodes

3: $\mathcal{R} \rightarrow$ Transmission range $\rightarrow$ Each $\mathcal{M}$ and $\mathcal{N}$ have a transmission range

Distance between each target node and anchor node

4: $d_{\mathcal{MN}} = \sqrt{(x_{\mathcal{M}} - x_{\mathcal{N}})^2 + (y_{\mathcal{M}} - y_{\mathcal{N}})^2}$

5: The target node is known as a *localizable* node if there are at least three anchor nodes within the transmission range of the target node

Butterfly initialization at the centroid of the anchor node

6: $(x_c, y_c) = \left\{ \frac{1}{\mathcal{N}} \sum_{i=1}^{\mathcal{N}} x_i, \frac{1}{\mathcal{N}} \sum_{i=1}^{\mathcal{N}} y_i \right\}$

The objective function of the localization problem

7: $f_{x,y} = \frac{1}{\mathcal{N}} \left(\sum_{\mathcal{N}=1}^{\mathcal{N}} \sqrt{(x - x_{\mathcal{N}})^2 + (y - y_{\mathcal{N}})^2} - d_{\mathcal{N}} \right)^2$

Where $\mathcal{N} \geq 3$

The total localization error

8: $E_1 = \frac{1}{\mathcal{N}_1} \sum_{\mathcal{N}=1}^{\mathcal{N}} \sqrt{(x - X_{\mathcal{N}})^2 + (y - Y_{\mathcal{N}})^2}$

Where $(X_{\mathcal{N}}, Y_{\mathcal{N}})$ are estimated node co-ordinates

Repeat steps 4-7 till all nodes get localized

Algorithm 4 BOA for node localisation.

Figure 10 shows the total number of nodes localised after every 10^{th} iteration and the corresponding time taken in seconds. Our findings show that all the nodes get localised after 115 iterations. The figure also shows the time required for localisation of nodes after every 10^{th} iteration.

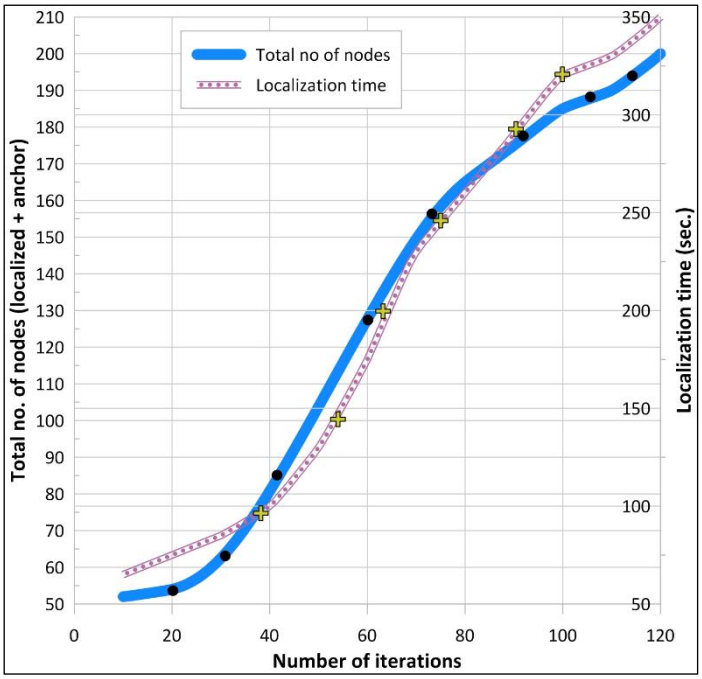

Figure 1: Node localisation using BOA (Number of target nodes = 50).

4.3 Comparison Between WOA and BOA

From the results obtained, we can say that WOA performs better than BOA in terms of the number of nodes (localised + anchor) per iteration. The time required to form localised nodes using BOA is less as compared to that of WOA. The energy consumption of nodes is less for WOA as compared to Re-LEACH, FCA, and BOA. The network lifetime of WOA is better than Re-LEACH, FCA, and BOA. In general, WOA outperforms BOA by about 32.04%.

5. CONCLUSION & FUTURE SCOPE

In this paper, we have compared the performance of WOA, BOA, FCA and Re-LEACH. Our experimentation shows that WOA performs better than other algorithms in terms of energy efficient clustering, node localisation and network lifetime for the considered scenario.

In future we will evaluate the performance of variants of WOA and BOA. We will also evaluate the performance of other swarm intelligence algorithms, including bat algorithm (BA), crow search (CSA), fish swarm optimisation (FSOA), glowworm swarm optimisation (GSOA), squirrel search (SSA), grasshopper optimisation (GOA) and cuckoo search optimisation (CSOA) for WSN.

REFERENCES

Ahmed, M., Houssein, E., Hassanien, A., Taha A., & Hassanien, E. (2017). Maximizing lifetime of wireless sensor networks based on whale optimization algorithm. *Int. Conf. Adv. Intel. Sys. Info.*, Springer, Berlin, Germany, pp. 724–733.

Ahmed, M., Houssein, E., Hassanien, A., Taha, A. & Hassanien, E. (2019). Maximizing lifetime of large-scale wireless sensor networks using multi-objective whale optimization algorithm. *Telecom. Sys.*,**72**:243–259.

Arora, S. & Singh, S. (2017a). Node localization in wireless sensor networks using butterfly optimization algorithm.*Arrb. J. Sci. Eng.*, **42**:3325-3335.

Arora, S. & Singh, S. (2019). Butterfly optimization algorithm: a novel approach for global optimization. *Soft Comput.*, **23**:715–734.

Baidar, L., Rahmoun, A., Lorenz, P. & Mihoubi, M. (2019). Whale optimization approach for optimization problem in distributed wireless sensor network. *Proc. 9th Int. Conf. Info. Sys. Technol.*, pp. 1-7.

Cui, J., Boussetta, K. & Valois, F. (2020). Classification of data aggregation functions in wireless sensor networks *Compt. Netw*, pp. 178-185.

Engmann, F., Katsriku, F., Abdulai, J., Adu-Manu, K. & Banaseka, F. (2018). Prolonging the lifetime of wireless sensor networks: a review of current techniques. *Wirel. Commun. Mob. Com.*, pp. 25-35.

Fanian, F. & Rafsanjani, M. (2019). Cluster-based routing protocols in wireless sensor networks: A survey based on methodology. *J. Netw. Comput. Appl.*, **142**:111–142.

Godbole, V. (2012). Performance analysis of clustering protocol using fuzzy logic for wireless sensor network. *IAES Int. J. Artif. Int.*,**1**:103–111

Kalla, N. & Parwekar, P. (2018). A study of clustering techniques for wireless sensor networks. In Suresh Chandra, S.,Vikrant, B. & Swagatam, D. (Eds.), *Smart Comptuing & Informatics*. Springer, Berlin, Germany, pp. 475-485.

Kos, A., Milutinović, V., & Umek, A. (2019). Challenges in wireless communication for connected sensors and wearable devices used in sport biofeedback applications. *Future Gener. Comp. Sys.*, **92**:582–592.

Lata, S., Mehfuz, S., Urooj, S. & Alrowais, F. (2020). Fuzzy clustering algorithm for enhancing reliability and network lifetime of wireless sensor networks. *IEEE Access.*, **8**:66013–66024.

Liu, X. (2017). Routing protocols based on ant colony optimization in wireless sensor networks: A survey. *IEEE Access*, **5**:26303–26317.

Maheshwari, P., Sharma, A. & Verma, K. (2021). Energy efficient cluster-based routing protocol for wsn using butterfly optimization algorithm and ant colony optimization. *Ad Hoc Netw.*, **110**: 110-114.

Mohammed, H., Umar, S. & Rashid, T. (2019). A systematic and meta-analysis survey of whale optimization algorithm. *Comput. Intel. Neurosc.*, **Vol. 2019**: 8718571

Okwu, M. & Tartibu, L. (2020). *Metaheuristic Optimization: Nat. Insp. Algo. Swarm & Comput. Intell., Theory & Appl.*, **927**:53-60.

Pandey, S. & Kumar, R. (2019). Re-LEACH: an energy-efficient secure routing protocol for wireless sensor networks. *Int. Conf. Comp. Netw. Comm. Tech.*, pp. 777-787.

Rana, N., Abd Latiff, M. & Chiroma, H. (2020). Whale optimization algorithm: a systematic review of contemporary applications, modifications and developments. *Neural Comput. Appl.*, **32**:16245–16277.

Randhawa, S. & Jain, S. (2017). Data aggregation in wireless sensor networks: Previous research, current status and futuredirections. *Wireless Pers. Commun.*, **97**:3355– 3425.

Singh, A., Sharma, S. & Singh, J. (2021). Nature-inspired algorithms for wireless sensor networks: A comprehensive survey. *Comput. Sci. Review*, **39**:100342.

Singh, P., Bhargava, B., Paprzycki, M., Kaushal, N. & Hong, W. (2020). *Handbook of Wireless Sensor Networks: Issues and Challenges in Current Scenario's*. Springer, Berlin, Germany.

Wohwe S., Yenke, B., Förster, A. & Dayang, P. (2019). Optimized clustering algorithms for large wireless sensor networks: A review. *Sensors*, **19**:322-328

Yetgin, H., Cheung, K., El-Hajjar, M. & Hanzo, L. (2017). A survey of network lifetime maximization techniques in wireless sensor networks. *IEEE Commun. Surv. Tut*, **19**:828-854.

SOLAR IRRADIANCE FORECASTING FOR MALAYSIA USING MULTIPLE REGRESSION AND ARTIFICIAL NEURAL NETWORK

Poh-Leng Yew & Yih Hwa Ho*

Centre for Telecommunication Research & Innovation, Fakulti Kejuruteraan Elektronik & Kejuruteraan Komputer, Universiti Teknikal Malaysia Melaka (UTeM), Malaysia

*Email: yihhwa@utem.edu.my

ABSTRACT

The installed capacity of solar photovoltaic (PV) globally continues to rise. In Malaysia, the monthly average daily solar radiation is 4,000-5,000 Wh/m², with the average daily sunshine duration ranging from 4 to 8 h. However, the output of solar energy is related to solar irradiance, which lacks stability due to weather variation. Therefore, solar irradiance forecasting has become an important resource for network grid operators to control the output of solar PV energy. Weather forecasting data, such as temperature, dew point, humidity, pressure and wind speed, are widely available from local meteorological organisations. However, solar irradiance forecasting data is often unavailable. In this paper, multiple regression (MR) and artificial neural network (ANN) models are used to forecast solar irradiance using weather forecasting data. The correlation of each weather parameter with solar irradiance is investigated. It is evident that the ANN model is able to improve the accuracy in terms of root mean square error (RMSE) by 18.42% of its as compared to the MR model.

Keywords: *Solar energy; solar irradiance; forecasting; multiple regression (MR); artificial neural network (ANN).*

1. INTRODUCTION

In the terms sustainability, there is a consideration for solar energy in the fields of environment, economic and social. Traditional power generation is based on fossil fuel, such as coal, petroleum, and natural gas, which is also known as non-renewable energy resource (Kumar, 2020). The depletion of fossil fuel can cause serious problems, in particular an energy crisis (Manieniyan *et. al.*, 2009). This is the most important reason to expand renewable energy, such as solar energy. The decreasing cost of solar energy deployment has made it a better choice for clean energy generation. To this end, the installed capacity of solar photovoltaic (PV) globally continues to rise (Fraas, 2014). Furthermore, solar energy is suitable to be expanded in Malaysia as compared to other renewable energy as it is located in the equatorial region, which has hot climate throughout the year. In Malaysia, the monthly average daily solar radiation is 4,000-5,000 W/m², with the average daily sunshine duration ranging from 4 to 8 h (Aziz *et al*., 2016).

The output of solar energy is related to solar irradiance, which lacks stability due to weather variation. Solar irradiance forecasting techniques can help to stabilise the production of electricity based on solar energy and sustain its integration with power generation based on fossil fuel (Akhter *et al*., 2019). There are different kinds of forecasting techniques. For instance, regression is a statistical approach, while artificial neural network (ANN) is a machine learning approach. Abuella & Chowdhury (2015), Kumar *et al*. (2016), Jeon & Kim (2020), Anthony & Ho (2021) and Khan *et al*. (2022) used ANN for estimation of solar radiation. On the other hand, Mekparyup *et al*. (2013), Nalina *et al*. (2014) and Massidda & Marrocu (2017) used of multilinear and multivariate regression for prediction of solar irradiance.

There is a lack of solar irradiance models for Malaysia despite its suitable geography with high monthly average daily solar radiation and average daily sunshine duration. This paper uses multiple regression (MR) and ANN to forecast solar irradiance using weather forecasting data, including temperature, humidity, wind speed and pressure.

2. METHODOLOGY

2.1 Multiple Regression (MR)

Regression is a process of modelling between a dependent variable, and one or more independent variables (Ul-Saufie *et al.,* 2011; Ostertagová, 2012). Regression with more than one independent variable is known as MR. Linear regression is a linear form, while quadratic regression is a non-linear form (Akinwande *et al*., 2015). The effect of multicollinearity makes the coefficients of regression insignificant when there are many similar independent variables. In order to avoid multicollinearity, variance inflation factor (VIF) can be used to detect the correlation of independent variables (Daoud, 2017). The range of VIF is as shown in Table 1. For instance, independent variables with VIF of above 5 should be removed.

Table 1: The range of VIF (Daoud, 2017).

VIF	Correlation between independent variables
1	Not correlated
Between 1 and 5	Moderately correlated
Greater than 5	Highly correlated

The goal of regression is to find the best fitted line (can be linear or quadratic) using the method of least-squares fit with estimated coefficients. Sinha (2013) suggested the general equations for multiple linear and quadratic regressions, as follows:

$$y = \beta_0 + \beta_1 X_1 + \beta_2 X_2 + \varepsilon \quad (1)$$

$$y = \beta_0 + \beta_1 X_1 + \beta_2 X_2 + \beta_{11} X_1^2 + \beta_{22} X_2^2 + \beta_{12} X_1 X_2 + \varepsilon \quad (2)$$

where:

β_0 - intercept
$\beta_1$and β_2 - linear coefficients
$\beta_{11}$and β_{22} - quadratic coefficients
β_{12} - interaction coefficient
X_1 and X_2 - independent variables
ε - random error that follows normal distribution with mean 0.

2.2 Artificial Neural Network (ANN)

ANN is a machine learning algorithm that allows neurons to learn like a human brain. A neural network consists of input, hidden and output layers. For each layer, there is a neuron (also known as node) that is connected in between multi-layer networks (Massidda & Marrocu, 2017). Mathematically, the output of a neuron can be calculated using Equation 3. The structure of a neuron is shown in Figure 1. In this study, weather parameters, including temperature, humidity, wind speed and pressure, are used as the input, *x* to the ANN, while solar irradiance is used at the output, *y*.

$$y_j = f\left(\sum_{i=1}^{n} x_i \cdot w_i + b\right) \quad (3)$$

where:

x	-	input
w	-	weight
b	-	bias
y	-	output.

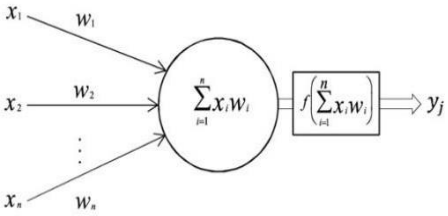

Figure 1: The structure of a neuron (Khatib *et al.*, 2012).

Feed forward neural network (FFNN) is a type of neural network with the application of forecasting. FFNN is based on the backpropagation learning algorithm, which is a type of` supervised learning. The function of backpropagation is to update weights to minimise error. By adjusting the weights, minimum error between the actual and predicted outputs of the ANN can be achieved (Grossi & Buscema, 2007).

3. RESULTS AND DISCUSSION

The solar irradiance and weather data are obtained from a weather station located in Melaka, Malaysia (N 2.314100, E 102.318353). In this study, three months of data (March to May 2020) is used for training the models to forecast irradiance for June 2020.

3.1 Data Analysis for the Dependent and Independent Variables

Solar irradiance is identified as the dependent variable, while temperature, humidity, wind speed and pressure are identified as the independent variables. The data analysis is separated into two parts. The first part is a correlation analysis among the independent variables. The second part is the correlation analysis between the dependant and independent variables.

Figure 2 shows that the data analysis between the independent variables. The relationship between temperature and humidity is the most significant, which is inversely related to each other. Furthermore, it is difficult to identify any relationship for the other independent variables.

Table 2 shows the correlation coefficient (R) and VIF among the independent variables. The relationship between temperature and humidity has the highest VIF of 4.1519, which indicates moderate correlation. For the rest of the independent variables, the values of VIF are close to 1, which indicates no correlation. Based on this, all the independent variables are included for modelling as they have VIF of less than 5.

Figure 3 shows that the data analysis between the dependent and independent variables. The left column shows the overall data view, while the right column shows the zoomed in view from the overall data for better view of the data analysis. It is found that there is high solar irradiance when the temperature is high. Besides that, humidity is the inverse of temperature and thus solar irradiance decreases as humidity increases. Wind speed is not steadily related to solar irradiance. For the pressure, it can be observed that the solar irradiance increases at the moment when pressure drops from its peak.

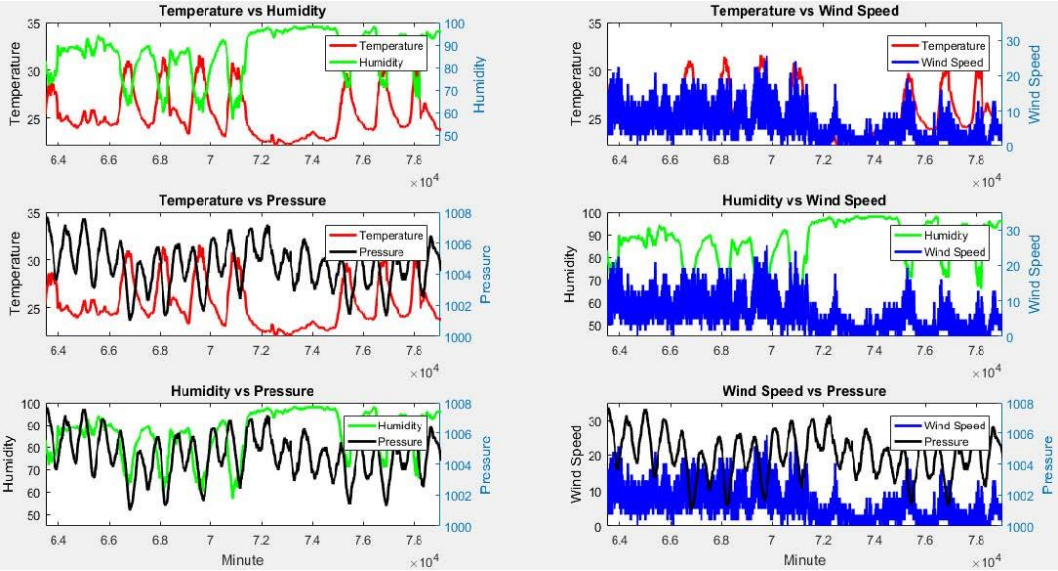

Figure 2: The data analysis between the independent variables (part of data).

Table 2: Values of *R* and VIF between the independent variables.

Parameters	*R*	VIF
Temperature & Humidity	-0.8713	4.1519
Temperature & Wind Speed	0.2452	1.0639
Temperature & Pressure	-0.2544	1.0692
Humidity & Wind Speed	-0.3773	1.1659
Humidity & Pressure	0.1994	1.0414
Wind Speed & Pressure	0.1071	1.0116

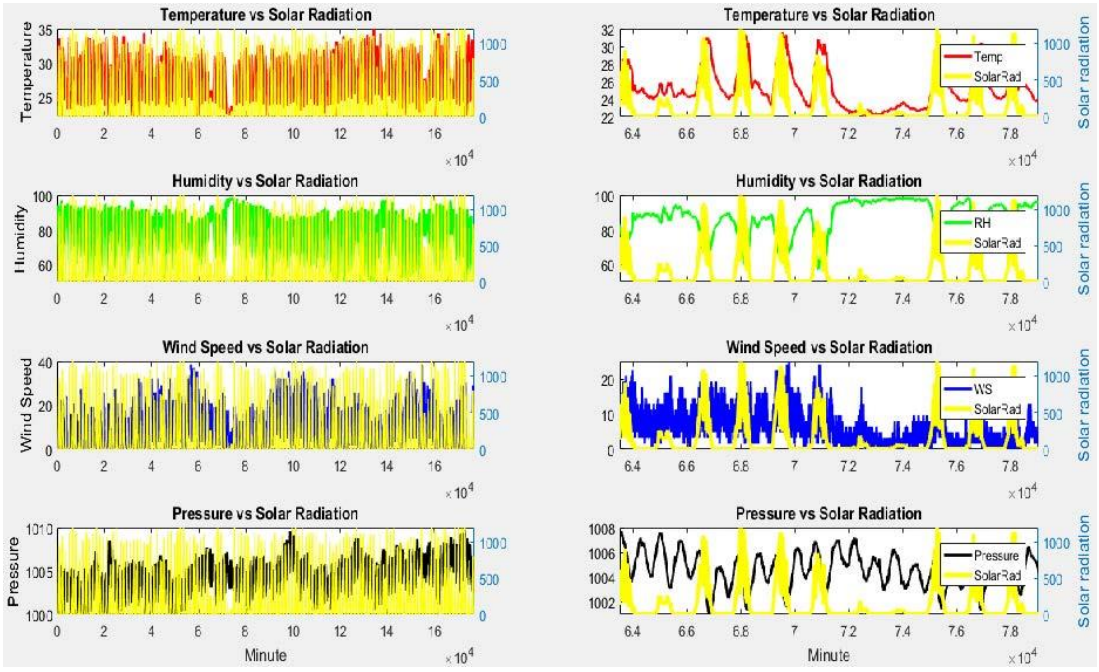

Figure 3: The data analysis between the independent variables and dependent variable.

From Table 3, the relationship between temperature and solar irradiance indicates the highest *R* of 0.6884. This is because strong solar irradiance causes higher temperature. In addition, the lowest *R* of $8.01e^{-4}$ and the highest root mean square error (RMSE) of 865.9054 is found for the relationship between pressure and solar irradiance.

Table 3: Values of *R* and RMSE for the dependent and independent variables.

Parameters	*R*	RMSE
Temperature & Solar Irradiance	0.6884	327.2544
Humidity & Solar Irradiance	-0.6878	313.7555
Wind Speed & Solar Irradiance	0.3552	336.6058
Pressure & Solar Irradiance	$8.01e^{-4}$	865.0954

3.2 Result Validation for the MR Model

The Statistics and Machine Learning Toolbox in MATLAB is used for the results validation for the MR model, as shown in Table 4. With the increase of parameters used, *R* is increased while RMSE is decreased. There is also improvement from 1st order (linear) to 2nd order (quadratic) regression. As the result, *R* is increased from 0.7642 to 0.8815 and RMSE is decreased from 185 to 135 for the model including all the parameters.

Table 4: Validation for MR model with different parameters.

Parameters	First order (Linear)		Second order (Quadratic)	
	R	RMSE	*R*	RMSE
Temp	0.6885	208	0.7148	200
Temp, RH	0.7113	201	0.7197	199
Temp, RH, WS	0.7246	197	0.7589	187
Temp, RH, WS, Pressure	0.7403	193	0.8000	172
Temp, RH, WS, Pressure, Time	0.7642	185	0.8815	135

*Note: Temp - Temperature; RH - Humidity, WS - Wind Speed

Based on the estimated coefficients, the equation of for the MR model is as follows:

$$\begin{aligned} y = {} & 4005X_1 + 1185X_2 - 1005.1X_3 - 186.6X_4 - 4586X_5 - 0.43917X_1X_2 \\ & + 2.8699X_1X_3 - 3.9952X_1X_4 - 104.36X_1X_5 \\ & + 0.0072604X_2X_3 - 1.1856X_2X_4 + 23.461X_2X_5 \\ & + 0.93005X_3X_4 - 1.2566X_3X_5 + 46.991X_4X_5 \\ & + 2.7276{X_1}^2 + 0.027146{X_2}^2 - 0.12369{X_3}^2 \\ & + 0.18551{X_4}^2 - 8.55.27{X_5}^2 \end{aligned} \quad (4)$$

where:

X_1 - temperature
X_2 - humidity
X_3 - wind speed
X_4 - pressure
X_5 - time

3.3 Result Validation for the ANN Model

The Deep Learning Toolbox in MATLAB is used for the results validation for the ANN model, as shown in Table 5. The ANN is set to only one hidden layer that consists of five neurons. It is found that the model gets better as the number parameters used is increased. With only the parameter of temperature used, the ANN only achieves *R* of 0.7278 and RMSE of 195.3103. The ANN that includes all the weather parameters as inputs has the highest *R* of 0.9067 and lowest RMSE of 121.0106.

Table 5: Validation for the ANN model with different parameters.

Parameters	*R*	RMSE
Temp	0.7278	195.3103
Temp, RH	0.7298	194.9912
Temp, RH, WS	0.7709	181.4396
Temp, RH, WS, Pressure	0.8308	159.8094
Temp, RH, WS, Pressure, Time	0.9067	121.0106

*With only one hidden layer that consists of five neurons

**Note: Temp - Temperature; RH - Humidity, WS - Wind Speed

Table 6 shows the validation of the ANN model for all the weather parameters with different number of hidden layers. Each hidden layer has the same number of neurons, which is five neurons. The ANN with three hidden layers achieved the highest *R* of 0.9173 and lowest RMSE of 114.1820. This indicates that with more hidden layers, the ANN becomes deeper and provides better results.

Table 6: Model validation with different number of hidden layers.

Parameters	No. of Hidden Layers	No. of Neuron	*R*	RMSE
Temp, RH, WS, Pressure, Time	1	5 (for each hidden layer)	0.9067	121.0106
	2		0.9153	116.3766
	3		0.9173	114.1820

3.4 Discussion

From the results obtained, it is found that the ANN model performed better as compared to the MR model. This is as the ANN model is based on the backpropagation algorithm, while the MR model is based on the best fit line that is regressed by all the parameters.

The comparison of *R* and RMSE values for the MR (second order quadratic) and ANN (three layers with five neurons for each layer) models is shown in Table 7.

Table 7: Comparison of *R* and RMSE values for the MR and ANN models.

Model	*R*	RMSE
MR (second order quadratic)	0.8815	135
ANN (three layers with five neurons for each layer)	0.9173	114.1820

Figure 5 shows that final structure of the ANN model consisting of three hidden layers. With each hidden layer having five neurons, the model has a total of 15 neurons. As it has the highest *R* and lowest RMSE, it is the best model to be used to forecast solar irradiance.

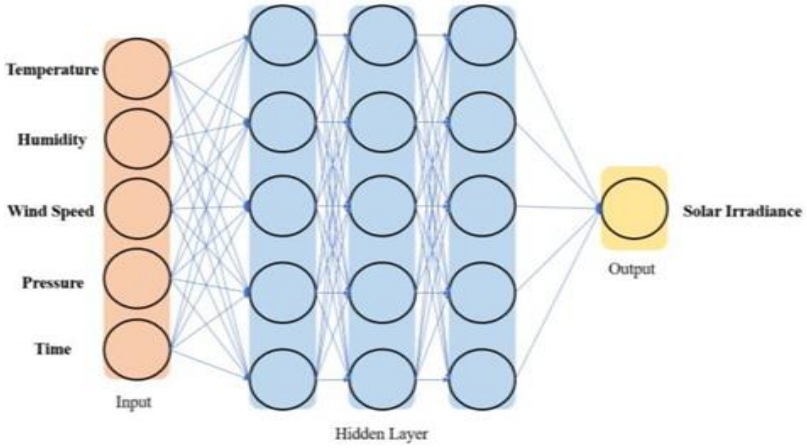

Figure 5: The final ANN structure.

4. CONCLUSION

In this study, MR and ANN methods were used to forecast solar irradiance using weather parameters, including temperature, humidity, wind speed and pressure. It is evident that the ANN model is able to improve the accuracy in terms of by 18.42% as compared to the MR model. The ANN structure with three layers and five neurons for each layer provided highest accuracy with *R* of 0.9173 and RMSE of 114.

ACKNOWLEDGEMENT

The authors would like to thank Universiti Teknikal Malaysia Melaka (UTeM) and the Ministry of Higher Education Malaysia for funding this research under the Fundamentals Grant Scheme (FRGS/2018/FKEKK-CETRI/F00358).

REFERENCES

Abdullah, W.S.W., Osman, M., Kadir, M.Z.A.A. & Verayiah, R. (2019). The potential and status of renewable energy development in Malaysia. *Energies*, **12:** 2437.

Abuella, M. & Chowdhury, B. (2015). Solar power forecasting using artificial neural networks. *Proc. 47th Annual North Am. Power Symp.*, Charlotte, North Carolina, US., 4 - 6 October 2015.

Akhter, M.N., Mekhilef, S., Mokhlis, H. & Mohamed Shah, N. (2019). Review on forecasting of photovoltaic power generation based on machine learning and metaheuristic techniques. *IET Renew. Power Gener.* **13**: 1009-1023.

Akinwande, M. O., Dikko, H.G. & Samson, A. (2015). Variance Inflation Factor: As a Condition for the Inclusion of Suppressor Variable(s) in Regression Analysis. *Open J. Stat.* **5**: 754–767.

Anthony, A. & Ho, Y.H. (2021). Solar Irradiance forecasting using Global Positioning System (GPS) derived total electron content (TEC). *Def. S T Tech. Bull.* **14**: 91 – 100.

Aziz, P.D.A., Wahid, S.S.A., Arief, Y.Z. & Aziz, N.A. (2016). Evaluation of solar energy potential in Malaysia. *Tr. Bioinformatics*. **9**: 35-43.

Daoud, J. I. (2017). Multicollinearity and regression analysis. *J. Phys.: Conf. Ser*. **949**: 012009.

Fraas, L.M. (2014). *Low-Cost Solar Electric Power*, Springer Nature, New York, US.

Grossi, E. & Buscema, M. (2007). Introduction to artificial neural networks. *Eur. J. Gastroenterol. Hepatol*. **19**: 1046–1054.

Jeon, B.K. & Kim, E.J. (2020). Next-day prediction of hourly solar irradiance using local weather forecasts and lstm trained with non-local data. *Energies* **13(**20): 5258.

Khan, W., Walker, S. & Zeiler, W. (2022). Improved solar photovoltaic energy generation forecast using deep learning-based ensemble stacking approach. *Energy*, **240**: 122812.

Kumar, M. (2020). Social, economic, and environmental impacts of renewable energy resources. *In* Okedu, K.E., Tahour, A. & Aissaou, A.G. (Eds), *Wind Solar Hybrid Renewable Energy System*. IntechOpen, London, UK.

Kumar, R. Pathania, S., Gupta, A., Sekhar, R. & Aggarrwal, R. K. (2016). Artificial neural network model for precise estimation of global solar radiation. *Int. J. Curr. Res.* **8**: 31119 – 31124.

Manieniyan, V., Thambidurai, M. & Selvakumar, R. (2009). Study on energy crisis and the future of fossil fuels. *Proc. SHEE 2009*, Annamalai University, Chidambaram, India, 11–12 December 2009.

Massidda, L. & Marrocu, M. (2017). Use of multilinear adaptive regression splines and numerical weather prediction to forecast the power output of a PV plant in Borkum, Germany. *Sol. Energy*. **146**: 141–149.

Mekparyup, J., Saithanu, K. & Dujjanutat, J. (2013). Multiple linear regression equation for estimation of daily averages solar radiation in Chonburi, Thailand. *Appl. Math. Sci*. **7**: 3629–3639.

Nalina, U., Prema, V., Smitha, K. & Rao K. U. (2014). Multivariate regression for prediction of solar irradiance. *Proc. Int. Conf. Data Sci. Eng. 2014 (ICDSE 2014)*, Kochi, India, 26-28 August 2014.

Ostertagová, E. (2012). Modelling using polynomial regression. *Procedia Eng.*, **48**: 500–506.

Sinha, P. (2013). Multivariate polynomial regression in data mining: methodology, problems and solutions. *Int. J. Sci. Eng. Res*. **4**: 962–965.

Ul-Saufie, A.Z., Yahya, A.S., Ramli, N.A. & Hamid, H.A. (2011). Comparison between multiple linear regression and feed forward back propagation neural network models for predicting pm 10 concentration level based on gaseous and meteorological parameters. *Int. J. Appl. Sci. Tech*, **1**: 42–49.